

NONUPDATING METHODS FOR THE CHARACTERIZATION OF
NONLINEAR STRESS-STRAIN AND DELAMINATION FRACTURE
PROPERTIES OF FIBER REINFORCED COMPOSITES

by

BASTIAAN CORSTIAAN WOUTER VAN DER VOSSSEN

DISSERTATION

Submitted in partial fulfillment of the requirements
for the degree of Doctor of Philosophy at
The University of Texas at Arlington
December, 2018

Arlington, Texas

Supervising Committee:

Andrew V. Makeev, Supervising Professor
Erian A. Armanios
Kent L. Lawrence
Ashfaq Adnan
Shih-Ho Chao

Copyright © by

Bastiaan Corstiaan Wouter van der Vossen

2018

In dedication to my wife Leine and my parents,
for encouraging me to pursue my dreams and passions.

ABSTRACT

NONUPDATING METHODS FOR THE CHARACTERIZATION OF NONLINEAR STRESS-STRAIN AND DELAMINATION FRACTURE PROPERTIES OF FIBER REINFORCED COMPOSITES

Bastiaan Corstiaan Wouter van der Vossen, Ph.D.

The University of Texas at Arlington, 2018

Supervising Professor: Andrew V. Makeev

Efforts to develop strength and life prediction analysis tools for aircraft composite structures have shown a great need to understand the complexity and interaction of failure modes. Many failure models are highly sensitive to transverse nonlinear shear stress-strain and delamination fracture properties, which are notoriously hard to measure. Without proper input parameters, life predictions analyses will not be successful. The objective of this work was to accurately characterize these mechanical properties of carbon fiber reinforced polymer composites through advanced experimental methods.

Full-field noncontact deformation measurements using Digital Image Correlation are used to quantify all surface strains components, enabling the design of experiments subject to complex loading. The presented splined-based optimization techniques link measured strains to applied loading, converging to accurate material properties without *ad hoc* assumptions on the

material model. These methods improve on first-order closed-form and iterative numerical solutions due to flexibility and accuracy without the computational expense.

Applications of the optimization model on the Short Beam Shear and Thick Adherend shear tests proved the usefulness of these methods. Full three-dimensional characterization of selected carbon fiber-reinforced polymer composites is presented with a discussion of the applicability of simplifying assumptions on the material model. This experimental program showed that the assumption of transverse anisotropy must be verified, as it may be inaccurate depending on the material. Furthermore, large shear strain response of IM7/8552 UD specimens has been measured by asymmetric three-point bending test.

Applicability of the common D3518 ± 45 degree off-axis tensile test was also deliberated. Shear stress-strain response measured from D3518 specimens disagrees with the Short Beam Shear and Small Plate Twist test results after about 5000 microstrain. This conclusion was shown to be influenced by the specimens' stacking sequence and microdamage which develops well before damage can be spotted in X-ray Computed Tomography reconstructions.

High-magnification deformation measurements are applied to directly measure cohesive laws in precracked Double Cantilever Beam and Thick Adherend shear specimens. Supported by non-destructive *in situ* crack front measurements by Computed Tomography, the loaded crack tip displacements are directly related to the J-integral. The derived traction-separation law is verified by the excellent agreement of the global response between cohesive model Finite Element Analysis and measurements. This study was the first application of the direct measurement of mode II traction-separation law in Thick Adherend shear specimens.

ACKNOWLEDGEMENTS

I wish to accentuate my most heartfelt gratitude to my advisor, Dr. Andrew Makeev. Under his guidance, I discovered a passion for life-long learning, inspired by the great diversity of projects being managed. In Dr. Makeev, I found the confidence and encouragement to exercise my creativity in the lab. I found inspiration in his knowledge and character, and a genuine desire to contribute to the field I study. Most importantly, I thank him for his opportunity and unwavering support throughout the years.

Additionally, I am grateful for the patience and expertise of Brian Shonkwiler and Dr. Yuri Nikishkov, who taught me the tools of the trade. Working with Brian gave me the skills and insight to become a better experimentalist. I wish to acknowledge Dr. Gennadiy Nikishkov and Dr. Guillaume Seon for sharing their knowledge with me. Similarly, I wish to thank my friends at AMSL: Dr. Julia Cline, Dr. Ekaterina Bostaph, Sarvenaz Ghaffari, and Md Hossain. I have always enjoyed a diverse work atmosphere and will look back fondly on all our time together.

I wish to express my appreciation of Dr. Kent Lawrence, Dr. Ashfaq Adnan, Dr. Erian Armanios, and Dr. Shih-ho Chao for being on my committee and for giving me their precious time and expertise. Special gratitude goes to Dr. Armanios with whom I have shared three semesters teaching solid mechanics. Working with him has been insightful, made me a better teacher, and provided me a chance to make a real difference for hundreds of prospective engineers.

Importantly, I present my fondest gratitude to my wife, Leine, for unconditional support during my studies, and for whom I moved to Texas. Thank you to all my dear family, whom

have supported me on this adventure: My parents, for coming to visit me from the Netherlands, and Dr. Karen-Sue Newby, for proofreading my thesis and the everyday help.

Furthermore, I acknowledge and thank NRTC/VLC AFRL for partial funding of this work. I also recognize and thank Boeing Research and Technology Group, Sikorsky, Lockheed Martin, and Bell for manufacturing test coupons for this research. These companies have provided me the opportunity to perform this research at UTA. Such support is gratefully acknowledged.

Dec. 4, 2018

TABLE OF CONTENTS

ABSTRACT	iv
ACKNOWLEDGEMENTS	vi
LIST OF FIGURES	xii
LIST OF TABLES	xviii
LIST OF FREQUENTLY USED SYMBOLS AND ABBREVIATIONS.....	xix
CHAPTER 1 INTRODUCTION	1
1.1 Motivation.....	1
1.2 Outline.....	6
1.3 Material Model for FRP.....	7
1.3.1 Material Model and FEA Implementation.....	7
1.3.2 Shear Nonlinear Behavior.....	10
1.4 Characterization of Mechanical Material Properties for FRPs.....	12
1.4.1 Complexity of Standard Material Certification Programs	12
1.4.2 Characterizing Shear Nonlinearity in FRP Materials	15
1.4.3 Material Parameter Characterization; The Inverse Problem.....	22
1.5 Cohesive Zone Properties for FRP Delamination Failure	26
1.5.1 The Cohesive Zone Model.....	26
1.5.2 Testing for Fracture Properties	28
CHAPTER 2 THREE-POINT BEND TEST AND ANALYSIS METHODS	32
2.1 Experimental Setup.....	32
2.1.1 Application of DIC to the 3-Point Bend Test	32

2.1.2 Specimen Preparation and Selection for 3-Point Bend Test	35
2.2 First-Order Analysis of 3-Point Bend Specimens.....	37
2.2.1 Analytical Solution using Beam Theory Equations.....	39
2.2.2 Theoretical Analysis via Hyperbolic Stress Functions	42
2.3 Multi-parameter Finite Element Method Updating	45
2.3.1 Finite Element Model	45
2.3.2 Finite Element Model Updating Scheme.....	46
2.4 Direct Optimization Method.....	52
2.4.1 Observations and the Applicability of Assumption.....	52
2.4.2 Optimization Model.....	54
2.4.3 Implementation in SBS Test	57
2.4.4 FEA Verifications and Sensitivity Analyses.....	61
CHAPTER 3 CHARACTERIZING NONLINEAR SHEAR LAMINA PROPERTIES .	68
3.1 Small Plate Twist and Verification of Transverse Isotropy Assumption	69
3.1.1 Test Method and Analysis	69
3.1.2 Characterization of Lamina Properties	72
3.2 Tensile Test of ± 45 Laminate	76
3.2.1 Virtual Test and Fiber Reorientation Studies.....	76
3.2.2 Test Method and Results.....	79
3.2.3 CT Study of D3518 Specimens.....	84
3.2.4 Evaluation of In Situ Lamina Shear Properties in SPT.....	86
3.2.5 Compression D695 Tests and Sensitivity to Stacking Sequence.....	87

3.2.6 Reversible Strains	89
CHAPTER 4 ADVANCED APPLICATIONS IN THE SBS METHOD	93
4.1 Characterizing High Strain Response	93
4.1.1 Wrapping phenomena during the test	93
4.1.2 Results from Optimization Model	95
4.1.3 Simulation in FEA environment	96
4.2 The Asymmetric Three-Point Bend Test	100
4.2.1 Reasoning and First-order Estimate.....	100
4.2.2 Experimental program and Test Results	101
CHAPTER 5 CHARACTERIZING TRACTION SEPARATION BEHAVIOR	106
5.1 Cohesive Force Model	106
5.2 Experimental Procedure.....	109
5.2.1 Specimen Manufacturing and Precracking	109
5.2.2 General Procedure.....	111
5.3 Simulation of DCB and TA Tests in FEA	115
5.3.1 FEA Models	115
5.3.2 Sensitivity of FEA Solution to CZM Modeling Parameters	117
5.4 Derivation of CZM Law	119
5.5 Verification by FEA Analysis.....	122
5.5.1 Comparison of Global Response	122
5.5.2 Sensitivity of Solution to Measurement Location in DCB Specimens	123
5.5.3 Application to TA Specimen Without Adhesive	125

5.5.4 Characterizing Bondline Shear Stress-Strain Response	126
5.6 Discussion of Results	129
CHAPTER 6 CONCLUSIONS, DISCUSSION, AND FUTURE WORK	131
REFERENCES	135

LIST OF FIGURES

Figure 1. Ramberg-Osgood Equation fitting Measurement Data	8
Figure 2. Coupling Effects between Transverse and Shear Stresses and Strains. Left: Effect of Transverse Stress on Shear Stress-Strain Response. Right: Effect of Compressive Stress on Shear Stress-Strain Response.	11
Figure 3. Material Characterization Efforts as explained by MIL-HDBK-17	14
Figure 4. Short Beam Shear Test Setup, showing the fixture, a coupon being tested, and the optical system.	18
Figure 5. Loading Configuration of the SBS method. Note the Failure in Interlaminar Shear [41]	18
Figure 6. Setup for Simultaneously Monitoring Surface Strains in all Principle Material Planes using three Synchronized Stereo Camera Systems for the Plate Twist Test Method [40].....	21
Figure 7. Shear Strain Measurements using DIC system in (a) 1-2 Plane, (b)1-3 Plane, (c) 2-3 Plane [39].....	21
Figure 8. Schematic of traction-separation relationship	27
Figure 9. ASTM Standard Fracture Test Methods [3]	31
Figure 10. Short Beam Shear Test Hardware Setup	34
Figure 11. Optical Full-Field Surface Measurements of 3-Point Bend Test with Strain Fields as Measured using DIC	34
Figure 12. Tested Material Plane of the 3-Point Bend Test depends on how the Coupon is cut from a Cured Plate [35].....	37
Figure 13. Static Analysis of the 3-Point Bend Test, with Coordinate Notation and Axial Strain Distribution	40
Figure 14. Solution of SBS Shear Stresses by Whitney’s Analytical Solution.	43

Figure 15. The Whitney and Browning Analytical Model Shows Deviations from Beam Theory at Low Aspect Ratios	44
Figure 16. Typical FEA Model for SBS Finite Element Updating Scheme	46
Figure 17. Logic Flow for the FEM Updating Scheme	48
Figure 18. Virtual gage areas simulated by DIC in the ASTM D5379 V-notched specimen.....	49
Figure 19. Comparison of Material Properties as Calculated using Beam Theory (Initial), after FEMU (Converged), and Reference	49
Figure 20. Effect of Aspect Ratio and Tensile/Compressive Modulus Ratio on Axial Strain Distribution.....	53
Figure 21. Parabolic Stress Distribution is Incompatible with Measurements.....	53
Figure 22. Graphical Representation of Integrating Shear Stresses through Cross-Section.....	57
Figure 23. Trends Captured using Shear Stress-Strain Optimization in SBS Specimens	59
Figure 24. Axial Strain and Stress Distribution with Extrapolation	61
Figure 25. Results of the Virtual Test. The Nonlinear Material Model is Recovered using Optimization Analysis	62
Figure 26. Results of the Optimization Analysis IM7/8552 SBS Specimens (1-3 Plane).....	64
Figure 27. IM7/8552 SBS Analysis. FEMU agrees well with Optimization Analysis.....	64
Figure 28. Sensitivity Analysis: Two Choices for Subset Size	65
Figure 29. Small Plate Twist Test Hardware Setup.....	70
Figure 30. Small Plate Twist Test, showing three Stereo Vision DIC Systems, Fixture, Specimen, and Measured Strain Fields in all three Principal Material Planes.....	71

Figure 31. Finite Element Model Updating (FEMU) Iterative Method for Characterizing Nonlinear Shear Stress-Strain Parameters [40]	71
Figure 32. Average Shear Nonlinear Stress-Strain Behavior of IM7/8552 in All 3 Material Planes, Tested in Short Beam Shear (SBS), Small Plate Twist 1.5in. Square (SPT15) and 2.5in. Square (SPT2.5)	74
Figure 33. Average Shear Nonlinear Stress-Strain Behavior of Material X in All 3 Material Planes, Demonstrating Shear Anisotropy	74
Figure 34. Top: Microscope Images of IM7/8552 SBS Specimens shows Similar Topology in 1-2 and 1-3 Principal Material Planes. Bottom: Different Topology suggests Different Shear Properties.....	75
Figure 35. Virtual Test: FEA Model and Calculated Stress-Strain Curves Match Input for both Material X and IM7/8552	77
Figure 36. Fiber Reorientation in Off-Axis Tensile Test.....	78
Figure 37. Virtual Test: Influence of Fiber Reorientation, Nonlinear Axial/Transverse Modulus, and Correction for Reduced Cross-Sectional Area	79
Figure 38. ASTM D3518 Specimens made of IM7/8552: 8-ply straight $[\pm 45]_{2s}$ (top) and Dog-Bone $[+45_2 / -45_2]_s$ (bottom) Specimens.....	80
Figure 39. Analysis of Pilot Specimens for IM7/8552 and Material X Straight ASTM D3518 Specimens, Including Fiber Reorientation Results.	81
Figure 40. Comparison Nonlinear Shear IM7/8552; ASTM D3518 Straight and Dog-bone Tensile Test, Short Beam Shear, and SPT 1-2 Plane	83
Figure 41. Comparison Nonlinear Shear Material X; ASTM D3518 Straight Tensile Test, Short Beam Shear, and SPT 1-2 Plane.....	83
Figure 42. CT Reconstruction of IM7/8552 D3518 Specimen at 17% Shear Strain.....	84
Figure 43. Pretest/Posttest Scan Material X O115-1-4 (3.1% Shear Strain)	85
Figure 44. An IM7/8552 SPT Specimen with $[0_2/90_2]_{3s}$ Stacking Sequence (top), and Typical Surface Shear Strain Measurements in 1-2 Plane.	87

Figure 45. Comparison of IM7/8552 D695 [± 45] _{2S} Compression Shear Stress-Strain Test Results to SBS, SPT Results. Left: Picture of D695 Fixture with Different Specimen	88
Figure 46. Comparison of IM7/8552 D3518 [$45_2/-45_2$] _{3S} Shear Stress-Strain Test Results to SBS, Sourced from AMSL Materials.....	89
Figure 47. Repeated Loading History of an IM7/8552 D3518 Specimen	90
Figure 48. Repeated Loading Stress-Strain Curves for IM7/8552 D3518 Specimen. Left: Permanent Strains are Visible. Right: Permanent Strains Removed.....	91
Figure 49. Reduction in Shear Modulus and Increasing Permanent and Transient Strains during Repeated Loading of IM7/8552 D3518 Specimen	92
Figure 50. IM7/8552 SBS specimen .25x.25x1.2in. Span Tested in 1-2 Plane. Wrapping of the Specimen Around Loading Nose (top). Strain Fields as Measured using DIC are shown.	94
Figure 51. Characterization of Nonlinear Shear Stress-Strain Behavior in 1-2 Plane for IM7/8552 (Left) and Material X (Right)	95
Figure 52. Highly Nonlinear Shear Model for UMAT to Simulate High-Strain Behavior	97
Figure 53. Material X SBS Specimen: Comparison of Measured and Simulated Strains. Specimens are .25 x .25 x 1.2in. Span under 900lbf Load. Color Legend is Matched	98
Figure 54. Material X SBS Specimen: Comparison of Measured and Simulated Strains. Specimens are .25 x .25 x 1.2in. Span under 1100lbf Load. Color Legend is Matched.	98
Figure 55. Material X SBS Specimen: Comparison of Simulated stresses under 900lbf and 1100lbf Load. Specimen demonstrated Large-scale Yielding throughout the Cross-section. Color Legend is Matched for both Plots	99
Figure 56. Static Analysis of the 3-Point Bend Test, with Asymmetric Span Setup.....	100
Figure 57. IM7/8552 Offset Asymmetric SBS Specimens Tested in 1-2 Plane.	102

Figure 58. IM7/8552 SBS Test Results: Comparison Average Shear Stress-Strain Curves from Symmetric and Offset SBS Specimens. Left: 1-2 Plane. Right: 1-3 Plane	103
Figure 59. Relevant Parameters for the VCCT Method	108
Figure 60. Thick Adherend (Left) and Double Cantilever Beam (Right) specimens as cut from a single co-cured panel.....	110
Figure 61. Thick Adherend Specimen Fabrication Issues	110
Figure 62. Fatigue Failure Progression in TA Specimens. Strains Along Bondline are shown at Select Cycle Counts	111
Figure 63. Thick Adherent Test Experimental Setup. A camera on the left tracks crack front optically. The cameras on the right take images of speckled side for DIC.....	112
Figure 64. DCB Data. Left: Crack Tip Location and Vertical Displacement Field. The red crosses indicate where crack tip displacements are measured. Right: Crack Front as Reconstructed in CT. Distance measured from groove edge	112
Figure 65. Synchronized Data Captured with Cameras during TA test: (a) Optical Tracking of Crack Length; (b) Deformed Speckle Pattern; (c) Shear Strain Measurements; (d) In-plane Specimen Rotation.....	114
Figure 66. Nodes Along Bondline Undergo Translation and Rotation	114
Figure 67. FE Meshed Models for TA (left) and DCB (right) Test Specimens.	116
Figure 68. Convergence of Cohesive Element Size in DCB FEA Analysis.....	117
Figure 69. FEA Simulation of DCB Specimen by CZM Triangular Traction-Separation Law. Graphs show Sensitivity to Cohesive Penalty Stiffness (a), Fracture Energy (b), Maximum Traction Stress (c), and Stabilization Viscosity (d).....	118
Figure 70. Test Data from DCB Specimens. Left: Load-Displacement Data from the Test Frame. Right: Resistance Curve, in accordance with ASTM standard D5528.....	120

Figure 71. Derivation of the Mode I Cohesive Traction-Separation Law in DCB Specimens. Left: J-integral vs Crack Tip Separation. Right: Traction-Separation Curves.	120
Figure 72. Fracture Energy in the TA Test, as Calculated using VCCT	121
Figure 73. Derivation of Traction-Separation Law in TA specimens. Left: J-integral vs Crack Tip Separation. Right: Traction-Separation Curve.	122
Figure 74. Comparison Global Numerical and Experimental Specimen Load-Displacement Measurements for DCB (Left) and TA (Right).....	123
Figure 75. Sensitivity of Traction-Separation Law to Crack Tip Measurement in DCB Specimens.	124
Figure 76. CT and Optical Measurements of IM7/8552 TA Specimens without Adhesive.....	125
Figure 77. CZM Characterization of IM7/8552 Specimens	126
Figure 78. Simulation of KGR Strain Measurement in FEA.....	127
Figure 79. Comparison of Stress-Strain Characterization Analyses for TA Specimens. The Flowchart for the Optimization Method is shown Left.	128
Figure 80. Measured Nonlinear Stress-Strain Behavior of Adhesive in TA Specimens	129
Figure 81. Adjustment of G_{Ic} of CZM Law to Improve Agreement between FEA Simulation and Measurement Data	130

LIST OF TABLES

Table 1. Testing and Processing the 3-Point Bend Specimens in Different Principal Material Planes and Span Lengths Determines Measured Properties.....	38
Table 2. Convergence of Material Properties of IM7-8552 Batch, Compared to Reference.....	50
Table 3. Results of the Virtual Test: Tabular Data for G_{xy} , K_{xy} , and n_{xy}	62
Table 4: Sensitivity Study of Extrapolated Axial Strain Nodes	65
Table 5. Sensitivity Analysis: Analysis Difference between Subset Size	66
Table 6. IM7/8552 SBS Analysis: Comparison of Choice ΔxLR	67
Table 7. Comparison Average Lamina Properties IM7/8552; SBS Method with Optimization and Standard Test Methods.....	72
Table 8. Test Results for ASTM D3518 Specimens.....	82
Table 9. Comparison Linear Shear Modulus G_{12} between SBS and T45	82
Table 10. IM7/8552 Specimens 1-3 Plane Test Results: Comparison Average Material Parameters from Symmetric and Offset SBS Specimens	103
Table 11. IM7/8552 Offset SBS Specimens 1-2 Plane Test Results: Comparison Offset Ratio on Characterized Material Properties	105
Table 12. Material Properties IM7/8552 used in FEA Simulation [61]	116

LIST OF FREQUENTLY USED SYMBOLS AND ABBREVIATIONS

<i>0</i>	Subscript: Reference
<i>1, 2, 3</i>	Subscript: Principal Material Directions
<i>A</i>	Area
<i>a</i>	Crack Length
<i>ASTM</i>	American Society for Testing and Materials
<i>b</i>	Linear Approximation of Axial Strains in Short Beam Shear Test: Intercept
<i>B</i>	FEA Element Width
<i>C</i>	Hooke Tensor
<i>CLT</i>	Classical Lamination Theory
<i>CT</i>	(X-ray) Computed Tomography
<i>CZM</i>	Cohesive Zone Model
<i>D3518</i>	±45deg Off-Axis Tension Standard Test
<i>DCB</i>	Double Cantilever Beam
<i>DIC</i>	Digital Image Correlation
<i>E</i>	Linear Modulus
<i>ENF</i>	End Notch Flexure
<i>F</i>	Nodal Force
<i>FEA</i>	Finite Element Analysis
<i>FEMU</i>	Finite Element Model Updating
<i>FRP</i>	Fiber Reinforced Plastic
<i>G</i>	Linear Shear Modulus Energy Release Rate
<i>h</i>	Specimen Thickness
<i>I</i>	Second Moment of Area
<i>ij</i>	Subscript: Material Plane Index
<i>ILS</i>	Interlaminar Shear
<i>IM7/8552</i>	Carbon Fiber Epoxy Composite Material System by Hexcel

J	J-integral
K	Ramberg-Osgood Parameter: Secant-Intercept Modulus; Cohesive Zone Model: Penalty Stiffness
L	Length, Span
L, R	Subscript: Left, Right
M	Bending Moment
n	Ramberg-Osgood Parameter: Exponent
N	Normal Force
P	Applied Load
$PDFA$	Progressive Damage and Failure Analysis
Q_{ply}	Ply Stiffness Matrix
R	Reaction Force
S	Strength
SBS	Short Beam Shear
SPT	Small Plate Twist
T, C	Subscript: Tensile, Compressive
TA	Thick Adherend
t_n	Cohesive Zone Model: Maximum Strength
U, u	Displacements Matrix
u, v, w	Displacements in Global Directions X, Y, Z
u', v', w'	Rotations about Global Directions X, Y, Z
UD	Unidirectional
$UMAT$	User Material Subroutine (For Abaqus)
V	Shear Force
$VCCT$	Virtual Crack Closure Technique
w	Width
X, Y, Z	Global Geometry Directions
x, y, z	Coordinates in X, Y, Z . Subscripts: in Geometry Directions
γ	Shear Strain
δ	Crack Tip Displacement

Δ	Increment/Change
ε	Normal Strain
θ	Material Parameters of Given Material Model; Fiber Direction Angle; Thick Adherend Gauge Section Rotation
κ	Linear Approximation of Axial Strains in SBS: Slope
ν	Poisson's Ratio
σ	Normal Stress
$\sigma(\delta)$	Cohesive Traction-Separation Law
τ	Shear Stress

CHAPTER 1

INTRODUCTION

1.1 Motivation

Fiber reinforced plastics (FRP) and similar composites are fundamental to modern aerospace structures, where new developments in material science are necessary to meet the ambitious design requirements. The development of new materials also drives and enables new capabilities for the future. In part, the performance of these structures relies on the superior specific strength and stiffness characteristics of FRPs as well as the ability to predict the useful life of in-service structures.

Efforts to develop life prediction analysis tools for aircraft composite structures has shown a great need to understand the complexity and interaction of failure modes. Without proper input parameters, strength and life predictions analyses will not be successful. Failure mechanisms of composite structures are complex due to the high anisotropy of fiber-reinforced materials. In one loading direction, the fibers give the composite high modulus and strength, whereas in other directions the mechanical properties are defined more by the weaker and softer matrix properties.

Failure mechanisms of out-of-plane loads in composite shells are often dominated by matrix properties, such as the out-of-plane elastic modulus and nonlinear shear behavior. Characterizing these properties is difficult, especially when the shear and normal stress-strain material characteristics have coupling in the nonlinear regime. To fully understand the material behavior, an intensive and elaborate program of mechanical testing is necessary. Because of the

high anisotropy and susceptibility of FRPs to moisture, time and temperature, such a program could undergo hundreds to thousands of tests and still be able to define all significant constitutive properties.

This has caused significant efforts in the scientific community to develop new methods that allow the user to define multiple mechanical properties from a single test method in cost-effective ways. Many of these tests make use of complex stress-states and full-field measurements of strains or displacements, preferably using tests of simple geometry and loading and sometimes including specific failure modes. The challenge is to accurately identify the material parameters of the material being tested through advanced numerical methods that can capture the full material behavior.

While constitutive properties of stress and strain are indicative of the performance of a material, the accurate characterization of material behavior during failure phenomena and development of physics-driven failure simulations are necessary to predict the useful life of a composite structure. Many high-performance applications of composite materials require accurate predictions of useful life and other failure performance attributes for the structure. This challenge is enhanced due to the tendency of FRPs to be heavily influenced by manufacturing defects in static strength and fatigue life. Hence, the development and testing process for composite structures would benefit from prediction models of manufacturing techniques and in-situ nondestructive inspection (NDI) techniques to define such manufacturing defects. The development of analysis tools that may predict useful life of composite structures may lead to faster design iterations that require fewer verification and validation tests for certification.

This thesis studies the extraordinary efforts required to gain confidence in material properties, performance, and allowables. The present day industry and government practices dictate a building-block approach, starting from basic coupon-level experiments [1]. Because of the efforts required, many composite materials are only characterized partially, such as only in the linear elastic regime, and strength allowables are specified for specific laminates and stacking sequences. Moving to more advanced characterization efforts quickly requires expensive experimental designs and computationally expensive analyses to derive the material behavior. Therefore, there is a need to address the effectiveness and computational efficiency of material characterization programs.

The first specific problem is the inherent difficulty of characterizing the nonlinear stress-strain properties in in-plane and in out-of-plane shear for fiber reinforced polymer composites. Accurate characterization of the mechanical behavior of fiber reinforced polymer-matrix (FRP) composites is instrumental to predict the stiffness, strength, and useful life of primary composite structures [2]. Traditionally, standard tests require local measurements of deformation to determine the surface strains and a measurement of load and geometry to calculate the applicable stress. Strain gauges are commonly used to measure the average deformation under the area covered by the gauge. As such, the test performed must usually achieve a uniform stress-state, such as in-plane tension, compression, or pure shear. Since FRPs have inherent anisotropy, multiple tests are needed to characterize only a limited set of properties, with the shear moduli measured separately from the normal elastic moduli [3]. Multiple tests have been proposed to measure the shear behavior of FRPs, but most suffer from problems with load introduction,

heterogeneity of the stress field, adequacy of data reduction, consistency, or complexity of specimen preparation [4].

Computationally effective and accurate multi-parameter identification tests reduce lead time and characterization effort for new materials. New methods have been proposed that induce a multivariate heterogeneous stress-field in a composite specimen, while full-field 2D surface deformations are measured [5,6]. The strain field in a heterogeneous stress-field depends on the (distribution of) material stress-strain behavior. Thus, the characterization of said stress-strain behavior poses an inverse problem. These experimental designs usually require a form of iterative Finite Element Analysis (FEA) that is both expensive from a numerical point of view and requires great expertise from the operator and analyst of the test. Furthermore, many of these iterative schemes must assume a certain material model to be fitted. There is still a need for computationally effective test methods that are accurate and flexible enough to capture all the complex constitutive properties of the composite material.

The work presented in this thesis addresses the need for a simpler analysis tool applied to test specimens subject to heterogeneous stress states to solve the material characterization inverse problem in a flexible, intuitive and time- and computationally effective manner. A large portion of this work is applied to the Short Beam Shear test method. The specimens are relatively inexpensive to test and are subject under a combination of shear and bending, making them ideal specimens for this research. Tests performed for this thesis include Short Beam Shear (SBS), Long Beam 3-point bend, Thick Adherend (TA) shear, $\pm 45^\circ$ off-axis tensile tests, and Small (Torsion) Plate Twist (SPT) tests.

The second specific problem addresses the lack of understanding of delamination cohesive laws, which is a fundamental aspect of strength and fatigue progressive damage and failure analysis (PDFA) of composite structures. Delaminations, a major failure mode in composite structures, behave different from bulk material failure. The cohesive zone laws are used to simulate interface damage initiation and progression in the FEA analysis. The derivation of these laws is typically based on mathematical assumptions fit to simplify convergence of analysis tools, instead of physics or measurement. Since convergence models do not usually prove that a solution is unique, the simplifying assumption may cause the simulation task to favor wrong cohesive material properties.

The objective was to perform a feasibility study focused on developing experimental methods and nonupdating analysis techniques for capturing the interface traction-separation law and increasing confidence in material input data for PDFA. Static Double Cantilever Beam (DCB), and Thick Adherend (TA) shear specimens have been pre-cracked under fatigue load and used to test the create mode I and mode II fracture. X-ray Computed Tomography (CT) reconstructions were used to locate the crack front. A direct approach was applied to measure cohesive laws using high resolution Digital Image Correlation (DIC) techniques. This high-magnification surface tracking method was used to measure crack tip separation in these specimens. The usefulness of the method was to be verified by direct comparison of load-displacement curves between numerical Finite Element models and experimental data of the DCB and TA test.

1.2 Outline

The dissertation is divided into chapters as follows: Chapter 1 introduces the problem statement and the objective of the work performed. Chapter 2 shows the development of analysis tools for the Short Beam Shear method. The Finite Element Model Updating (FEMU) was shown as the reference case, as the high-fidelity model captures the stress field as accurately as possible. Using that model as a starting point, a physics-driven approach was used to develop a nonupdating method based only on the measured strains, the specimen geometry, and the measured load.

Chapter 3 lays out the work done to verify the experimental method and analysis developed. Foremost, the chapter compares the experimental results of the SBS, the Torsion Plate Twist, and the $\pm 45^\circ$ off-axis test for two different material systems. The results are used to verify simplifying assumptions on the three-dimensional stress-strain behavior.

Chapter 4 provides evidence to demonstrate the capability of the Short Beam Shear to measure large-strain shear performance. The work done shows that an asymmetric loading nose offset improves experimental results.

Chapter 5 elaborates on the feasibility study for the direct measurement of the cohesive traction-separation law in mode I and in mode II. The chapter first defines the theoretical framework for the project. It follows with the specimen preparation and experimental procedure. Test results and analyses are shown for DCB (mode I) and TA (mode II) specimens. The TA specimen is subject to a mix of mode I and mode II fracture energy, without an available closed-form solution. The fracture energy is approximated using the Virtual Crack Closure Technique (VCCT) method in Abaqus CAE. By employing DIC with high-magnification zoom, the

deformations at the crack tip are measured and used directly for the cohesive law. Usefulness of the results was verified by FEA analysis.

Chapter 6 describes the most pertinent conclusions and perspectives from the work shown in this thesis. At the time of writing, some of the work in this thesis has been published in references [7,8].

The remainder of chapter 1 delves into the available literature for the mechanical testing of FRP materials. This chapter cannot possibly be exhaustive but highlights the research that is more relevant to the research topic. It also defines the current challenges in the topic.

1.3 Material Model for FRP

The mechanical behavior of materials and structures requires knowledge of the relationship between stresses and strains: the constitutive model. Due to the high specific strength and specific stiffness of composite materials, their popularity and demand in aerospace structures is on the rise. This increased demand leads to a high rate of development of new materials. Among these, glass and carbon fiber/epoxy laminated composites have proven important in high-performance designs.

1.3.1 Material Model and FEA Implementation

The material model presented in this thesis is applicable to laminated Glass- and Carbon Fiber Reinforced Plastics (GFRP and CFRP). The mechanical test specimens have a unidirectional layup, unless otherwise specified. In this configuration, all plies are stacked with all fibers in the same direction. This allows for specimen geometry to match with material principal directions. Specimens tested under shear will not behave linearly (brittle). [9–11]. This

nonlinear behavior depends on complex micro-scale behavior, but macroscale behavior is often characterized by stress-strain equations, such as the third-power polynomial and the Ramberg-Osgood equation. A third-power stress-strain response works well in linear systems such as the Virtual Fields Method, but has limited applicability. The Ramberg-Osgood offers the flexibility to specify the nonlinear exponent, improving modeling accuracy (see Figure 1).

$$\gamma_{ij} = \frac{\tau_{ij}}{G_{ij}} + \text{sign}(\tau_{ij}) \left| \frac{\tau_{ij}}{K_{ij}} \right|^{\frac{1}{n_{ij}}} \quad (1-1)$$

$$G_{ij}^* = \frac{1}{G_{ij}} + \frac{1}{n_{ij} K_{ij}} \left| \frac{\tau_{ij}}{K_{ij}} \right|^{\frac{1}{n_{ij}} - 1} \quad (1-2)$$

In this relationship, K and n are nonlinear parameters, and ij represents the 12, 13, or 23 material planes. G_{ij}^* represents the locally reduced inverse of shear modulus due to nonlinearity. Other formulations have been proposed [12–14], which generally use more curve-fitting parameters. The Ramberg-Osgood equation is well suitable to capture nonlinear behavior up to 3-5% shear strain.

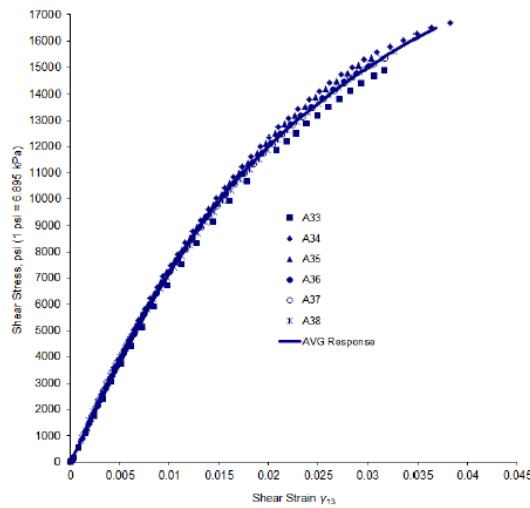


Figure 1. Ramberg-Osgood Equation fitting Measurement Data

The implementation of the Ramberg-Osgood relationship for nonlinear shear in FEA analysis for composites requires the use of a custom UMAT. The following equation represents the relationship between stresses and strains at stress interval k .

$$\begin{bmatrix} \frac{\delta\epsilon}{\delta\sigma} \end{bmatrix}^k = \begin{bmatrix} \frac{1}{E_{11}} & -\frac{\nu_{12}}{E_{11}} & -\frac{\nu_{13}}{E_{11}} & 0 & 0 & 0 \\ -\frac{\nu_{12}}{E_{11}} & \frac{1}{E_{22}} & -\frac{\nu_{23}}{E_{22}} & 0 & 0 & 0 \\ -\frac{\nu_{13}}{E_{11}} & -\frac{\nu_{23}}{E_{22}} & \frac{1}{E_{33}} & 0 & 0 & 0 \\ 0 & 0 & 0 & \frac{1}{G_{23}^*} & 0 & 0 \\ 0 & 0 & 0 & 0 & \frac{1}{G_{13}^*} & 0 \\ 0 & 0 & 0 & 0 & 0 & \frac{1}{G_{12}^*} \end{bmatrix}^k \quad (1-3)$$

where,

$$E_{11} = \begin{cases} E_{11T} & \text{if } \sigma_{11} \geq 0 \\ E_{11C} & \text{if } \sigma_{11} \leq 0 \end{cases} \quad (1-4)$$

The 1, 2, 3 subscripts represent the material principal directions. The axial modulus E , shear modulus G , and Poisson's ratio ν represent orthotropic material properties. ϵ and σ represent the set of normal and shear strains and stresses. Certain materials show a difference in tensile and compressive axial stiffness [15]. The tensile modulus of CFRP is about 10% higher than the compressive modulus. In this thesis, this phenomenon is referred to as bi-modularity.

The Jacobian for each element is finally given as:

$$[J] = \left[\frac{\delta\sigma}{\delta\epsilon} \right]^k = \left(\left[\frac{\delta\epsilon}{\delta\sigma} \right]^k \right)^{-1} \quad (1-5)$$

The Jacobian is used to update material stresses, which can be updated incrementally. Shear stresses cannot be updated incrementally, as the solution might be dependent on the size of strain increments. Therefore, a Newton-Raphson model was implemented to solve for shear stress τ_{new} iteratively. While *residual* < *tolerance*:

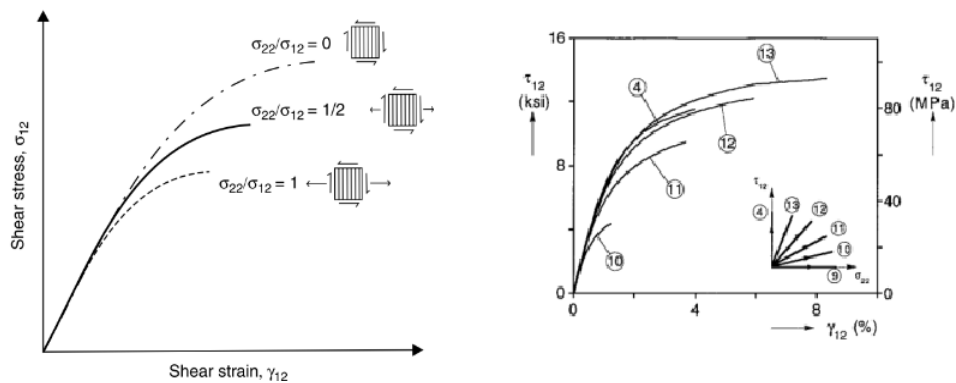
$$\tau_{\text{new}} = \tau_{\text{old}} + \Delta\tau = \tau_{\text{old}} + \frac{G\gamma_{\text{new}} - \tau - \text{sign}(\tau)G \left| \frac{\tau}{K} \right|^{\frac{1}{n}}}{1 + \frac{G|\tau|^{\frac{1}{n}-1}}{nK^{\frac{1}{n}}}} \quad (1-6)$$

$$\text{residual} = \left| \frac{\Delta\tau}{\tau_{\text{new}} + \text{tolerance}} \right| \quad (1-7)$$

1.3.2 Shear Nonlinear Behavior

The micro-structural phenomena that lead to nonlinear behavior in composites are not yet fully understood. Classical Lamination Theory (CLT) assumes that the three-dimensional stress state has no coupling between the normal and shear stress-strain properties. However, there is reason to believe that material shear behavior in the nonlinear regime is sensitive to matrix stress [16,17]. As the shear stress increases, micro-damage in the matrix causes a loss of stiffness; the stress-strain curve becomes nonlinear. Plastic flow in glassy polymers is commonly driven by shear bands, which are regions of localized, heterogeneous deformation forming in the direction of maximum shear stress. This failure phenomenon leads to very local yielding, softening the bulk material by reorientation of fibers. According to Courtney, the yield strength of the material depends on the temperature and hydrostatic pressure. In his model, a tensile pressure would lead to less resistance to shear band formation, while a compressive pressure would increase it [18].

A tensile load in combination with shear deformation will worsen microscale damaged development, whereas a compressive load may delay or suppress the onset of damage, as has been illustrated in Figure 2. Vogler and Kyriakides [19,20], who have done a systematic testing program on the interaction between nonlinear transverse compression and nonlinear shear in AS4/PEEK. Petterson [21] argues that nonlinearity arises from geometric damage, creep deformations, and micro-crack arrays.



* Note: Reprinted with permission from Puck and Schürmann [16] (left) and Vogler and Kyriakides. [20] (right). Copyright © 2002 Elsevier Science, Ltd. All rights reserved.

Figure 2. Coupling Effects between Transverse and Shear Stresses and Strains. Left: Effect of Transverse Stress on Shear Stress-Strain Response. Right: Effect of Compressive Stress on Shear Stress-Strain Response.

Over time, aerospace systems tend to increase structural efficiency with higher stress levels. As such, understanding of nonlinear shear behavior becomes more valuable. Experimental and analytical research by Camanho [17] shows load capacity of composites under transverse tensile and shear stresses. In composite shell structures, the transverse and interlaminar shear

stresses cause plies to separate and delaminate, limiting the failure load. These failure modes are more important in out-of-plane loading than noted in-plane loading. Camanho builds upon Hashin's theory, with matrix failure envelope defined by the shear and matrix stresses. Their interaction influences the failure load. Including these coupling effects improved accuracy of their failure predictions. Without modeling shear nonlinearity, the stress components in design are usually overestimated. As the matrix becomes more ductile, the load capacity decreases from what analytically expected values. Material shear modulus decreases due to micro-damage in the matrix, which does not develop into macro-cracks due to the presence of fibers, but does have a significant effect on the overall structural stiffness.

1.4 Characterization of Mechanical Material Properties for FRPs

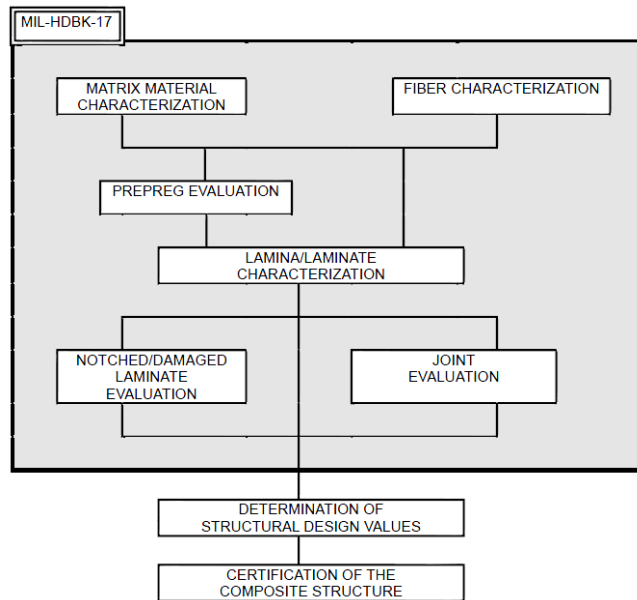
1.4.1 Complexity of Standard Material Certification Programs

The rapid advances in material development drive a great need for efficient characterization methods. Compared to traditional metal characterization programs, fiber reinforced plastics require a wide selection of tests to characterize each constitutive property. This problem is made complex by time-consuming, costly test setups and complex specimen geometries that are often required. Refer to Figure 3 for a map given by the Military Handbook of Composites [1] on characterizing a new material. Due to the complexity and monetary barriers, not all material properties are fully characterized. Among these, nonlinear and out-of-plane shear behavior can be assumed. Even though this behavior is critical to predict complex deformation and damage development, cost may be prohibitive. Once a material has been finally

fully-certified, it can be very difficult to introduce a new material system in later stages of product development.

Material certification requires knowing the constitutive properties in all three principle directions. Industry standards require many different test methods to measure these properties, but some of these will never be mentioned due to prohibitive costs. Often, the material properties exhibit significant scatter in material properties (modulus, strength, manufacturing quality). This scatter is caused by irregularities in production and handling, which means that multiple panels from different batch materials have to be made for each test. This effort makes it also very costly to investigate complicating effects (such as temperature, strain rate sensitivity, fatigue, moisture, nonlinear behavior) in detail. There are multiple quality publications available that discuss mechanical testing in composite materials. Among these, Adams et al. [22] and Czichos et al. [23] provide more insight into these tests. Sharpe [24] gives a more up-to-date view on material characterization, including noncontact measurement methods, such as the Digital Image Correlation method. This method is described in detail by Sutton [25]. Generally, the industry generally has three important guidelines for on the test selection:

1. Preference for small specimens and thin laminates to reduce cost and time;
2. To measure both elastic properties and failure strength in one direction. For accuracy, the stress state has to be homogeneous and not multi-axial.
3. To test on common universal testing machines for reproducibility. This rules out exotic shapes and loading configurations.



* Note: Approved for Public Release by U.S. D.O.D. [1]

Figure 3. Material Characterization Efforts as explained by MIL-HDBK-17

Statistical variability of composite material properties requires testing of a large number of specimens. Creating a material database to provide this statistical variability is therefore time- and cost intensive. Reasons for this variability are numerous [26]. Due to sensitivity to material processing, specimens are created from panels made from different prepreg material batches [27]. As such, batch traceability is important. Laminate testing is usually performed to define allowables for open hole tension/compression for selected layups. After a testing program, the product development may be limited to a subset of layup configurations. Understanding of material nonlinear stress-strain and damage behavior enables development of data-driven methods necessary to predict useful life of composite structures, regardless of chosen layup. This may reduce the number of required tests to verification levels.

Consider the intermediate modulus carbon fiber in a tough epoxy matrix IM7/8552, meant for use in primary aerospace structures [28,29]. The qualification material property data report is extensive and covers hundreds of both UD and laminate test specimens. Still, out-of-plane shear moduli are not measured. Even though shear nonlinear behavior is shown, it is not quantified in the report. Consider that companies may source their own material or need to certify the material for an application, companies are advised to perform in-house material testing to test for relevant laminate stacking sequences, different environments, and more complex failure phenomena. Considering the tremendous amounts of effort and money this requires, it is no surprise that a composite material might not be fully understood during the design process of a structure. Without this understanding, composite structures still rely on extensive structural testing programs for certification.

1.4.2 Characterizing Shear Nonlinearity in FRP Materials

Specimens subject to multi-axial stresses may be used to enhance cost-effectiveness of material characterization programs [30,31]. In one specimen, all orthotropic linear parameters are involved in the global response. By measuring full-field deformations, the contribution of each parameter on the global and local response can be determined. Doing so requires knowledge of the influence of the material on the specimen response (via FEA or analytical solutions) and advanced, reliable, and accurate methods to measure full-field deformations [32]. Doing so efficiently could lead to rapid material screening capabilities.

Measuring the shear nonlinear stress-strain response requires a well-considered choice of test method. Multiple test methods measure the shear response curve, but obtaining a pure and uniform shear stress state is hard to achieve. Torsion of a circular thin-walled tube would give a

very accurate shear stress-strain response, but the test can be prohibitively expensive and sensitive to test misalignment. The Iosipescu (ASTM D 5379) or V-notched Rail (ASTM D 7078) shear tests manage to produce an area of pure shear, but are sensitive to notch geometry. While expensive to produce, the two methods are known to be accurate and reliable. The $[\pm 45]$ tension test (ASTM D 3518) and the two- and three-rail shear tests (ASTMD 4255) require a simpler geometry and test fixture, but do not produce a region of pure shear [33]. As such, these specimens produce the wrong failure mode. Iosipescu specimens may fail from matrix tensile stress at the notch, while Short Beam Shear specimens may create compression cracks under the loading nose. For a more elaborate discussion, please refer to Chaterjee et al. [4].

The SBS test (ASTM D 2344 [34]) is a three-point bending test with a small span-to-thickness aspect ratio. In this configuration, specimens are loaded such that they fail under pure shear stress. Conventionally, the SBS test is popular, because of its simplicity and ease in which the specimens can be conducted. The method is relatively inexpensive, but does not provide a uniform shear stress state and failure is often affected by bending and contact stresses. Large strain gradients are present throughout the specimen. Even though an area of pure shear is formed, it cannot be captured using a strain gauge. Instead, the test performs well as a quality control test, indicating of the quality of the fiber-matrix interfacial bonds (the interlaminar shear strength).

At the University of Texas in Arlington, Advanced Materials and Structures Lab (AMSL), a combination of a modified Short Beam Shear (SBS) method [34] is used to characterize material all three-dimensional constitutive properties, along with interlaminar shear and tensile strength. The lab has adapted the SBS method to prevent the contact and bending

stresses to influence the in-plane shear strength measurements [35]. Full-field noncontact strain measurements are performed using stereo vision 3D Digital Image Correlation (DIC). By tracking surface features as the specimen deforms, surface deformations are measured with high resolution, which allows for an accurate measurement of the shear strains at the whole front surface. This resolution allows for measurement at the region of pure shear, which is too small for strain gauges. As the influences of axial, transverse, and through-the-width stresses are nearly zero at the neutral axis, the shear stress-strain response in the SBS specimen should match that of the more reliable Iosipescu test method.

The SBS test is explained by Makeev [15] and the setup is shown in Figure 4 and Figure 5. In these figures, the three-point bending fixture, speckled specimen, lighting, and DIC system are visible. The speckled specimen usually is a glass or carbon fiber epoxy but is applicable to metals and other material systems. There is some flexibility with the test in terms of specimen size, contact roller dimensions, and support positioning. As the SBS specimens are subject to complex stress states including large axial and shear stresses, material characterization in multiple directions is possible [15]. The SBS test has many benefits over the competing shear methods: coupons with small size and simple geometry can be produced cheaply and often be produced along with other types of specimens from the same panel. Even within a single small panel, dozens of specimens may be cut in different loading planes. In each plane, axial and shear modulus is tested. By testing in the different loading planes, the 3D constitutive model is known with little material use, including the shear nonlinear response in the 1-2 and 1-3 plane. As such, this method may substitute for other test methods, such as Iosipescu shear, curved beam bending, tension, and compression tests.

By using the high-resolution noncontact DIC system, all strain components are measured and used for material characterization. As such, the SBS test method is proven to measure all constitutive properties in 3D, using a small subset of the full-field information. From the full-field data, line and point measurements have been taken to identify material parameters. Full-field strain measurements provide more information than traditional “point” or “area” strain measurements, such as gradients, distribution and information on loading misalignment. Therefore, there is untapped information on material behavior to be discovered.



Figure 4. Short Beam Shear Test Setup, showing the fixture, a coupon being tested, and the optical system.

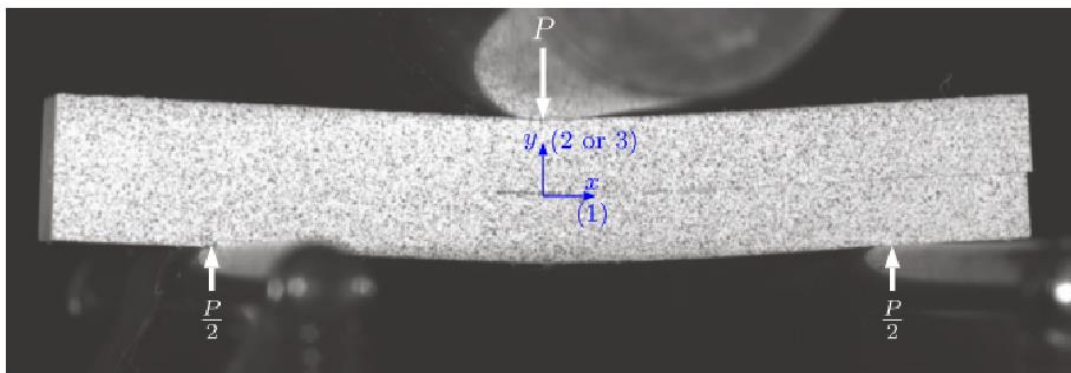


Figure 5. Loading Configuration of the SBS method. Note the Failure in Interlaminar Shear [41]

The PhD theses of Y. He [36], P. Carpentier [35], and J. Cline [37] and a previous MSc thesis by B. van der Vossen [38] serve as the foundation of this continued research. Carpentier used an analytical expression to identify material parameters from strain measurements. By observing that axial strains are linear through the thickness of the specimen, she and Makeev derive a closed-form analytical solution for axial and shear stresses away from the points of contact. These equations are more readily applicable than the solution derived by Whitney and Browning [39]. In the thesis of He, an iterative method is proposed to find accurate shear stress-strain behavior by using accurate shear stresses from FEA. In the thesis of Van der Vossen, it was shown that axial modulus calculations could be improved by FEM and that the shear nonlinear behavior is affected by compressive matrix stress near the contact points. Further evidence is given in the thesis of Cline, who used full-field optimization methods to identify material parameters to minimize the error between FEA-simulated and DIC-measured strains. The tools used include a FEM model and User Material Subroutine, which are used in a Finite Element Model Updating (FEMU) technique to find the shear nonlinear parameters. A similar FEMU approach has been applied in [38] on applied to axial and transverse strains.

The SBS method is unable to measure shear nonlinearity in the 2-3 plane. In order to reach high shear stresses, the applied force must be high. In the 2-3 plane, there are no fibers to hold the bending moment, causing these specimens to usually break before reaching the nonlinear regime. Further work is done to characterize nonlinear shear properties by means of the torsion Small Plate Twist test method [40]. By combining the DIC technique with the plate twist setup, one can measure high shear strains in all material planes. No closed-form solutions exist to relate the applied force to surface stresses, so a tool was developed using the

aforementioned strain matching technique between FEM and DIC to iteratively solve for the 3D nonlinear shear parameters. Figure 6 shows one possible test setup using three stereo camera systems to track surface strains in all three material planes, which are shown in Figure 7.

The popular $[\pm 45]$ ASTM D3518 tensile test [42] is relevant for the thesis as reference. While known for its straightforward specimen geometry, loading, and analysis, it may not be a satisfactory test. As Chatterjee et al. [36] note, the material response and strength depend on the exact lay-up (number and grouping of plies). They note that there are significant matrix tensile stresses in these specimens. As experimentally shown by Sket et al. (2014), these tensile specimens develop significant matrix cracks after this threshold. They also show the fiber axes rotating away from the original 45deg axis, causing the closed-form solutions for the stress to be inaccurate. The ASTM standard advises to use these specimens only up to 5% shear strain. This test is, however, more capable of demonstrating damage progression, most notably permanent strains and shear modulus reduction. This has led to interesting publications on nonlinear shear stress-strain analysis [43]. Even the ASTM D3518, which has homogeneous stress distribution, can benefit from DIC full-field strain measurements [44].

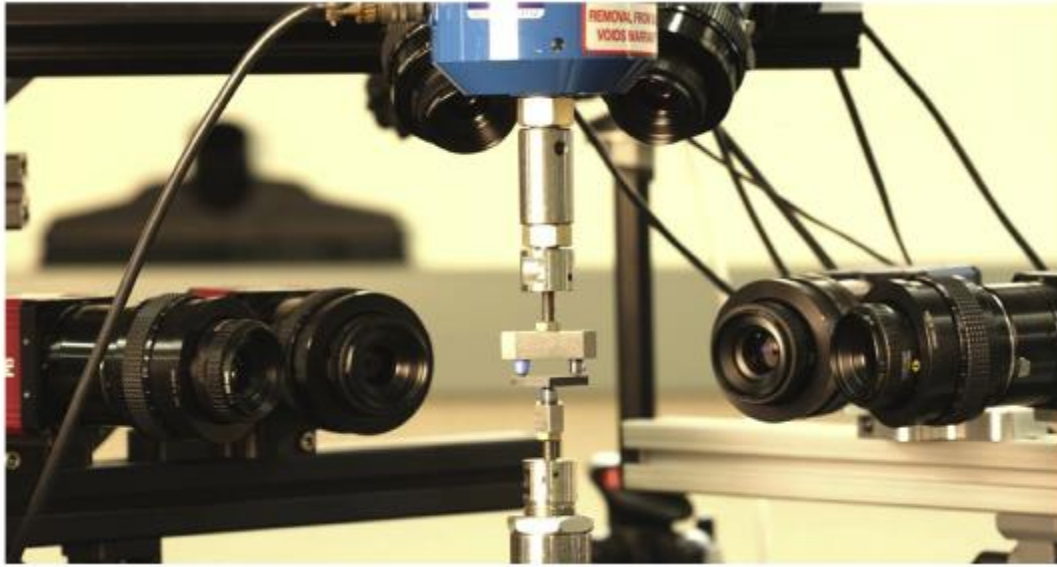


Figure 6. Setup for Simultaneously Monitoring Surface Strains in all Principle Material Planes using three Synchronized Stereo Camera Systems for the Plate Twist Test Method [40]

The applications for nonlinear (transverse) shear stresses in structural composites are already well-established, with methods calculating transverse shear stresses in beams using equilibrium equations [45], using the shear resultant [46] or by functionally graded materials such as in [47,48].

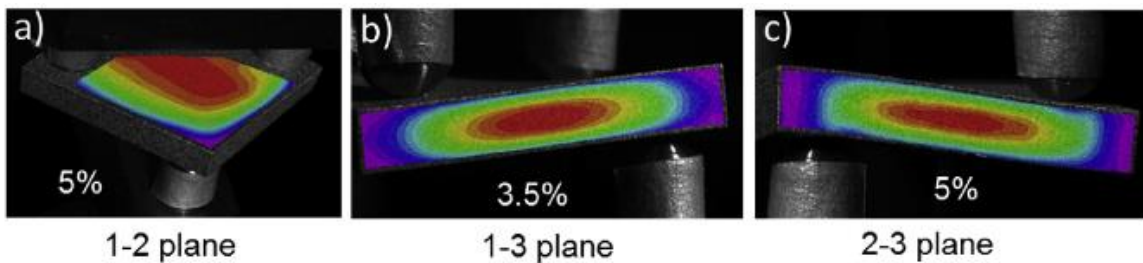


Figure 7. Shear Strain Measurements using DIC system in (a) 1-2 Plane, (b) 1-3 Plane, (c) 2-3 Plane [39]

1.4.3 Material Parameter Characterization; The Inverse Problem

The problem of deriving material properties from strain measurements is often defined as an inverse problem [32,49–51]. In a direct structural analysis, the geometry, loading, and the material model with parameters are known and used to solve for stresses, strains, and displacements. Consider the standard set of FEM equations:

$$K(\theta)U = R \quad (1-8)$$

where $K(\theta)$ is the stiffness matrix as a function of the material constants θ . In this case, the displacements U and loads R are known. For material testing, the inverse for this problem has to be solved: starting with the displacements U (or strain measurements), geometry, and loading configuration (R) to find the material parameters θ . For simple geometries and loadings, inverse relationships may be derived that link measured response to applied loading. As a basic example, the axial modulus may be calculated from strain measurements in tensile specimens, given the specimens cross-section and load level. Introducing complexity such as stress concentrations and non-uniform loading or geometry leads to heterogeneous stress states (not constant). In these cases, specimen response is often dependent on the material behavior and closed-form solutions are not always available.

Measurements from specimens loaded under a homogeneous state may easily be used to derive one or maybe two material parameters, such as modulus and Poisson's ratio.

Measurements from specimens subject to a heterogeneous stress states give information on many more properties. Since optical full-field strain measurements are given in 2D, the full 2D material model could be characterized in one test method. The chosen inverse method must take the complex loading configuration and material model in account to find the relevant material

parameters. The most well-known inverse methods are: Closed-form solutions, Virtual Fields Method (VFM), Finite Element Model Updating method (FEMU), Constitutive Equation Gap Method (CEGM), Equilibrium Gap method (EGM), and the Reciprocity Gap Method (RGM) [51].

Closed-form solutions are the most obvious choice if available, wherein an established relationship between load and stress is used to calculate the material properties. For the standard ASTM test methods, these relationships are known. For tests specimens subject to multiaxial heterogeneous stress states, closed-form solutions are often not available.

Half of the given solutions are updating methods. The FEMU, CEGM, and RGM methods use FEM analyses to compute reference stress, strain or displacement fields. The FEMU method is flexible, widely applicable, and accurate enough to take full 3D geometry and loading into account. Therefore, it is applied by many researchers [49,50,52,53]. The first iteration of the FEA analysis uses an initial guess for the material parameters. A cost function is derived, often comparing the output strain from FEA and measured strain from DIC. Using a sensitivity matrix, the next iteration of the FEA model uses a new set of properties to reduce the value of the cost function. The model keeps iterating until convergence is reached. The cost function is used to evaluate the fit between measured and simulated variables, and is often based on a least-squares fit. The CEGM and RGM are variations on the FEMU approach. The Constitutive Equation Gap method was used previously to verify Finite Element simulations. In the past several years, applications to material parameters identification have been discovered. The Reciprocity Gap method is another variation, employing kinematic fields on the boundaries. So far, no reference is known where this method has been applied to test data.

The other methods are nonupdating. The Virtual Fields Method [54] is based on the principle of virtual work.

$$-\int_{\Omega} \sigma : \epsilon[u^*] dV + \int_{S_f} T \cdot u^* dS = \int_{\Omega} \rho \ddot{u} \cdot u^* dV \quad (1-9)$$

With u^* being the virtual displacement field. First, a constitutive model is chosen such that

$$\sigma = K(\theta) \hat{\epsilon} \quad (1-10)$$

With known strains $\hat{\epsilon}$. Integrating these virtual fields and the strain measurements provides a linear system which can be solved to give the material parameters. This method is highly appropriate and does not require a Finite Element Model, leading to reduced cost. Unfortunately, the virtual fields are assumed. Optimal virtual fields are hard to achieve and require a lot of validation [55]. Linearization of the shear model degrades the quality of the results. Furthermore, the response is integrated from the entire front surface, which includes the insecurities under the stress concentrations and local damage effects. As the axial response is integrated, no difference can be discerned between tensile /compressive moduli. The Equilibrium Gap Method is similar and can be seen as an equivalent of the VFM with piecewise particular fields [56].

The noncontact full-field displacement and strain measurements are of crucial importance to solve the inverse problem. The full strain field is comprised of hundreds or thousands of data points, providing much more data than strain gauges could provide. The options for optical full-field noncontact measurement systems include Moiré interferometry, Digital Image Correlation with speckle or grid patterns, photo-elasticity, or X-Ray stress analysis [24]. Digital Image

Correlation has become the state of the art due to high performance. VIC3D software processes random speckle pattern images to create fields (matrices) of displacement measurements, from which strain fields are derived. The output depends on some user-defined variables, such as the subset size and the filter size. The subset size influences the strain gradient which can be measured, while the filter size renders the data smoother. Some post-processing methods exist to refine DIC data or make it more useable for advanced analysis: Matching Finite Element nodes using bi-linear interpolation [50]; Parameterizing the DIC strain output using Artificial Neural Networks [58]; or least-squares solutions including Multi-Layer Perception Networks [59].

The nonupdating inverse methods described compensate for the lack of closed-form solutions by using overdetermined full-field strain measurements to find the material parameters that are most probable to give the measured response. As such, the method can be no more accurate than the resolution and quality of the DIC speckle pattern. Some tradeoffs are noted; the chosen subset size in the DIC analysis determined how many pixels are used to define the shape function. A direct effect is lack of data at the edges of the measurement field, thus some methods may require extrapolation beyond what is measured. Furthermore, measured strain levels must be sufficiently high to give a satisfactory signal-to-noise ratio. To mitigate these concerns, high magnification DIC is necessary with excellent speckle contrast.

Each of the FEMU- and VFM-life methods has its benefits. The FEMU methods offer higher accuracy and flexibility, albeit at a greater computational cost. Application to the SBS favors the FEMU method, due to the complex contact loading. Deriving virtual fields is complicated by changing boundary conditions; the contact area at the loading nose is a function

of geometry, matrix modulus, and applied load. The FEMU iterative scheme was already applied to derive the nonlinear shear behavior [38,57]. This thesis builds on this work.

1.5 Cohesive Zone Properties for FRP Delamination Failure

The need to develop more durable composite materials for flight-critical composite components and structures, also requires efficient performance prediction. The Finite Element Method (FEM) method has been the most widely accepted technique for strength and fatigue life prediction [60]. Cohesive Zone Modeling (CZM) is a powerful tool to predict delamination initiation and progression.

1.5.1 The Cohesive Zone Model

Damage in a composite structure may be simulated by stress-based or fracture-based methods. Bulk material may use either, such as continuum damage models which degrade elements or fracture models such as VCCT or XFEM. Delamination as a primary failure model in composite structures may best be simulated using fracture mechanics-based methods. These methods are the most pertinent approaches to simulate PDFA in the FEA environment. A distinction may be made between methods that determine crack initiation and crack growth. Linear elastic fracture mechanics have been successful in modeling crack growth, but are limited to small-scale yielding and cannot determine when or where a crack starts. These analyses require a starting crack or a different crack initiation criterion. The Cohesive Zone Model is a powerful way to predict initiation and damage growth of delaminations in composites structures [61–65] and can thus be used to accurately predict fracture progression. The CZM application also extends to bonded structures with large nonlinear yielding response.

One of the focus points of this thesis lies on characterizing delamination crack growth. Laminates by nature are weakest at their ply interfaces. Delaminations at free edges and at notches are often caused by a combination of interlaminar tensile (mode I) and shear (mode II and III) stress and the strength is matrix-dominated and process-dependent. These are among the more challenging constitutive properties to measure. While the matrix stress-strain behaviors and strength values are applicable, delamination growth is a fracture phenomenon and best described using methods that use concepts of energy and work [66]. The cohesive zone method (CZM) described the relationship between crack surface traction and separation [67]. It characterizes local level damage and energy dissipation is defined as the area under the traction-separation curve (see Figure 8). This relationship appears simplified as a triangle, but can take any shape. The shape of this relationship does significantly affect crack growth behavior and should be carefully characterized [67].

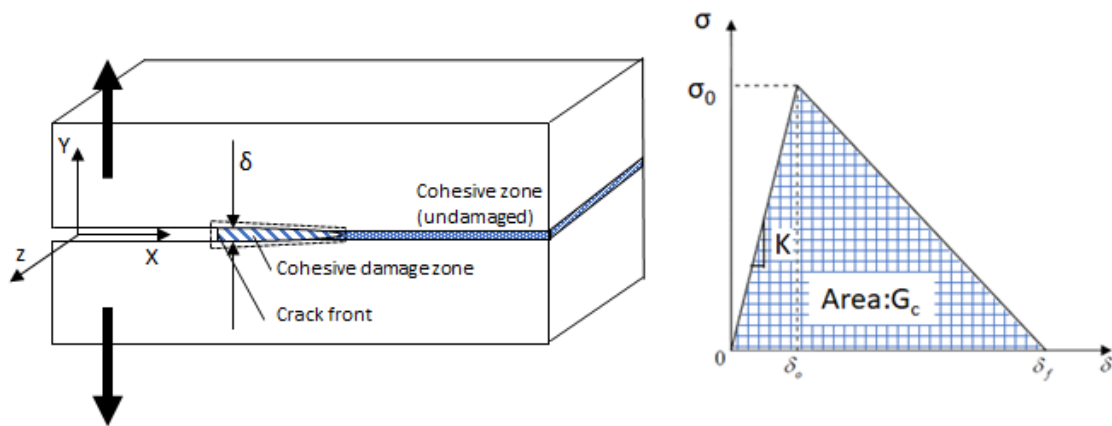


Figure 8. Schematic of traction-separation relationship

CZM provides a macroscopic reproduction of damage along an interface, by defining the traction-separation ($t - \delta$) cohesive law which correlates surface displacements to the applied traction. The CZM model usually makes a distinction between Mode I tension, Mode II, III shear, and mixed-mode fracture criteria. Traction initially increases with surface separation, after which damage is simulated by softening until reaching zero traction at a critical separation [60]. One challenge of PDFAs based on fracture is sensitivity to the cohesive laws, which are typically assumed but not measured.

1.5.2 Testing for Fracture Properties

The standard methods used to measure fracture toughness as specified in D4762 are the Double Cantilever Beam (DCB) [68,69], End Notch Flexure (ENF) [70], and Mixed-Mode Bending (MMB) tests. Specimens created for these tests typically have an initial delamination like flaw implemented during manufacturing. This flaw may be a Teflon insert between plies, which inhibits adhesion between interfaces. DCB mode I toughness results are usually consistent with crack length, but mode II interlaminar shear fracture may not be. In the ENF D7905 configuration, crack propagation is unstable, which limits measured toughness to the cracking onset from the Teflon insert. As such, this fracture behavior may merely reflect manufacturing quality, rather than material behavior. One argument for this is that the shape and regularity of the natural crack front in delamination is usually not straight through the width.

The Thick Adherend (TA) [71] shear test provides an alternative shear test. As a single lap joint, the shear force goes through the interface of interest. The TA test is a standard to measure stress-strain behavior of adhesives in shear. By introducing a crack between the adherends, the interface is loaded predominantly in mode II. As a downside, the single lap joint

is subject to a bending moment as well, which rotates the joined section and induces peeling stresses at the crack tips [72]. Recent research has used the TA test as verification for the Mode I and Mode II traction-separation laws as determined using the DCB and ENF tests [73].

Deriving the traction-separation laws for CZM is not straightforward, nor are methods standardized to characterize them. Recent literature provides two general approaches to characterize such laws. Similar to deriving shear nonlinear behavior, the two methods are either FEA-updating or nonupdating direct methods. The FEA-updating approach uses the FEMU scheme to fit cohesive law parameters to a predetermined shape such as a triangle or trapezium. The CZM parameters are optimized to minimize a cost function or to match an objective function, such as one derived from comparison of FEA to specimen load-displacement data [74–77].

The nonupdating approach identifies the cohesive law directly from measured crack tip displacements δ and the energy release rate G . The crack tip displacement can be measured noncontact optical techniques such as DIC [20] or other reference point-tracking technologies [78,80]. The energy release rate is calculated using the J-integral [78–84] or Virtual Crack Closure Technique (VCCT) in a FEM analysis [85–88]. By the definition, the area under the traction-separation curve represents the fracture toughness of the material. Using this definition, the cohesive law equals the derivative of the $\delta - G$ curve. Svensson proposed a hybrid technique in Ref [82] to estimate the cohesive law using the direct approach and to improve upon it using the inverse approach.

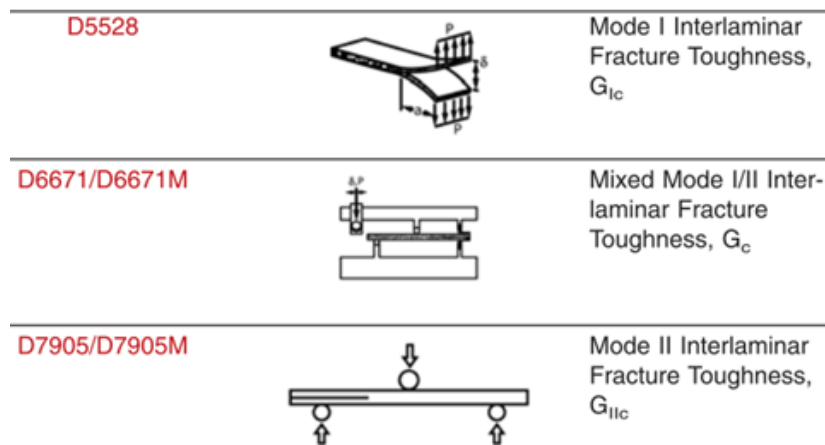
A tradeoff may be performed between the FEMU and direct approaches. The FEMU approach can accurately simulate compliance and ultimate load but is less flexible because of the

assumption on the shape of the cohesive law. This updating inverse method finds the parameters that best fit the objective function. There is no guarantee that the converged solution is unique, accurate, or even applicable to other test configurations. The direct approach does offer the flexibility in the shape of the cohesive law, but the measurements are subject to signal noise. The direct method makes fewer assumptions on the material model than the FEMU scheme, but the final solution is not guaranteed to be accurate or useful to simulate specimen ultimate load or load-displacement behavior. The displacements measured at the side of the specimen are 2D, while the crack is 3D in nature and varies through the specimen width.

Many fracture specimens exhibit this 3D nonuniform crack front through the specimen width. The crack front in DCB specimens is well documented to be curved, which may lead to wrong fracture toughness measurements [61]. The crack front shape is influenced by partial restriction of anticlastic bending and free edge effects, which limits the applicability of the plane stress assumption [74].

Accurately locating the crack front is a large problem in measuring the crack tip displacements. The paint on the side of the specimen may crack at different strain level than the substrate, such that the paint is not a good indicator of crack tip location. Wildy [89] proposed a numerical crack finding algorithm using a governing differential equation. The accuracy of this method is also defined by cracking of the paint and does not have the spatial resolution to pinpoint the crack front in a DIC field either. This problem is worst if paint is brittle, while the adhesive interface is ductile. In that case, the use of the J-integral to describe fracture energy in ductile adhesive materials that have been plastically unloaded is not a physically-complete calculation and should include proper considerations for bulk plasticity [90].

Figure 9 [3] provides an overview of the standard ASTM fracture test methods to characterize delamination growth. Mode III fracture is not usually measured. Important details of these tests are the pre-crack created during specimen production and stable crack growth towards failure. There have been several publications which try to characterize the shape of the traction-separation curve using full-field deformation measurements and FEM analysis. Bergan et al. [91] uses E1922 notched flat plate specimens to derive this law. Svensson and Alfredsson [82] use the DCB and three-point bend test. Both these sources assume a shape of the CZM to reduce the number of variables to solve. Shen et al. [77] uses the FEMU model to optimize any arbitrary CZM shape, but is applied to cementitious composites. Leitao et al. [79,80] uses DIC with ENF to characterize the CZM laws using the J-integral. There is still a need to characterize the CZM for FRP composite delaminations using high-resolution DIC, data-driven analysis without ad hoc assumptions of the CZM law.



* Note: Standard Guide for Testing Polymer Matrix Composite Materials by Subcommittee D30.01 Reproduced with permission of ASTM International in the format Republish in a thesis/dissertation via Copyright Clearance Center.

Figure 9. ASTM Standard Fracture Test Methods [3]

CHAPTER 2

THREE-POINT BEND TEST AND ANALYSIS METHODS

2.1 Experimental Setup

The 3-Point Bend test is a versatile method to obtain the 3D constitutive properties [15,35]. As mentioned in the introduction, the AMSL lab has a nonstandard method to perform the tests, which deviates from ASTM standard [34]. As such, this chapter highlights the test method, and focuses on the analysis tools developed for data reduction.

2.1.1 Application of DIC to the 3-Point Bend Test

The 3-point bend test, in particular the SBS test, is well-known as an affordable yet inaccurate test to measure composite materials interface shear strength. As such, it works well as quality control, or to compare different materials [4]. The issue lies with the heterogeneous stress field. The specimens are subject to a combination of bending and shear stress, and thus large strain gradients. While the specimens are subject to a region of pure shear, no strain gauge is able to capture the magnitude of the maximum shear strain. The strain gauge works by averaging out the strains under the bonded surface, and thus lack the spatial resolution to provide the necessary data.

With the development of noncontact, full-field optical strain monitoring, the required spatial resolution is achieved. The Digital Image Correlation (DIC) method uses two stereo-vision cameras to track surface features of the tested article as it is being deformed. The specimens are prepared with a white base paint coat, followed by a black speckle pattern, applied using a compressor-fed air brush. These black speckles provide the contrast necessary to serve as

tracking features. The VIC-3D software developed by Correlated Solutions maps out the deformation field as these speckles move with respect to each other. The coordinates of the reference speckle (x_i, y_i) and the deformed location (x_i^*, y_i^*) are related by translations u , and v , in the X- and Y- direction respectively. The deformation map can be found by relating the translations between two images [92]:

$$x^* = x + u + \frac{\delta u}{\delta x} \Delta x + \frac{\delta u}{\delta y} \Delta y \quad (2-1)$$

$$y^* = y + v + \frac{\delta v}{\delta x} \Delta x + \frac{\delta v}{\delta y} \Delta y \quad (2-2)$$

Where Δx and Δy represents the distance from the center of sub-image to the point (x, y) , and $u_{i,j}$ represents the displacement gradients. The fidelity of the results depends on several factors, including accurate 3-dimensional calibration of the cameras, image contrast, resolution, the speckle pattern, and proper camera focus. The methodology is flexible, such that different brands of cameras with different specifications may work at any reasonable distance if the focus, calibration, resolution, and field of view are adequate. During this thesis, 16MP cameras were used with 60mm lenses, at approximately 7in. from the specimen. A photo of the SBS setup is shown in Figure 4 in Chapter 1. Figure 10 shows a schematic of the test setup with DIC-system on one surface, and representative test images with DIC analysis are shown in Figure 11.

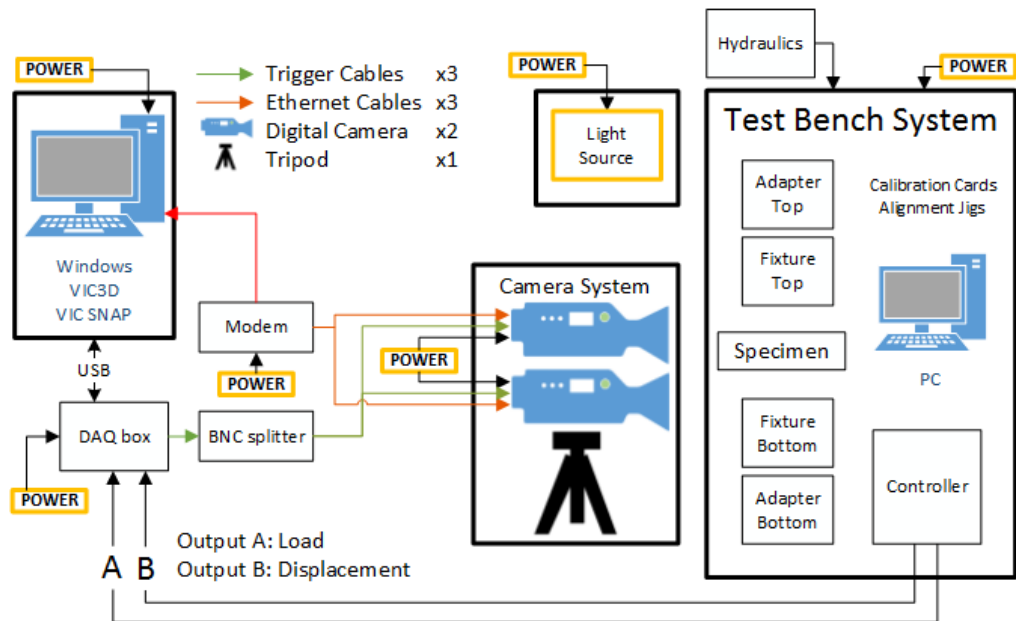


Figure 10. Short Beam Shear Test Hardware Setup

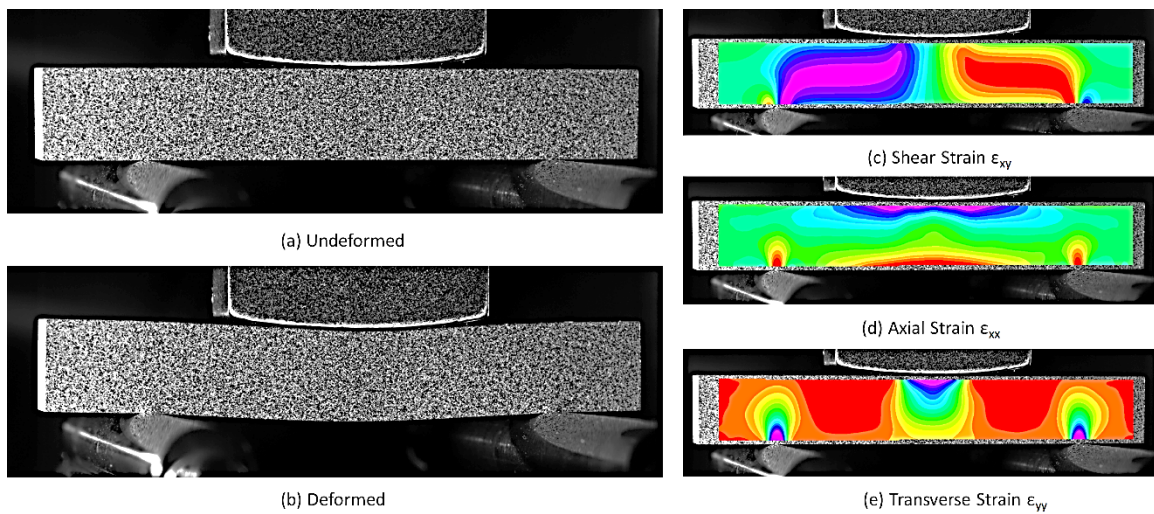


Figure 11. Optical Full-Field Surface Measurements of 3-Point Bend Test with Strain Fields as Measured using DIC

2.1.2 Specimen Preparation and Selection for 3-Point Bend Test

The 3-Point Bend specimens are small and have very simple geometries. This is part of why these are some of the more affordable specimens to make. However, they do require a thick laminate, as the desired square cross-section has a width and height of .25in. While specimens of 1/6in. are adequate, the operator will need to compensate with higher resolution cameras or higher magnification. The cross-section is as constant as possible, and the length depends on the desired test span. SBS specimens only need an aspect ratio (L/h) of 5-7, while long beam specimens need much more length. For SBS specimens of .25in. high, this comes out to a span of 1.2in. The loading nose either has either a 2in. or a 4in. diameter, as the large contact surface suppresses mixed compression/ shear cracks at the contact. The supports are .25in. in diameter. For a detailed derivation for the optimal span and test parameters, refer to Carpentier [35]. The parameters of the loading fixture have negligible effect on the material properties measured but does change the strain field locally as to induce the desired failure mode.

The DIC full-field measurements are by nature 2-dimensional. As such, it is appropriate to apply this method to specimens subject to either plane-stress or plane-strain. The Short Beam Shear specimens are approximately plane-stress, such that the strain varies little throughout the width of the specimen. To achieve full 3-D material characterization, multiple material planes must be tested. The specimens to be tested are cut and loaded in the desired material plane. The plane notations are such that the first number is the longitudinal axis, and the second number the vertical axis. The numbers represent the principal material directions as defined in Figure 12, with the 1-direction defined in the direction of the fibers and the 3-direction being out-of-plane. In this case, specimen cut as configuration A can be loaded both in the 1-2 and 1-3 plane.

Specimen B can be loaded in the 2-3 and 2-1 direction, while C can be loaded in the 3-1 and 3-2 planes. Specimens tested in configuration C require very thick laminates, and will generally have a smaller span, width and height to compensate [93].

3-Point Bend specimens are subject to axial stress due to bending and shear stress, inducing gradients of axial, transverse, and shear strains. These specimens ideally have a linear distribution of axial strains, such that this strain component is equal to zero at the neutral axis. On the other hand, shear stress is maximum at the neutral axis, creating a region of pure shear. Short Beam Shear specimens capitalize on this phenomenon, and due to their short span are more likely to fail in shear. Long beams, on the other hand, are more likely to fail under bending induced axial stresses before shear strain becomes significant. As such, it is beneficial to test both short and long beam specimens. Table 1 summarizes the most popular configurations for the 3-Point Bend test and the desired material properties that can be characterized using this test.

Since transverse stresses are absent halfway between the loading nose and the supports, axial strains are merely a function of the applied bending stress. Any transverse strains that are present are assumed to be a result of the Poisson's Ratio effect under the chosen material model. Altogether, each specimen can provide a measure of the axial modulus, the Poisson's Ratio, and shear modulus in one test.

One can note that if SBS coupons are tested in the 1-2, 1-3, 2-3, and 3-2 planes, the full 3-D constitutive stress-strain model is characterized. Unfortunately, not every failure mode may be achieved. The short beams tested with the fibers aligned with the longitudinal axis benefit from the high axial strength, allowing the specimens to fail under pure shear and allows for the full nonlinear shear stress-strain curve to be determined. On the other hand, specimens tested in

the 2-3 and 3-2 plane exhibit a much smaller tensile strength and will generally fail under tension before shear strains become significant, such that the nonlinear shear behavior cannot be determined in this plane.

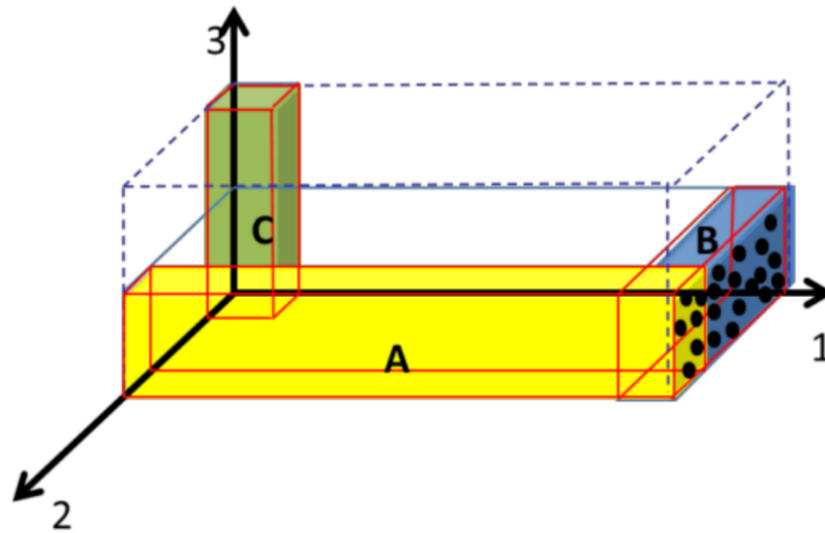
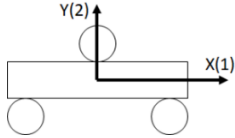
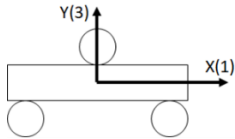
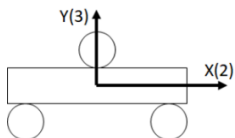
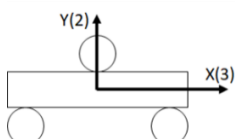
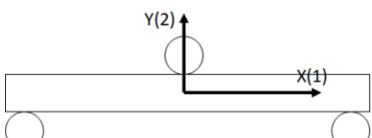
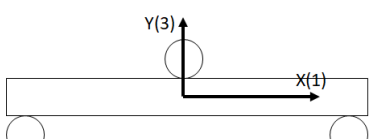


Figure 12. Tested Material Plane of the 3-Point Bend Test depends on how the Coupon is cut from a Cured Plate [35]

2.2 First-Order Analysis of 3-Point Bend Specimens

The following analysis provides a first-order estimate of the stress-state in 3-Point Bend specimens based on beam theory equations (section 2.1.1), and the more general solution offered by Whitney and Browning [94] (section 2.2.2).

Table 1. Testing and Processing the 3-Point Bend Specimens in Different Principal Material Planes and Span Lengths Determines Measured Properties

	Material Plane	Measured Property
A		Axial Tensile Modulus E_{11T} , E_{11C} , $E_{11average}$ Poisson's Ratio ν_{12} Shear Stress-Strain Properties G_{12} , K_{12} , n_{12} Desired Failure Mode: Pure Shear S_{12}
A		Axial Tensile Modulus E_{11T} , E_{11C} , $E_{11average}$ Poisson's Ratio ν_{13} Shear Stress-Strain Properties G_{13} , K_{13} , n_{13} Desired Failure Mode: Pure Shear S_{13}
B		Axial Tensile Modulus E_{22T} , E_{22C} , $E_{22average}$ Poisson's Ratio ν_{23} Shear Modulus G_{12} Desired Failure Mode: Matrix Tension S_{22T}
C		Axial Tensile Modulus E_{33T} , E_{33C} , $E_{33average}$ Poisson's Ratio ν_{32} Shear Modulus G_{23} Desired Failure Mode: Interlaminar Tension S_{33T}
A		Axial Tensile Modulus E_{11T} , E_{11C} , $E_{11average}$ Poisson's Ratio ν_{12} Shear Modulus G_{12} Desired Failure Mode: Fiber Compression S_{11C}
A		Axial Tensile Modulus E_{11T} , E_{11C} , $E_{11average}$ Poisson's Ratio ν_{13} Shear Modulus G_{13} Desired Failure Mode: Fiber Compression S_{11C}

2.2.1 Analytical Solution using Beam Theory Equations

With the full-field strain measurements, it is possible to make a first estimate of the material properties in the 3-Point Bend specimen. For the purposes of this analysis, the beam theory equations do not apply to the regions near the contact surfaces, as they are subject to transverse stresses. Halfway between the loading nose and the support locations, the strain distribution is parabolic, without being influenced by the contact surfaces. This parabolic shear strain and linear axial strain distribution is characteristic for stresses in beams. Figure 13 schematically shows the SBS specimen and defines several key variables as well as the shear force and bending moment diagrams. It also shows that the strain distribution conforms to beam theory only away from the contact surfaces. From this 2-mm wide vertical section, the axial and shear strains are averaged and extracted for analysis.

As the test is being performed (quasi-static, displacement control, 0.05in./min), the DIC system will capture the surface deformations at regular intervals. Each frame provides sufficient information to characterize axial moduli and the Poisson's Ratio. As the signal-to-noise ratio improves at larger strains, the confidence in the result improves at larger load levels. Since the Poisson's Ratio and axial moduli are linear constants, only one frame is required. The shear modulus does require knowing stresses and strains at multiple load levels, as this is a nonlinear property.

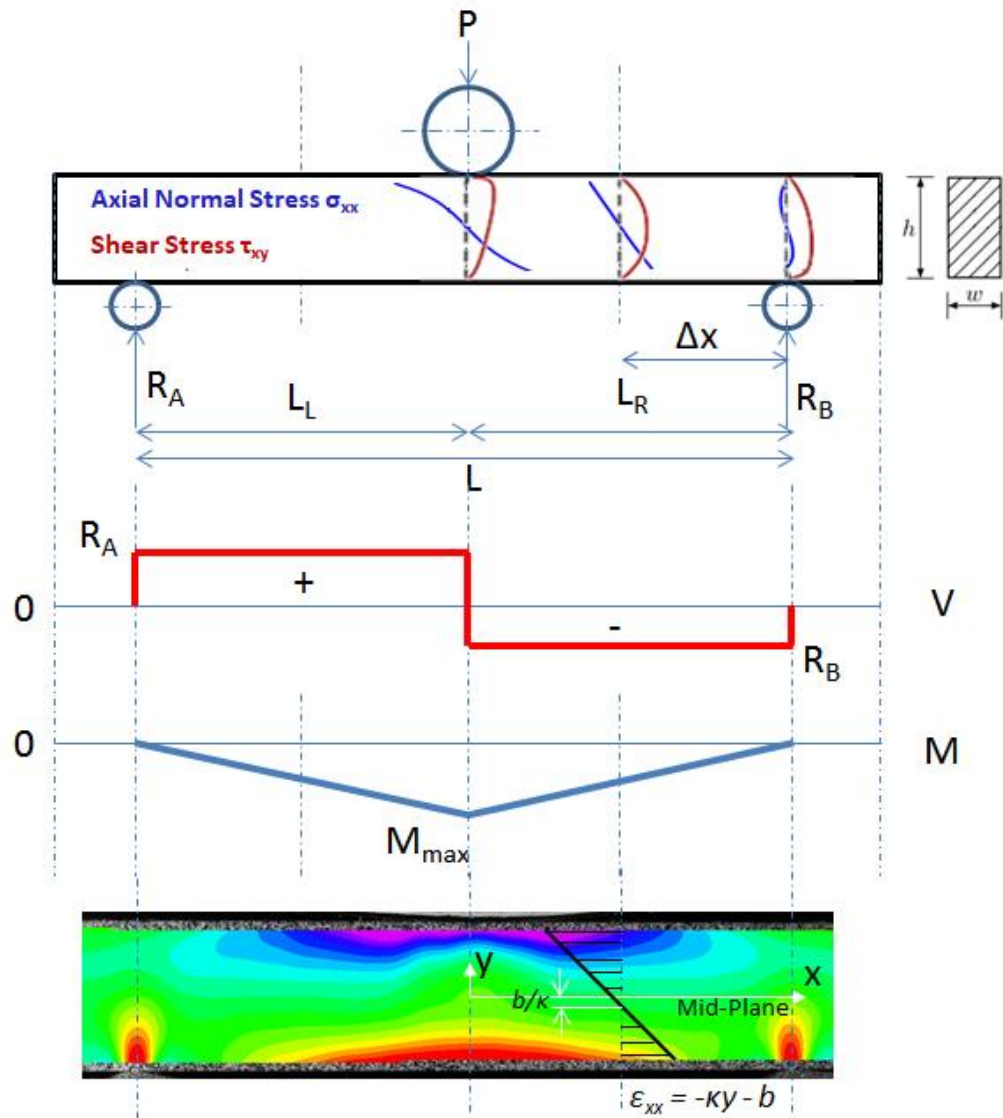


Figure 13. Static Analysis of the 3-Point Bend Test, with Coordinate Notation and Axial Strain Distribution

The shear force diagram in Figure 13 is simplified in a way that all contacts are assumed to be point loads. Regardless, the shear force in the left and right sections are given in the following equations.

$$R_A = P \frac{L_R}{L} \quad , \quad R_B = P \frac{L_L}{L} \quad (2-3)$$

$$M_{max} = P \frac{L_R L_L}{L} M_L = M_R = R_B \Delta x = P \frac{L_R L_L}{L} \frac{\Delta x}{L_R} \quad (2-4)$$

Where the operator decides on the appropriate value of $\Delta x/L_R$ to be away from the points of contact. This may be closer to the loading nose for large beams. A similar analysis is performed on the left side of the specimen. The following equation shows the linear approximation of the axial strains.

$$\epsilon_{xx} = -\kappa y - b \quad , \quad -\frac{h}{2} \leq y \leq \frac{h}{2} \quad (2-5)$$

Note that from this equation, the neutral axis lies at $y = -b/\kappa$. The neutral axis does not coincide with the mid-plane, due to a significant difference between tensile and compressive axial moduli. Solving for the equilibrium equations, the axial moduli are determined to be [15]:

$$E_{T,C} = \frac{M}{\kappa I (1 \mp a)^2} \quad , \quad a = \frac{2b}{h\kappa} \quad , \quad I = \frac{wh^3}{12} \quad (2-6)$$

Where I represents the second moment of area, and κ and b are the slope and intercept from the linear fit of the axial strain through the cross-section. As the value of the intercept b goes to zero, the difference between E_t and E_c becomes smaller and the solution goes to $E = M/(\kappa I)$.

The shear strains are maximum at the neutral axis, as the axial strains are zero. In this region of pure shear, the beam theory equation is used to estimate the shear stress.

$$\tau_{xy} = \frac{3V}{2wh} \quad \text{where} \quad V = \begin{cases} \frac{L_R}{L} P, & \text{if left} \\ \frac{L_L}{L} P, & \text{if right} \end{cases} \quad (2-7)$$

With known strain-stress pairs, the nonlinear parameters for G_{xy} , K_{xy} , n_{xy} are found using nonlinear least-squares curve fitting using the curve-fitting toolbox in Matlab. The robust bi-square option is enabled during the curve-fitting.

The Poisson's Ratio can be found by plotting transverse strains against axial strains in the cross-section. As transverse stress goes to zero away from the contact surfaces, the transverse strains are purely an effect of the Poisson's Ratio. In addition, the strength of the specimen is determined by its failure mode. If the specimen fails at the cross-section under the loading nose, the axial stress is maximum. If the specimen fails under pure shear, the shear stress is equal to the shear strength. If the wrong specimen and fixture geometry is used, the specimen may exhibit mixed-mode failure near the loading nose. Since this is a complex interaction between nonlinear shear and fiber compressive stresses, this topic is considered out of the scope of this thesis.

$$S_{xy} = \frac{3 \max(L_L, L_R) P_{max}}{2 L wh} \quad (2-8)$$

$$S_{xx} = P_{max} \frac{L_L L_R}{L} \frac{h}{2I} \quad (2-9)$$

2.2.2 Theoretical Analysis via Hyperbolic Stress Functions

In 1985, Whitney and Browning solved for the stresses in 3-point and 4-point bend specimens by Fourier series, based on classical theory of elasticity. The solution applies to the setup shown in Figure 13, including overhang. The applied load is represented as an evenly distributed normal pressure over a distance d by

$$f_i(\xi) = \frac{P}{bd} \left(\beta + \sum_{m=1}^{\infty} \sin \frac{p_m \beta}{2} \cos p_m \delta_i \cos p_m \xi \right), \quad (i = 1,2) \quad (2-10)$$

Where $\zeta, \beta, \delta_1, \delta_2$ refer to specimen and fixture geometry, and $p_m = 2 m \pi$. In this application, the solution is sought in the following form of normalized stress distributions:

$$\sigma_\xi = R \left(A_0 + \beta_0 \eta + \sum_{m=1}^{\infty} \mu_m^2 \sum_{i=1}^2 \lambda_i^2 g_{mi} \cos p_m \xi \right) \quad (2-11)$$

$$\sigma_\eta = -\frac{1}{S} \left(2 + \sum_{m=1}^{\infty} p_m^2 \sum_{i=1}^2 \lambda_i^2 g_{mi} \cos p_m \xi \right) \quad (2-12)$$

$$\tau_{\xi\eta} = \frac{1}{R} \sum_{m=1}^{\infty} p_m^2 \sum_{i=1}^2 \lambda_i \left(A_{mi} \frac{\sinh \lambda_i \mu_m \eta}{\sinh \lambda_i \mu_m} + B_{mi} \frac{\cosh \lambda_i \mu_m \eta}{\sinh \lambda_i \mu_m} \right) \quad (2-13)$$

For the solution to this set of equations to the imposed boundary equations, refer to [39].

The hyperbolic functions are assumed to fit the partial derivative model and depends on the material parameters λ_i , which are by their definition elastic. Figure 14 shows the shear stress field as determined in this solution.

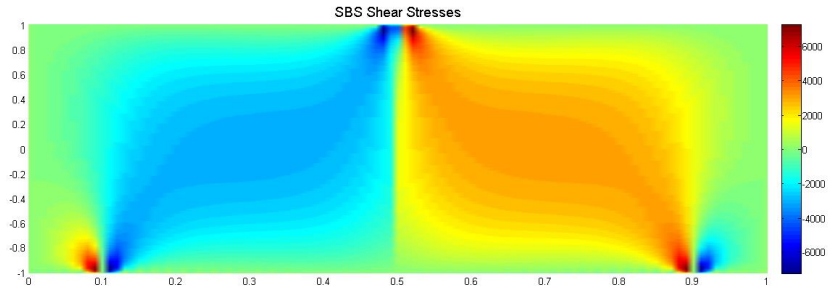


Figure 14. Solution of SBS Shear Stresses by Whitney's Analytical Solution.

The solution is able to capture interesting phenomena that otherwise only an FEA model could pick up. The shear “moustache” shape is evident, showing stress concentrations at the

contact surfaces. Unfortunately, the loading scenario is too simplistic, and the material model is homogeneous and linear. As such, it is of limited practical use for the SBS analysis. It does show that there is a pronounced effect of the loading nose on key analysis parameters. Due to the proximity of the loading nose, the SBS specimens have a slightly lower maximum shear stress. Furthermore, the neutral axis shifts due to very small residual transverse stresses. As such, any SBS specimen will have an artificially large measured difference between tensile and compressive modulus. This effect is shown in Figure 15.

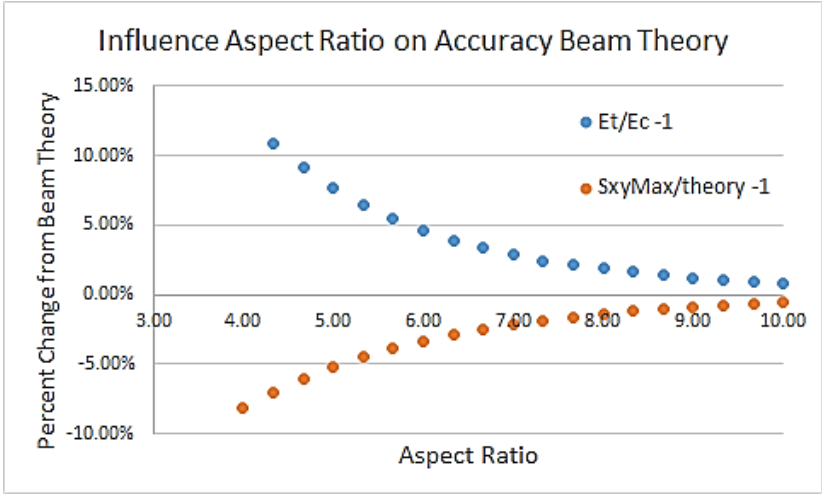


Figure 15. The Whitney and Browning Analytical Model Shows Deviations from Beam Theory at Low Aspect Ratios

Of key interest here is that common SBS specimens are tested in the range of $4 < L/h < 5$. The operator may expect some error when using the analytical solution in the G -, $E_{T,C}$ - moduli. This model shows that instead of finding $E_{T,C}$, the operator should define $E_{average}$ instead. Therefore, there is value in testing long-beam specimens, to which beam equations are more accurate and applicable.

2.3 Multi-parameter Finite Element Method Updating

As per the previous discussion, the closed-form solutions are not adequate for the nonlinear stress-strain analysis applied to the SBS test. As the test is performed, the load and strain fields are measured, with which the certainty depends on the quality of the sensors and the procedure. The desired outcome is a stress-strain relationship, so given the geometry and applied loading, a mathematical model is created to calculate the stress. Since the stress field is heterogeneous, the solution is material dependent, which necessitates the solving of an inverse problem. The reference case shall be the FEMU method, as described in references [38,41]. This section briefly describes the method.

2.3.1 *Finite Element Model*

The FEA model's purpose as described in this chapter is to calculate accurately the stresses at the front surface. These stresses are to be used directly to provide stress-strain relationships, from which the axial, and shear moduli may be derived. The model is parametric and specimen-specific with respect to loading, geometry. A representative model is shown in Figure 16. The loading nose and supports are modelled by analytical rigid surfaces, while the SBS specimen is a solid rectangular extrusion with a homogeneous section. This may only be true for unidirectional coupons, as is the case in this methodology. The orientation of the material corresponds to the material plane as tested.

The structure is meshed with C3D8I elements, which perform well in bending-dominated structures, as they remove shear locking and reduce volumetric locking. The mesh is refined along the top/bottom surfaces and under the contact areas, as these are the locations where stress gradients are highest. One symmetry plane is applied in the x-y plane, without detriment to the

result. The supports have the encastre boundary conditions, while the loading nose is only free to move in the y-direction. The surface-to-surface contact definition is applied to contact regions, with penalty tangential behavior of 0.2 and maximum elastic slip of 0.005 and standard geometric properties. Small amount of contact stabilization was required to obtain a solution, but care is taken that the energy dissipation is not significant.

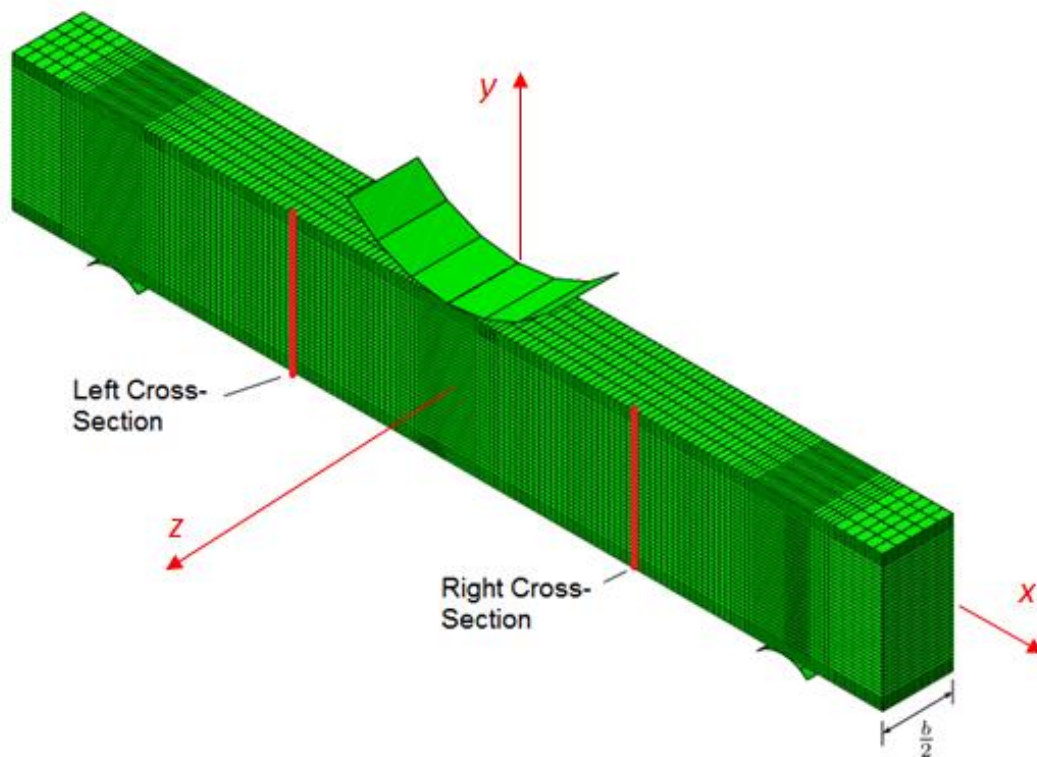


Figure 16. Typical FEA Model for SBS Finite Element Updating Scheme

2.3.2 Finite Element Model Updating Scheme

The objective of this FEMU scheme is to have an agreement between strains as measured in the DIC and as calculated in the FEA model. The chosen parameters for the model are the shear G_{xy} , K_{xy} , n_{xy} parameters, the axial $E_{T,C}$ moduli, and the Poisson's Ratio. After calculating

initial values as per the section 2.2.1, the model is run. The model hits specific load levels that correspond to those in the test. The stresses and strains are extracted along the left and right cross-sections as shown in Figure 16 and used to define new material properties for the next iteration.

The following numerical quantities are replaced by FEA: The slopes for $\frac{d\varepsilon_{yy}}{d\varepsilon_{xx}}$ is compared to the measured and used to adjust the Poisson's Ratio ν_{xy} ; The slope of the axial stress $\frac{d\sigma_{xx}}{dy}$ replaces the calculated bending moment over second moment of area M/I . Edges nodes are excluded from regression analysis, to compensate for a lack of data in the DIC strain fields at the top/bottom surfaces; A linear regression of the FEA axial strains provides the location of the neutral axis, which may not agree with measurements. If $E_{xx,T}/E_{xx,C}$ ratio is too high, the neutral axis in the simulation is too far down. The bimodularity ratio is refined until the neutral axis matches the measurement; One node at the mid-plane represents the maximum (pure) shear stress. The shear stress at this location at each frame replaces the first-order estimate of $\frac{3P}{4A}$. Then, the G_{xy} , K_{xy} , n_{xy} parameters are found by least-squares regression analysis.

Figure 17 shows the logic flowchart of the FEMU program. From the DIC measurements, the user needs to input the geometry, loading data, and measured strain- Y-coordinates pairs at the required cross-section. In the blue block, the stresses are replaced by the new iteration of FEA stresses. From there, the material properties are updated. If the convergence criterium is met, the program ends. That criterium is satisfied if the material properties do not change significantly between iterations:

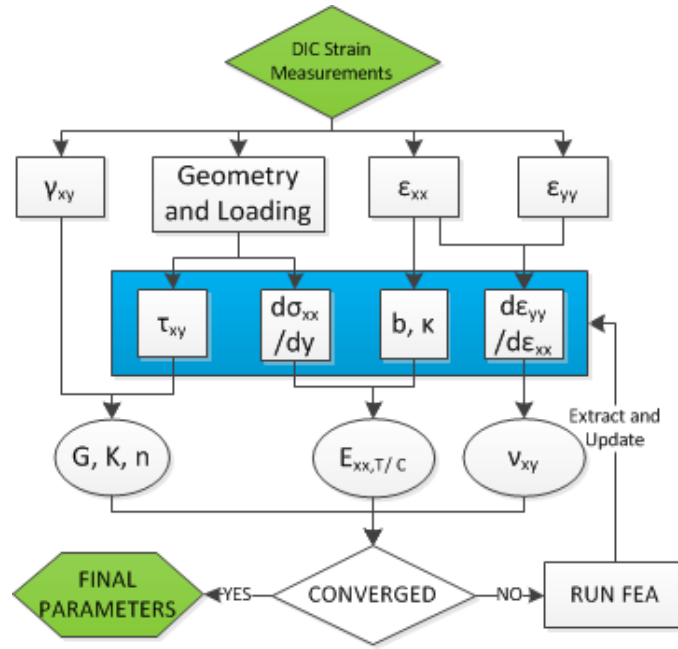


Figure 17. Logic Flow for the FEM Updating Scheme

$$\left(\frac{G_{xy}}{G_{xy0}} - 1\right)^2 + \left(\frac{K_{xy}}{K_{xy0}} - 1\right)^2 + \left(\frac{n_{xy}}{n_{xy0}} - 1\right)^2 + \left(\frac{\nu_{xy}}{\nu_{xy0}} - 1\right)^2 + \left(\frac{E_{xxT}}{E_{xxT0}} - 1\right)^2 + \left(\frac{E_{xxC}}{E_{xxC0}} - 1\right)^2 < Threshold \quad (2-14)$$

Where the subscript 0 refers to reference values. These reference values are arbitrary at the first iteration and later represent the previous loop. Important to note is that the FEA model calculates both sides at the same time. Therefore, the material input properties in the FEA model are defined as the average of the two solutions.

This updating scheme was verified using a batch of four IM7/8552 carbon epoxy specimens tested in the 1-3 plane. These specimens are common in the aerospace industry and have been extensively characterized [29]. Using the beam theory equations, the material parameters calculated do not agree with the reference. The specimens had a width of .25in. and a height of .25in. These were tested at a span of 1.2in., loading nose diameter 4in., and roller

support diameter .25in. The disagreement in outcome is due to the low aspect ratio of these specimens. The four specimens equate to 8 data sets. All other test settings were as recommended in section 2.1. For the FEMU scheme, the threshold value is set to 1%.

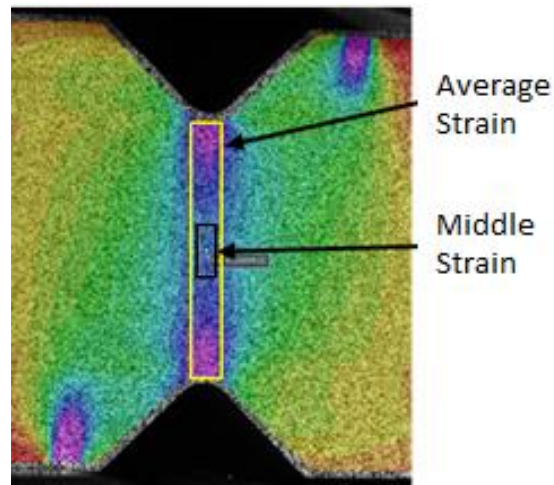


Figure 18. Virtual gage areas simulated by DIC in the ASTM D5379 V-notched specimen.

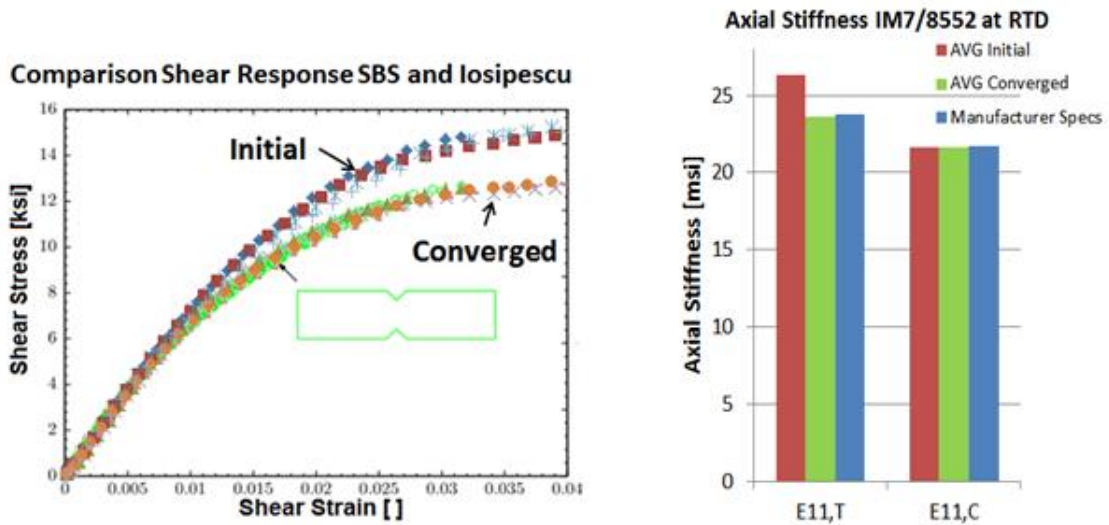


Figure 19. Comparison of Material Properties as Calculated using Beam Theory (Initial), after FEMU (Converged), and Reference

Table 2. Convergence of Material Properties of IM7-8552 Batch, Compared to Reference

Iteration	E _{11,T}	E _{11,C}	ν_{13}	G ₁₃	K ₁₃	n ₁₃
A1:1	2.64 E+07	2.11 E+07	0.347	7.74 E+05	2.94 E+04	.199
5	2.36 E+07	2.13 E+07	0.423	7.36 E+05	2.61 E+04	.174
A2:1	2.62 E+07	2.18 E+07	0.334	7.74 E+05	2.80 E+04	.191
4	2.35 E+07	2.17 E+07	0.424	7.36 E+05	2.47 E+04	.165
A3:1	2.64 E+07	2.26 E+07	0.290	7.99 E+05	3.00 E+04	.205
4	2.35 E+07	2.23 E+07	0.387	7.58 E+05	2.71 E+04	.184
A4:1	2.64 E+07	2.09 E+07	0.309	7.85 E+05	3.22 E+04	.220
4	2.36 E+07	2.12 E+07	0.462	7.42 E+05	3.07 E+04	.208
AVG 4	2.36 E+07	2.16 E+07	0.424	7.43 E+05	2.71 E+04	.183
Hexcel	2.26 E+07	2.07 E+07	0.333*	6.8 E+05**		
COV [%]	[1.7	6.4		3.7		

* Average of Poisson's Ratio from tensile and compression test

** G12 cited as reference, tested with $\pm 45^\circ$ off-axis tensile test

Figure 19 and Table 2 show the performance of this FEMU tool. The initial estimate comes from the beam equations. The converged solution is after FEMU. The shear nonlinear properties are compared to reference data from the Iosipescu shear test (Figure 18 [36]). While the Iosipescu specimens are more expensive to run, they are well known for giving accurate shear stress-strain properties. These results show that the SBS specimens can reach the same quality result via advanced analysis tools. The axial properties are compared to reference values by Hexcel and demonstrate a better match, mainly by reducing the ratio between the tensile and compressive modulus. The results for the Poisson's Ratio were less impressive, due to the low

strain levels being noisier data. There is also an outsized influence of proximity to the loading nose.

In conclusion, the FEMU method serves as the reference case of the material parameters moving forward. This iterative method substitutes stresses from the closed-form solution with those found in the FEA, creating a more accurate solution. It reduces the shear stresses, which are otherwise too high. The method also corrects for the aspect ratio effect on the neutral axis. There is on the other hand less benefit to apply this model to long beams and the results did also not compare favorably for the Poisson's Ratio.

FEA is a powerful tool to analyze virtually any geometry and loading and FEMU can incorporate large amount of overdetermined data. Even though most sources in this study use the FEMU method to solve the inverse problem of parameter identification, the solution is usually approximately solved due to experimental, discretization and modeling errors [51]. The FEMU model shown uses a small subset of the total measured strain field. A different FEMU iteration scheme was developed by Cline and Seon [40], which uses strain matching between FEA and DIC. The material parameters are changed by use of a Jacobian matrix. These FEMU models can only characterize the material model specified and there is still need for a nonupdating tool for material characterization which allows for any arbitrary material model.

2.4 Direct Optimization Method

2.4.1 *Observations and the Applicability of Assumption*

The equations as described in section 2.2.1 are based on the observation that axial strains are linear through the cross-section. This is certainly true for long beam specimens, but not necessarily true for the SBS specimens. Consider Figure 20, which shows a part of a parametric study on the influence of the aspect ratio and tensile/compressive moduli ratio in the test specimen. Note that the SBS specimens (with aspect ratio $L/h = 4.8$) has nonlinear stress distribution. Worse, for specimens with no difference in tensile/compressive modulus, the model does show the intercept is nonzero. This neutral axis does shift when bi-modularity becomes more significant.

Of note is the high sensitivity of the axial properties to the position of the neutral axis. A small deviation due to measurement uncertainty has a disproportional influence on the result (Figure 15). Furthermore, an attempt was made to create a bi-linear fit to separate tensile and compressive modulus [38]. This method did not mathematically make a difference, as the underlying assumption of plane stress dictates the solution. Therefore, the combination of low aspect ratio, very large shear stresses, and proximity of the loading nose leads to a combination where the assumption of planar stresses is not valid.

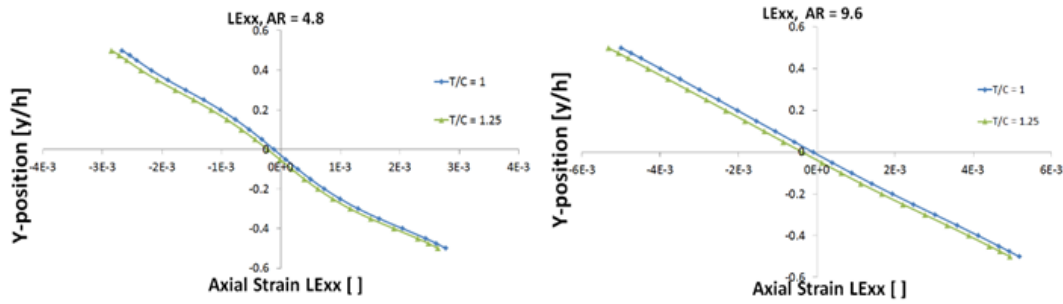


Figure 20. Effect of Aspect Ratio and Tensile/Compressive Modulus Ratio on Axial Strain Distribution

By extension, the derivation of the shear stress distribution cannot be accurate either. The notion that shear stresses are parabolic through the cross-section depends on the axial stresses to be linear. By observation and simulation, shear strains are roughly parabolic through the cross-section. However, this would not be possible in the combination of parabolic shear stress distribution and highly nonlinear stress-strain relationship. This counterargument is supported by Figure 21. Other assumptions (plane stress state, small displacements) have been verified using FEA.

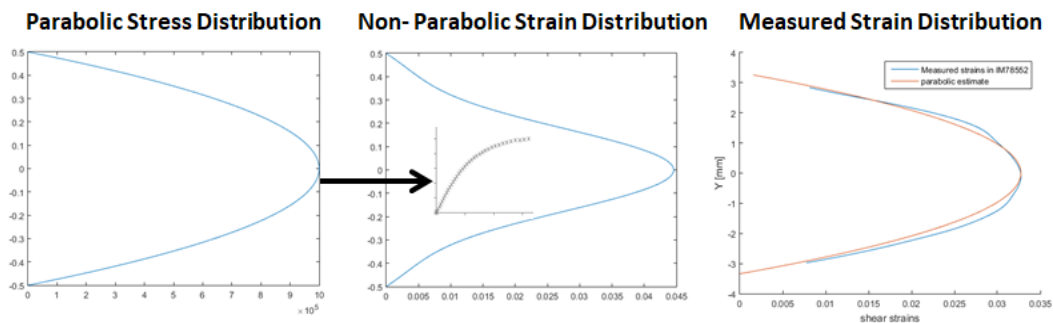


Figure 21. Parabolic Stress Distribution is Incompatible with Measurements

2.4.2 Optimization Model

Closed-form solutions are often based on invalid assumptions. Most often, analysts assume linear elastic behavior and transverse isotropy for composite plies. Only rarely are heterogeneous stress states entirely material independent. When it comes to identifying material parameters, attempting to solve these equations using iterative methods is a logical step. However, these iterative methods will be expensive to perform; the operator or experimentalist will have to use dedicated software (FEA) on powerful computers and have a lot of available time and expertise to get the correct answer. Instead, consider the following set of equilibrium equations (assuming body forces are negligible).

$$\begin{aligned} t_i &= \sigma_{ij}n_j && \text{on } S_f \\ \sigma_{ij,j} &= 0 && \text{in } \Omega \\ \sigma_{ij} &= \sigma_{ji} && \text{in } \Omega \end{aligned} \quad (2-15)$$

where t_i is the applied traction on the surface S_f . σ_{ij} are the stress combination in the domain Ω of the specimen and has to satisfy the balance of forces and moments. Consider the kinematic compatibility equations:

$$\begin{aligned} \varepsilon_{ij} &= \frac{1}{2} \left(\frac{\delta u_i}{\delta x_j} + \frac{\delta u_j}{\delta x_i} \right) && \text{in } \Omega \\ u &= \bar{u} && \text{on } S_u \end{aligned} \quad (2-16)$$

where u is the displacement vector, and \bar{u} is the applied displacement on surface S_u . The constitutive equation is given as

$$\sigma_{ij} = C_{ijkl}(\sigma_{ij})\varepsilon_{kl} \quad \text{in } \Omega \quad (2-17)$$

with C_{ijkl} being the Hooke tensor. To note its nonlinear behavior, it is noted as being a function of applied stress. The general idea is that with DIC, the surface displacement field \bar{u} is

calculated from tracking of the speckling pattern during deformation of the surface. Using the previous equations, the Cauchy infinitesimal strain tensor is calculated. For the remainder of this proposal, “strain” shall be defined as engineering strain, so the shear strain is multiplied by a factor of 2.

On the other hand, the applied traction will be considered as a known quantity, resulting in a traction load, which manifests itself within the body as applied stress. Using the force equilibrium equation, a set of integrals is defined with which the integral of stress is set equal to the applied loading case. The specifics of this integral depend on the loading case, as it can manifest itself in a body as a normal force $N_{\alpha\beta}$, a shear force V_α , or a bending moment $M_{\alpha\beta}$ in any direction.

The first method to solve for $C_{ijkl}(\sigma_{ij})$ is using optimization algorithms. To solve this set of equations, start with displacement field measurements across multiple load/deformation levels. Note for each frame the applied loads. Next, define the engineering strains on the surface. Then, define stress as a function of strains as:

$$\sigma_{ij} = f(\varepsilon_{kl}) \quad (2-18)$$

Stress is purposely left as an arbitrary function of strain. The analyst may choose any preset model that works or create a tabular form of stress-strain and use spline tools to make the conversion. The variables in eq. 3-4 to identify are called [X]. Curve fitting is always possible after optimization. The temporary stress field is computed using an initial guess for the material parameters.

The next step is to apply the applicable integration across any cross-sectional or surface stresses that physically must equal the applied load. These integrals are to be derived from the

force balance equation 3.1. For every stress field m , you can then have integrated normal force $(N_{\alpha\beta})_{sum}$, shear force $(V_{\alpha})_{sum}$, and bending moment $(M_{\alpha\beta})_{sum}$. The subscript “sum” denotes that for numeric data, the integration usually is a summing operation.

The objective is then to create a cost function $f([\theta])$ to evaluate the difference between the applied $N_{\alpha\beta}$, V_{α} , and $M_{\alpha\beta}$ and the integrated values for each selected load level. Constraint functions $(A, Aeq, b, beq, c([\theta]), ceq([\theta]))$ and limits (lb, ub) can also be set up to guide the solution. The analyst is free to select a programming solver to minimize $f([\theta])$ while satisfying the constraints imposed. One example of such is the function “fmincon” by Matlab that finds the minimum of a problem specified by

$$\min_{\theta} f([\theta]) \text{ such that } \begin{cases} c([\theta]) \leq 0 \\ ceq([\theta]) = 0 \\ A \cdot [\theta] \leq b \\ Aeq \cdot [\theta] = beq \\ lb \leq [\theta] \leq ub \end{cases} \quad (2-19)$$

A simpler method exists for linear stress-strain relationships, where optimization is possible, but more than sufficient. A linear property such as matrix tensile modulus and fiber tensile, compression modulus, only require one load-frame to get a solution. Equation 3-4 simplifies to become

$$\sigma_{ij} = E(\varepsilon_{ij}) \quad (2-20)$$

which simplifies the process considerably. The integral equation derived from eq. 3-1 can then be rewritten to integrate measured strain values directly. The integral equation can then be used to solve for E using algebraic operations. Good practice is to apply this calculation to each load-frame, to see if the solution does not vary with applied load level.

2.4.3 Implementation in SBS Test

While the methodology works for different test methods, it must be tailored to the specific test and the measurements. The only thing measured during the SBS test is the applied load and the surface strains. From there, we get two very distinct objectives: to match the applied shear force and applied bending moment.

The material model chosen in this application is tabular. The conversion of measured strain to virtual stresses is done via cubic spline, consisting of stress-strain pairs. The strain data points are chosen at $2000\mu\epsilon$ intervals, such that the corresponding stress data points are the variables $[\theta]$ to be optimized. The number of data points must be large enough to capture the nonlinear behavior accurately. On the other hand, small intervals between data points leads to erratic behavior. Noise in the data leads to data points not being exactly on the material curve. As the spline must go through each data point, and still be piecewise continuous, it will appear to oscillate and deviate widely from the general trend.

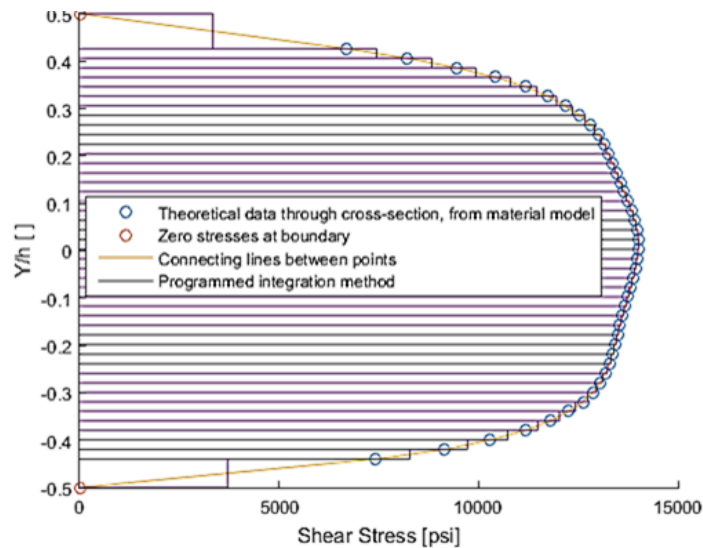


Figure 22. Graphical Representation of Integrating Shear Stresses through Cross-Section

The next step is to convert measured strains to virtual stresses. Physically, the integration of shear stress over the specimen cross-section must equal the applied shear force. Figure 22 shows the distribution of shear stresses through a cross-section and the integration scheme. Note that DIC data is incomplete at the edges, so extrapolation is necessary and shown as well. Numerical integration using trapezoidal steps is performed to calculate a virtual shear force V_{sum} . Assuming no stress variation through the width and small deflections, the following optimization scheme is set up. It is important to emphasize that the material model applies to all strain data points in all the frames.

$$\tau_i = f(\gamma_i) \quad (2-21)$$

$$V_{sum} = w \int_{-\frac{h}{2}}^{\frac{h}{2}} \tau dY = \sum_{i=2} \left[\tau_{i-1} + \frac{1}{2}(\tau_i - \tau_{i-1}) \right] (Y_i - Y_{i-1}) \quad (2-22)$$

$$\min_X \sum (V_{sum_i} - V_i)^2 \quad (2-23)$$

Where τ_i and γ_i represent shear stress and strain, respectively. The index represents each point as measured through the cross-section. The virtual shear force is calculated for each load frame and compared to V_i , the applied shear force. The initial error using the closed-form solution represents a mismatch between applied shear force and what would be the internal stress-state with the calculated material model. After optimization, this error is greatly reduced to noise-level.

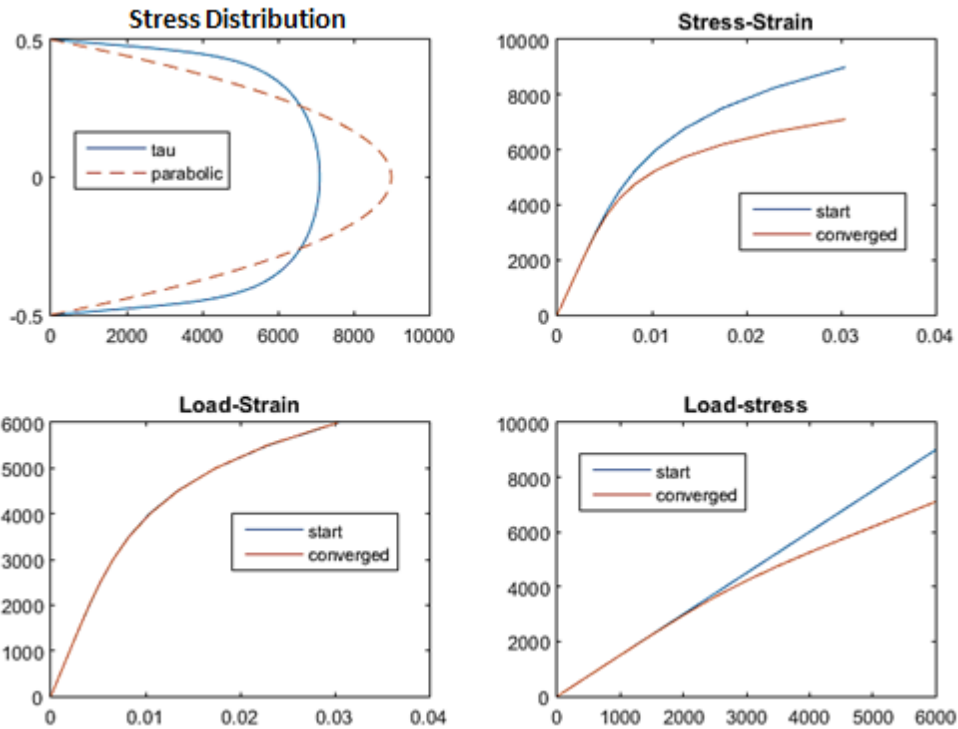


Figure 23. Trends Captured using Shear Stress-Strain Optimization in SBS Specimens

The implications of the optimization scheme lead to a new set of trends that corresponds well to what is observed from the FEMU analysis (as shown in Figure 23). The stress distribution across the cross-section flattens out to become less parabolic and the maximum stress does not correspond linearly with maximum load anymore. Most importantly, the shear stress-strain curve is adjusted. All the while, nothing changes in the relationship of load vs maximum strain, as these are the measured properties.

The analysis as performed for the axial modulus is similar. The axial strain distribution through the cross-section is transformed to the axial stress distribution via a spline material model via the following equation. Note this is not necessarily linear.

$$\sigma = f(\epsilon) \quad (2-24)$$

Note this equation is a very simplified 1-D version of Hooke's law. In this case, the σ_{zz} and σ_{yy} are both equal to zero, which simplifies the equation. For this application, the integral of the $\sigma_{zz} \cdot Y$ must equal the bending stresses. According to the equilibrium equations, the integral of σ_{zz} must also equal net axial force. Unfortunately, noise in the system makes optimization for both targets hard to achieve. Because the bending moment is defined at multiple load steps, the problem is over-defined and of acceptable accuracy.

Figure 24 shows an example of axial strains through the cross-section. Normalized axial strain data come from a 1mm wide band, instead of 2mm to reduce noise. About 300-400 data points are usually present. Extrapolation of the DIC data is necessary to fill in the strain at the free edges. Regression of last (or first) k many data points gives a line equation used to predict ϵ_{xx} at $\pm h/2$. Since these strains are nonzero, this part of the solution is significant. The data points represent a piecewise linear line as shown. The line equation for stress is given as follows and used to derive the integral (numerical summation) and objective function for the optimization algorithm.

$$\sigma = mY + b = \frac{\sigma_i - \sigma_{i-1}}{Y_i - Y_{i-1}}Y + \frac{\sigma_{i-1}Y_i - \sigma_i Y_{i-1}}{Y_i - Y_{i-1}} \quad (2-25)$$

$$\begin{aligned} M_{sum} &= w \int_{-\frac{h}{2}}^{\frac{h}{2}} \sigma Y dY \\ &= \sum_{i=2} \left[\frac{1}{3} \frac{\sigma_i - \sigma_{i-1}}{Y_i - Y_{i-1}} (Y_i^3 - Y_{i-1}^3) + \frac{1}{2} \frac{\sigma_{i-1}Y_i - \sigma_i Y_{i-1}}{Y_i - Y_{i-1}} (Y_i^2 - Y_{i-1}^2) \right] \end{aligned} \quad (2-26)$$

$$\min_x \sum (M_{sum_i} - M_i)^2 \quad (2-27)$$

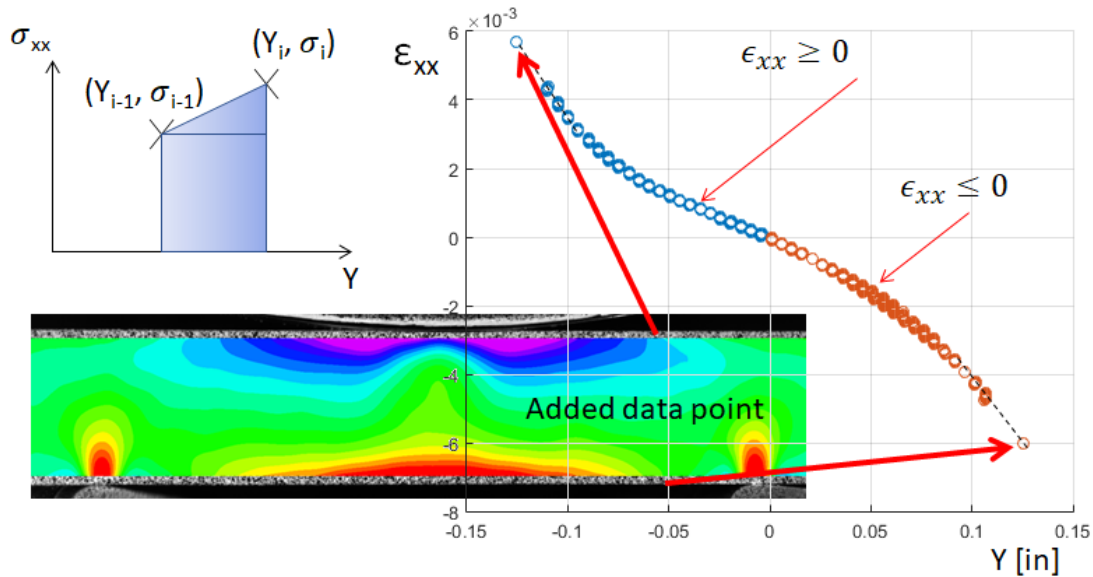


Figure 24. Axial Strain and Stress Distribution with Extrapolation

2.4.4 FEA Verifications and Sensitivity Analyses

Usefulness, accuracy, and reliability of this method was established by means of virtual test, comparison of test analysis, and sensitivity study to analysis parameters. The virtual test uses the FEA model as illustrated in section 2.3.1. The model was first run using typical values for a fiber reinforced epoxy composites ($G = 757\text{ksi}$, $K = 45.2\text{ksi}$, $n = 0.292$). After running the specimen, the surface strains at the cross-section of interest are exported for analysis and represented the measurement data. Results of the first-order analysis and the optimization analysis are shown in Figure 25. The initial estimate for shear stress is not accurate, and widely overstates the nonlinear stress-strain curve. However, the input stress-strain relationship is recovered accurately after the optimization analysis. The G-K-n Ramberg-Osgood parameters vary (Table 3), which is a weakness of the Ramberg-Osgood equation: One curve can be characterized by different G-K-n combinations.

Table 3. Results of the Virtual Test: Tabular Data for G_{xy} , K_{xy} , and n_{xy} .

	Input	3P/4A	Optimized
G_{xy}	757000	783321	725736
K_{xy}	45200	49999.99	44478
n_{xy}	0.292	0.275798	0.288

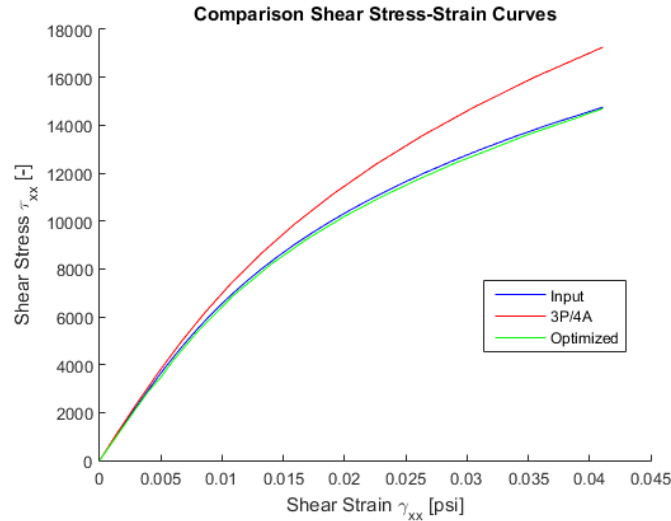


Figure 25. Results of the Virtual Test. The Nonlinear Material Model is Recovered using Optimization Analysis

After verification of the optimization model, this has been applied to a batch of 5 IM7/8552 specimens tested in the 1-2 and 1-3 plane. Testing parameters have been kept identical to that tested for the data in section 2.3. Results of the optimization analysis are shown in Figure 26 and a comparison of the three methods (first-order, FEMU, optimized) in Figure 27.

Figure 26 shows that the amount of scatter is not necessarily increased, but results depend on the amount of noise in the full-field strain measurement data. The optimized axial stress-strain plot is a continuous curve from ϵ_{\min} to ϵ_{\max} , going from negative to positive. A typical result is shown for one specimen. Notably, the result agrees well with a linear slope, as fibers have very linear stress-strain response. The slope of this line usually agrees also very well with the average

modulus as defined by the closed-form solution. As such, it confirms that the SBS is best used for average tensile modulus, rather than a separate tensile/compressive modulus.

Figure 27 shows an excellent agreement of the optimization and FEMU model up to 2.5-3%. As such, the nonupdating method is a vast improvement over the first-order approximation. The disagreement may be a result of the flexibility of the spline-based tool to adjust to highly nonlinear behavior. On the other hand, the optimization model uses more DIC data to obtain its result, and thus may be more influenced by noise-related factors in the data.

Among the factors studied in the sensitivity analysis, the following three factors were deemed significant: extrapolation of DIC strain measurements to correct for missing data, subset size of DIC analysis and choice of cross-section for optimization analysis.

Extrapolation of DIC data is necessary to account for missing data in the strain field. At the edges, significant axial strains are present, but not measured. These form a significant part of the integral. Consider the extrapolation points as shown in Figure 24. It is plausible this method could be only 5% accurate, so the effect of this accuracy is shown in Table 4. If the edge strains are really 5% higher than as analyzed, the measured modulus is overestimated by 1%. If the edge strains are 5% lower, the modulus is underestimated by 1%. As such, the sensitivity to this analysis choice is low.

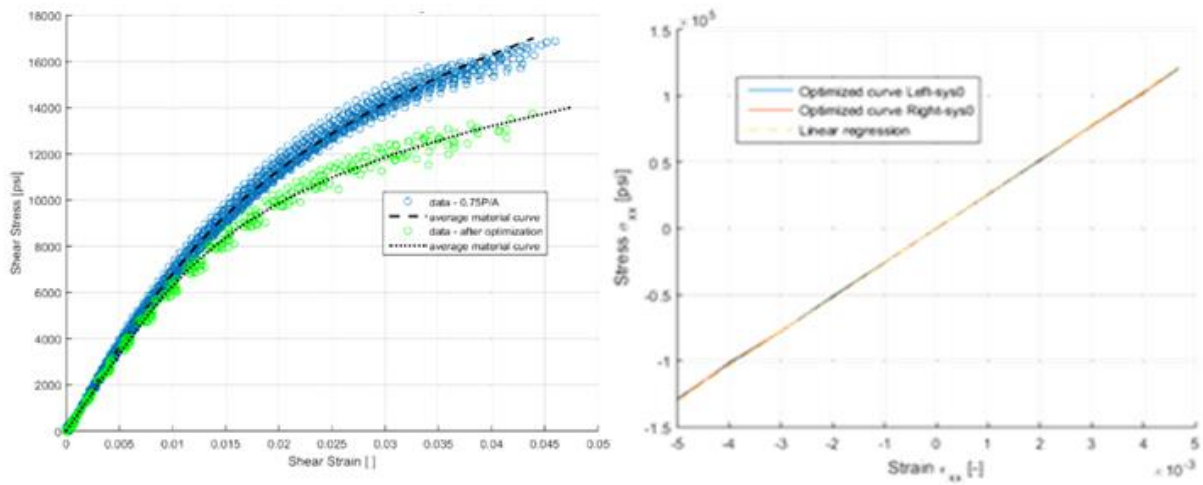


Figure 26. Results of the Optimization Analysis IM7/8552 SBS Specimens (1-3 Plane)

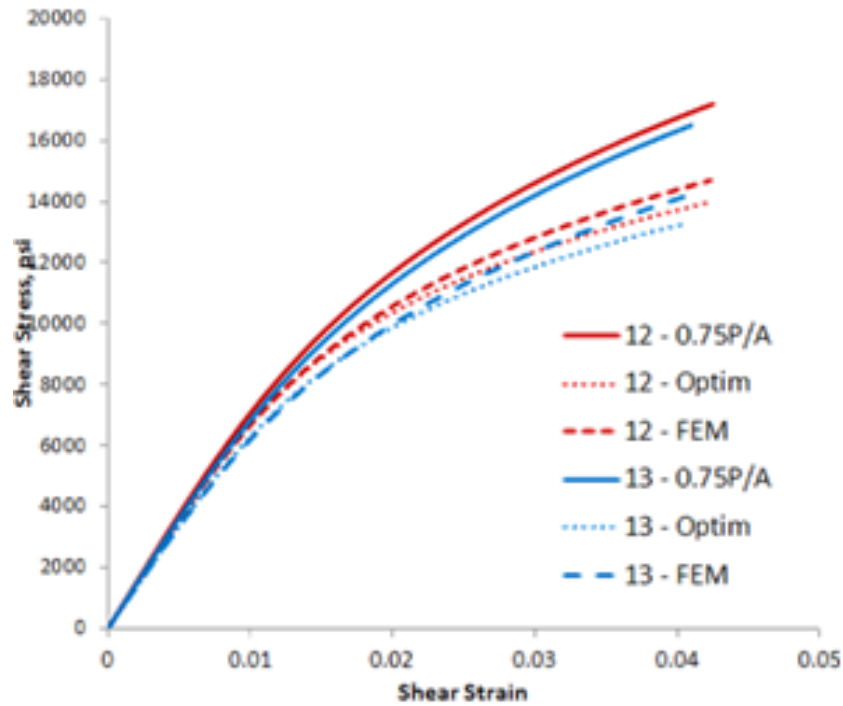


Figure 27. IM7/8552 SBS Analysis. FEMU agrees well with Optimization Analysis

Table 4: Sensitivity Study of Extrapolated Axial Strain Nodes

	Edge Nodes * 1.05			Edge nodes * 0.95		
	ExxT	ExxC	ExxAVG	ExxT	ExxC	ExxAVG
Left	-1.0%	-0.9%	-0.9%	1.1%	0.9%	1.0%
Right	-1.0%	-0.8%	-0.9%	1.0%	0.9%	0.9%
AVG	-1.0%	-0.8%	-0.9%	1.0%	0.8%	0.9%

The second analysis choice is the subset size in DIC. The subset size influences the strain gradients that may be captured. A finer subset size allows for more spatial resolution and capturing large strain gradients. On the other hand, the speckle pattern and camera resolution must be able to support the chosen subset size. For a more accurate discussion, refer to [92]. Figure 28 shows two choices for a subset size in the SBS analysis. The left image has 10 subsets through the thickness, 45pixels. The latter has 13, and only 35 pixels per subset. The respective difference is quantified in Table 5.

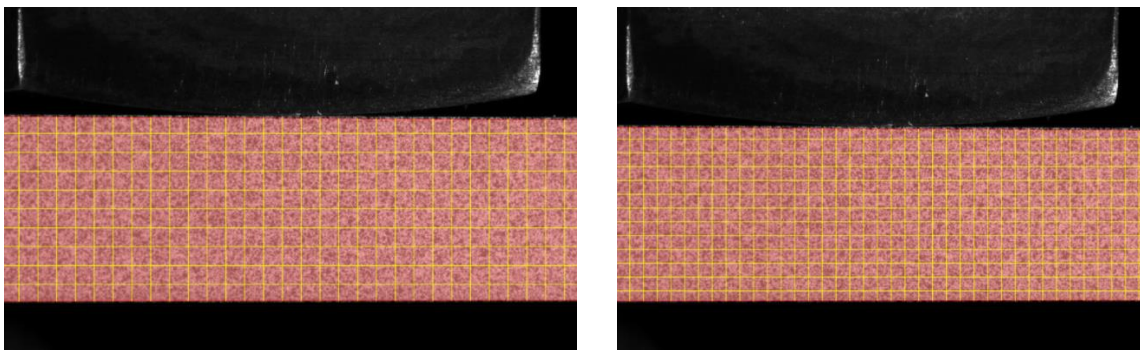


Figure 28. Sensitivity Analysis: Two Choices for Subset Size

Table 5. Sensitivity Analysis: Analysis Difference between Subset Size

	G	K	n	ExxT	ExxC	ExxAVG
Left	-0.6%	0.2%	0.3%	1.5%	1.8%	1.7%
Right	-0.4%	0.3%	0.4%	-2.0%	-0.5%	-1.5%
AVG	-0.5%	0.2%	0.3%	-0.5%	0.8%	0.1%

Again, the sensitivity to subset size is not very large, as the measured strain gradients are modest compared to the capability of the DIC system. The last variable is the choice of cross-section with respect to the loading nose. Consider $\frac{\Delta x}{L_R}$ in Figure 13. Set at 0%, it is at the support locations. Here, bending moment and shear force are zero and stresses of the contact are high. Set at 100%, bending moment is maximum, shear force is zero, and contact stresses are high. 50% works well for SBS specimens, but analysis for long beam specimens could be closer to 80% benefit of higher axial strain measurements. How does the choice of $\frac{\Delta x}{L_R}$ influence SBS analysis? For typical specimen dimensions as discussed, the following conclusions are drawn:

- Shear optimization gives similar results between $10\% < \frac{\Delta x}{L_R} < 60\%$
- Axial properties calculations are consistent between $30\% < \frac{\Delta x}{L_R} < 60\%$
- Poisson's Ratio is affected by stresses near the contacts; use $40\% < \frac{\Delta x}{L_R} < 50\%$

At 40%, the bending moment is lower, but axial strains have a more linear distribution through the cross-section. At 60% the bending moment is higher, but strains are less linear. As results at 40% seem more promising, a comparison is shown in Table 6. The results of the analysis of IM78552 1-2 Plane analysis agree better with the reference parameters [29], but

scatter is higher and results do not necessarily improve. As such, the choice of cross-section is up to the user.

In conclusion, the presented optimization model has great benefits over the FEMU model, considering it is a flexible approach, uses more data across many frames, is nonupdating, very fast, and has very intuitive guiding equations. It is also much more accurate than the first-order analysis. The shear properties found in this analysis method are not very sensitive to model and analysis parameters, and the axial modulus is easily derived from the results. However, the average modulus is not significantly different from that found by closed-form beam equations and thus not improved compared to the FEMU. It does, however, use more data from the DIC strain field, increases confidence, and does verify whether the stress-strain relationship is linear. Note the applicability of the optimization analysis: It applies to homo- and heterogeneous strain fields, with well-defined equilibrium equation for the objective functions and for specimens subject to plane strain/plane stress state.

Table 6. IM7/8552 SBS Analysis: Comparison of Choice $\frac{\Delta x}{L_R}$

Property	$\frac{x}{L_L} = 40\%$			$\frac{x}{L_L} = 50\%$		
	12-plane	13-plane	COV	12-plane	13-plane	COV
E_{xxT}	24.0 Msi	26300000	7.4%	25700000	26000000	4.5%
E_{xxC}	19.7 Msi	19300000	4.1%	19900000	19300000	3.5%
E_{avg}	21.8 Msi	22800000	4.0%	22400000	22200000	1.7%
ν_{xy}	0.32	0.31	13.5%	0.3	0.3	11.9%

CHAPTER 3

CHARACTERIZING NONLINEAR SHEAR LAMINA PROPERTIES

DIC-based advanced measurement techniques are effective for material characterization and can be used to verify simplifying assumptions. One notable assumption is the transverse isotropic approximation, which assumes that shear nonlinear behavior in the 1-3 plane is the same as that in the 2-3 plane and depends on shear stress-strain curves in the 1-2 and 1-3 plane to be very similar to each other. The industry standards are currently not able to adequately measure shear nonlinear behavior in the 2-3 plane due to early other failure modes [3]. Some polymeric composites may exhibit anisotropic shear response; thus, this assumption should be verified.

This chapter presents an analysis and comparison of different experimental methods to characterize shear stress-strain behavior in all three material planes. DIC data-driven methods developed at AMSL are the SBS and Small-Plate Twist (SPT) method. This work was performed as part of a project in collaboration with the Boeing Research & Technology group, developing novel test and inspection techniques to determine what input properties are needed for progressive damage analysis (PDA) methods. This work was an effort to develop verification and validation guidelines based on experimental mechanics, inspection fidelity, and method formulation. Results for these two methods will be compared to the industry standard $\pm 45^\circ$ laminate tensile test to determine accuracy and usefulness of this method.

3.1 Small Plate Twist and Verification of Transverse Isotropy Assumption

3.1.1 Test Method and Analysis

While the SBS method can characterize nonlinear shear behavior in the 1-2 and 1-3 plane, it is unable to do so for the 2-3 plane. Due to the absence of fiber reinforcements in the axial direction, these specimens fail under axial stress before reaching significant shear strains. The same principle applies in the 3-2 plane, in which interlaminar tension is the primary failure mode. However, out-of-plane shear properties in the 1-3 and 2-3 plane are necessary to accurately predict delamination failure and matrix cracking in PDFA methods. In order to measure shear nonlinear behavior in every plane, the SPT test was developed [40,95]. A small, rectangular plate is twisted in all four corners, generating shear strain in each material plane without prohibitive tensile stresses in the matrix. Using DIC-based strain measurements and FEMU methodology, all three shear stress-strain behaviors are characterized at the same time, in the same specimen.

Figure 29 and Figure 30 shows the test setup, including three stereo vision DIC systems. Each camera set measures a material plane and is synced with the other cameras. While testing IM7/8552 specimens, the strains measured reach about 5% in the 1-2 and 2-3 plane, and 3.5% in the 1-3 plane. As there is no closed-form solution for the deformations at the surface of a small plate twist specimen, data-driven modeling is a necessity. The iterative FEMU as shown in Figure 31 was used to solve for the Ramberg-Osgood shear parameters for the tests performed. The method as developed by Seon optimizes material parameters until the error between the virtual and measured strain fields is minimized. More details can be found in reference [40].

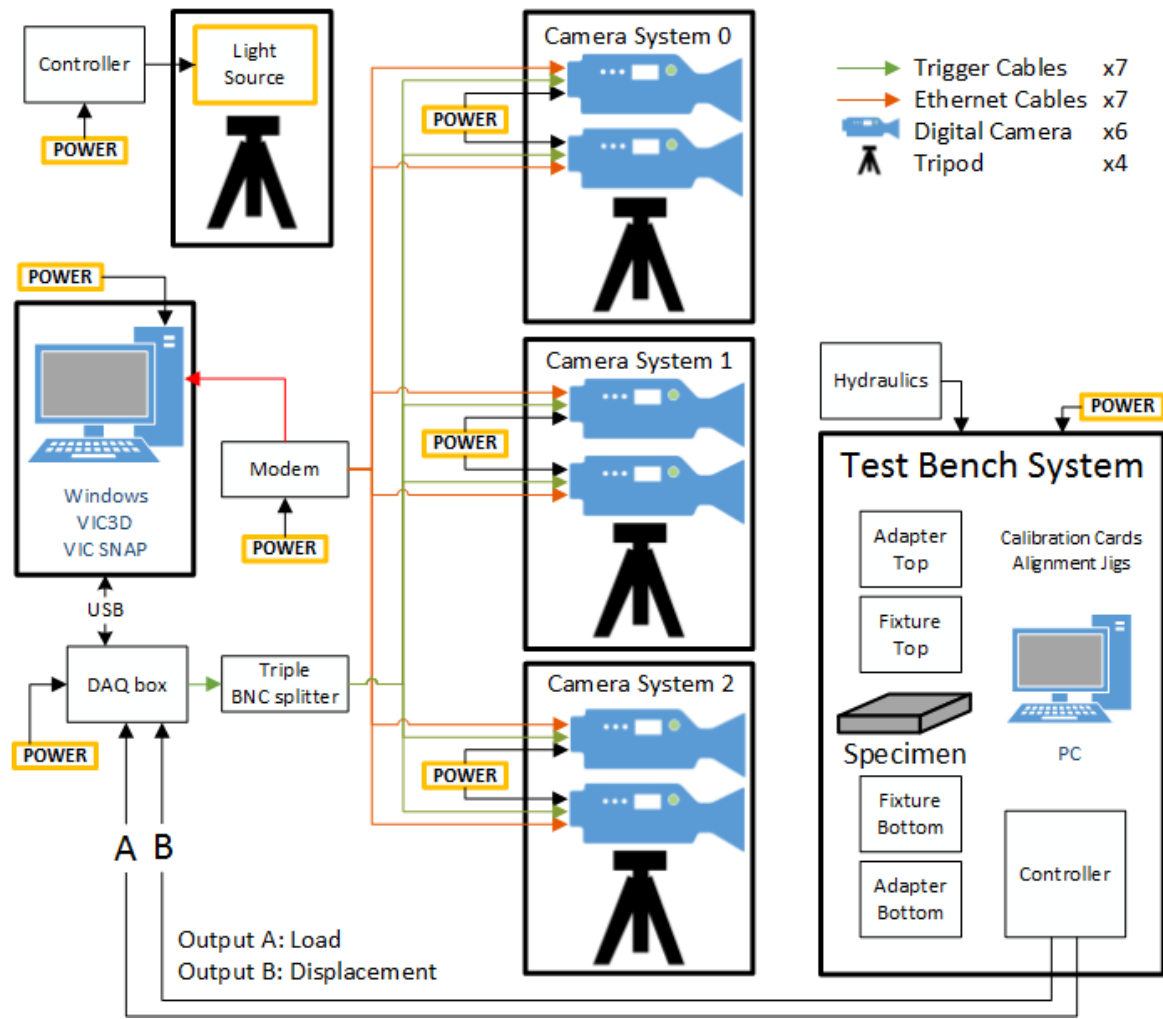


Figure 29. Small Plate Twist Test Hardware Setup

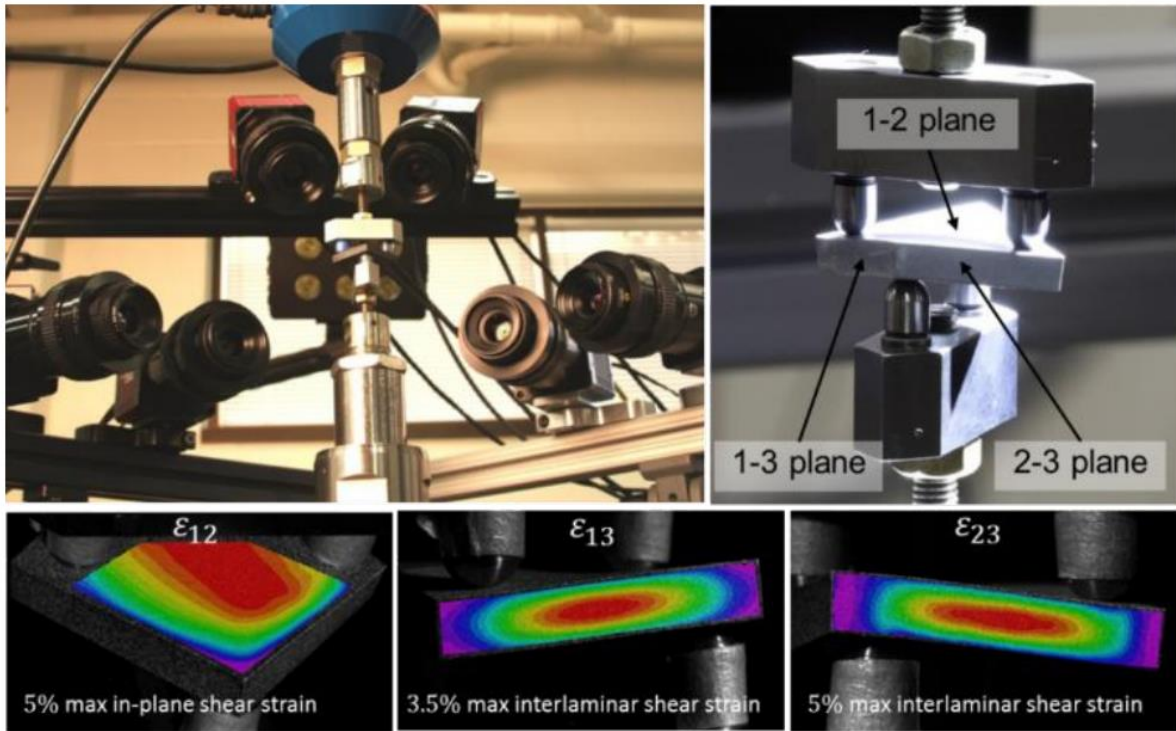


Figure 30. Small Plate Twist Test, showing three Stereo Vision DIC Systems, Fixture, Specimen, and Measured Strain Fields in all three Principal Material Planes

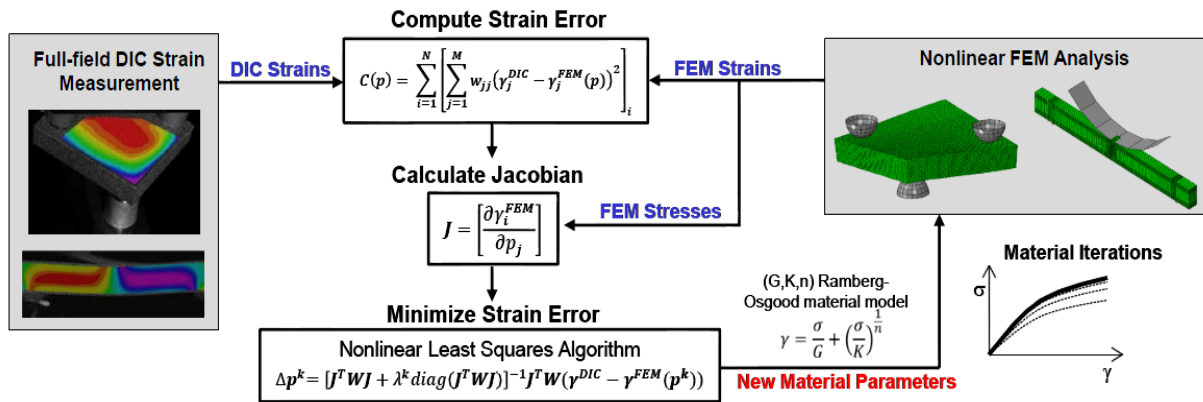


Figure 31. Finite Element Model Updating (FEMU) Iterative Method for Characterizing Nonlinear Shear Stress-Strain Parameters [40]

3.1.2 Characterization of Lamina Properties

For this project, the DIC data-driven methods of the SBS and SPT were applied to the legacy IM7/8552 carbon-epoxy composite and a nondisclosed material system which will be referred to as “material X”. Each material system was subject to the same testing procedure; three batches of five 1.75 x .25 x .25in. rectangular SBS coupons to be tested in the 1-2, 1-3, and 2-3 planes; SPT specimens 2.5 x 2.5 x .25in. and 1.5 x 1.5 x .25in. machined from the same panel as the SBS coupons.

Table 7. Comparison Average Lamina Properties IM7/8552; SBS Method with Optimization and Standard Test Methods

Lamina Material Property	SBS Test Method (COV)	ASTM Standard Test (COV)
Young’s modulus, $E_{average}$	22.7 Msi (1.7%)	22.0 Msi (2.0%)
Young’s modulus, E_{22}	1.49 Msi (2.5%)	1.30 Msi (3.4%)
Poisson’s ratio, ν_{12}	0.294	0.316
Poisson’s ratio, ν_{13}	0.278	
Poisson’s ratio, ν_{23}	0.511	
Shear Modulus, G_{12}	720 ksi (2.6%)	759 ksi (3.1%) (*)
Shear Modulus, G_{13}	674 ksi (4.3%)	734 ksi (4.2%) (*)
Shear Modulus, G_{23}	437 ksi (2.2%)	437 ksi (2.2%) (*)
Shear secant-intercept modulus, K_{12}	31.3 ksi	48.8 ksi (*)
Shear secant-intercept modulus, K_{13}	30.9 ksi	48.7 ksi (*)
Shear exponent, n_{12}	0.213	0.266 (*)
Shear exponent, n_{13}	0.218	0.271 (*)
1-2 plane ILS strength, S_{12}	15 ksi	21.2 ksi (0.5%) (*, **)
1-3 plane ILS strength, S_{13}	12.9 ksi (2.1%)	16.6 ksi (4.3%) (*)
2-3 plane matrix tensile strength, S_{22}	18.6 ksi (6.1%)	18.6 ksi (6.1%)

* Standard properties from same SBS specimens, analyzed using closed-form solution

$$\tau_{max} = \frac{3P}{4A}$$

** Shear failure occurs at large strains larger than can be fitted with Ramberg-Osgood equation.

Results of the IM7/8552 test batch are summarized in Table 7, showing good agreement between SBS test method and ASTM standard for all linear properties. As a subset, the basic lamina material properties in the SBS test can be faithfully generated. This process is repeated for material X. Due to lack of reference, these properties are not shown here. Properties as defined in the SBS specimens were used as the starting point (initial material parameters) for the FEMU iteration scheme. Lacking more knowledge at that time, transverse isotropy was assumed, with, K_{23} and n_{23} set equal to K_{13} and n_{13} .

Figure 32 shows the experimental results for IM7/8552 as tested with SBS, 1.5in. SPT, and 2.5in. SPT. Excellent agreement verifies that both test methods are accurately measuring the material properties. As shear in the 1-2 and 1-3 plane are very similar, the assumption of transverse isotropy is reasonable to make. Note that the smallest SPT specimens achieve agree very well with the larger specimens but can achieve higher strain values. While the fixture parameters may be a cause in delaying failure in the SPT15 specimens, the smaller aspect ratio (span/thickness) is deemed to be more significant, as it is for the SBS specimens.

SPT specimens fail in a mixed-mode complex stress state, usually assisted by matrix tension. As such, no inference can be made on shear strength, but it is at least as large as the maximum stress as calculated in FEA. The ILS shear strength for IM7/8552 is estimated at 13.2ksi.

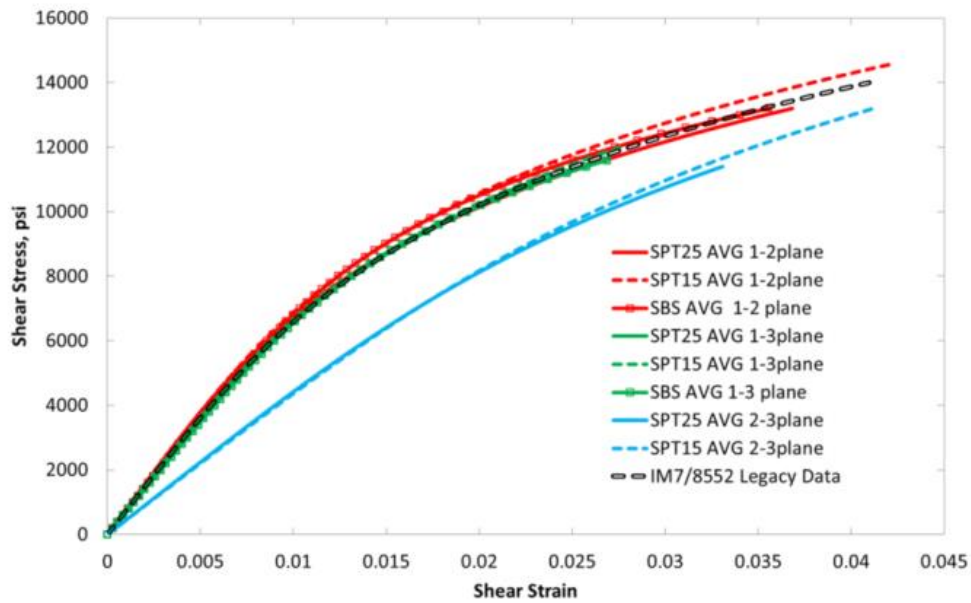


Figure 32. Average Shear Nonlinear Stress-Strain Behavior of IM7/8552 in All 3 Material Planes, Tested in Short Beam Shear (SBS), Small Plate Twist 1.5in. Square (SPT15) and 2.5in. Square (SPT2.5)

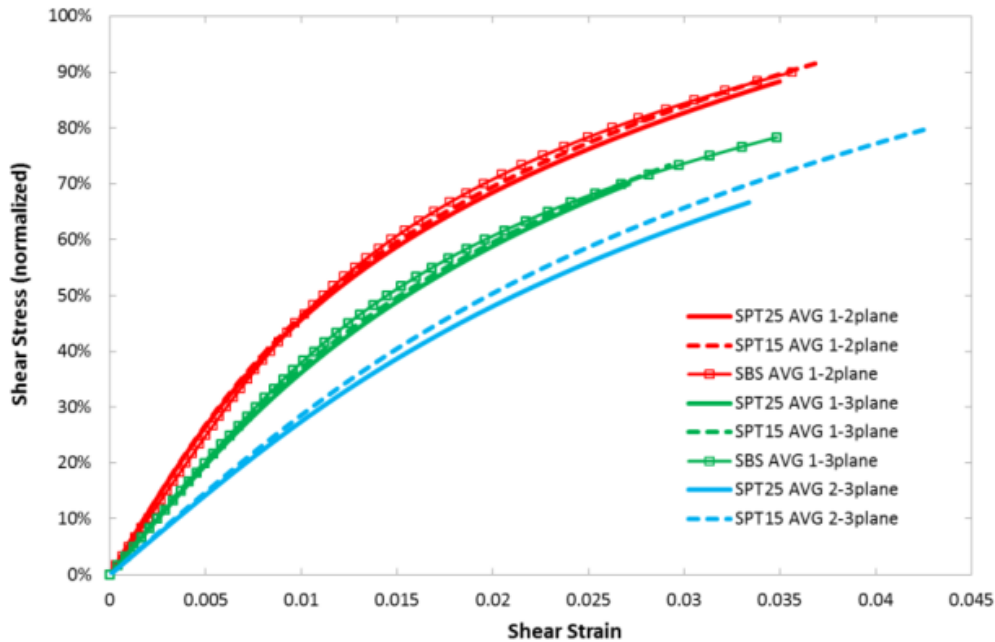


Figure 33. Average Shear Nonlinear Stress-Strain Behavior of Material X in All 3 Material Planes, Demonstrating Shear Anisotropy

The method is repeated for material X, for which the results are shown in Figure 33. The agreement between SBS and SPT is striking and show a distinct difference between material behavior in the 1-2 and 1-3 plane. Whereas IM7/8552 specimen shows a rather homogeneous microstructure throughout, material X has a clear topography difference in microstructure between 1-2 and 1-3 plane (Figure 34). As such, there is a strong anisotropic behavior, demonstrating the importance of accurate three-dimensional quantification of material parameters to be used in PDFA methods. In this case, such an assumption would have led to a 25% error in shear modulus and 20% error in ILS strength [7].

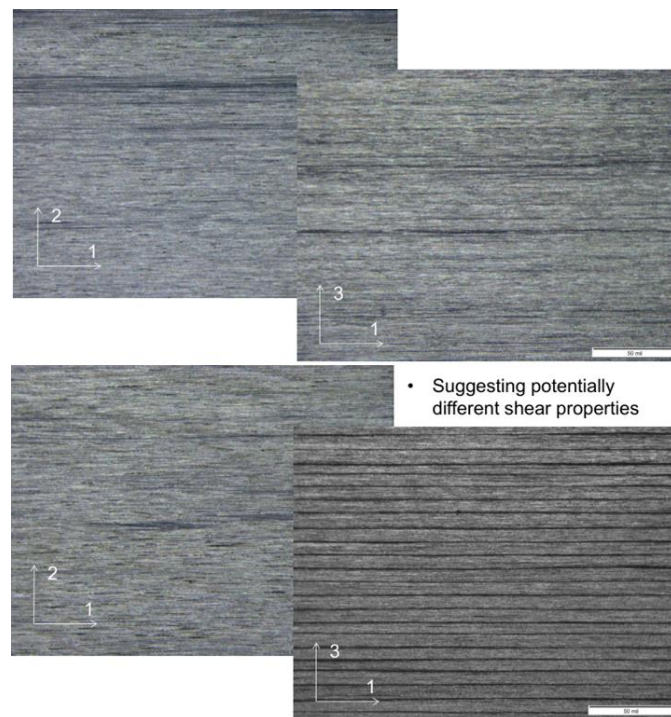


Figure 34. Top: Microscope Images of IM7/8552 SBS Specimens shows Similar Topology in 1-2 and 1-3 Principal Material Planes. Bottom: Different Topology suggests Different Shear Properties

3.2 Tensile Test of ± 45 Laminate

The most common method to characterize the shear modulus of a composite is to perform the ASTM D3518 ± 45 degree off-axis tensile test. This method is very compatible with other tensile tests, as it does not require dedicated fixtures. Ideally, this method for characterizing shear stress-strain behavior will agree with the SBS and SPT test. It is, however, not subject to pure shear [4]. D3518 specimens are subject to matrix and fiber tensile stress, and therefore exhibit the complex failure modes. The purpose of this study is to compare the shear curves between the tensile and SBS test to determine until what strain level they agree.

3.2.1 Virtual Test and Fiber Reorientation Studies

A virtual test using FEA was conducted to test whether the test procedure is accurate and captures all the true stresses and strain in the nonlinear regime. The FEM reproduced the ASTM D3518 in-plane shear stress-strain response. The 3D model consists of 1 or 2 elements per ply and has a mesh oriented with the fiber direction. Explicit PDFA was used to predict cracks and delaminations. Using the nonlinear material model, the FEA output strains are used as if they are the full-field strain measurements.

$$\tau_{12} = \frac{P}{2A} \quad (3-1)$$

$$\gamma_{12} = \varepsilon_{xx} - \varepsilon_{yy} \quad (3-2)$$

As shown in Figure 35, the virtual test was able to capture the input properties of the FEA model. This was done both with input properties of IM7/8552 and for material X. However, a slight deviation starts occurring at 3% shear strain. According to literature, cross-sectional area reduction is not captured in the ASTM standard equations, and fiber reorientation is not

simulated in the FEA model. The fiber reorientation is due to a geometry change: shear strain changes the angle of a volume element, and thus the fiber moves as well, as shown in Figure 36.

The effect of area reduction can be found using:

$$\tau_{12} = \frac{P}{2A(1 + \epsilon_{yy})} \tag{3-3}$$

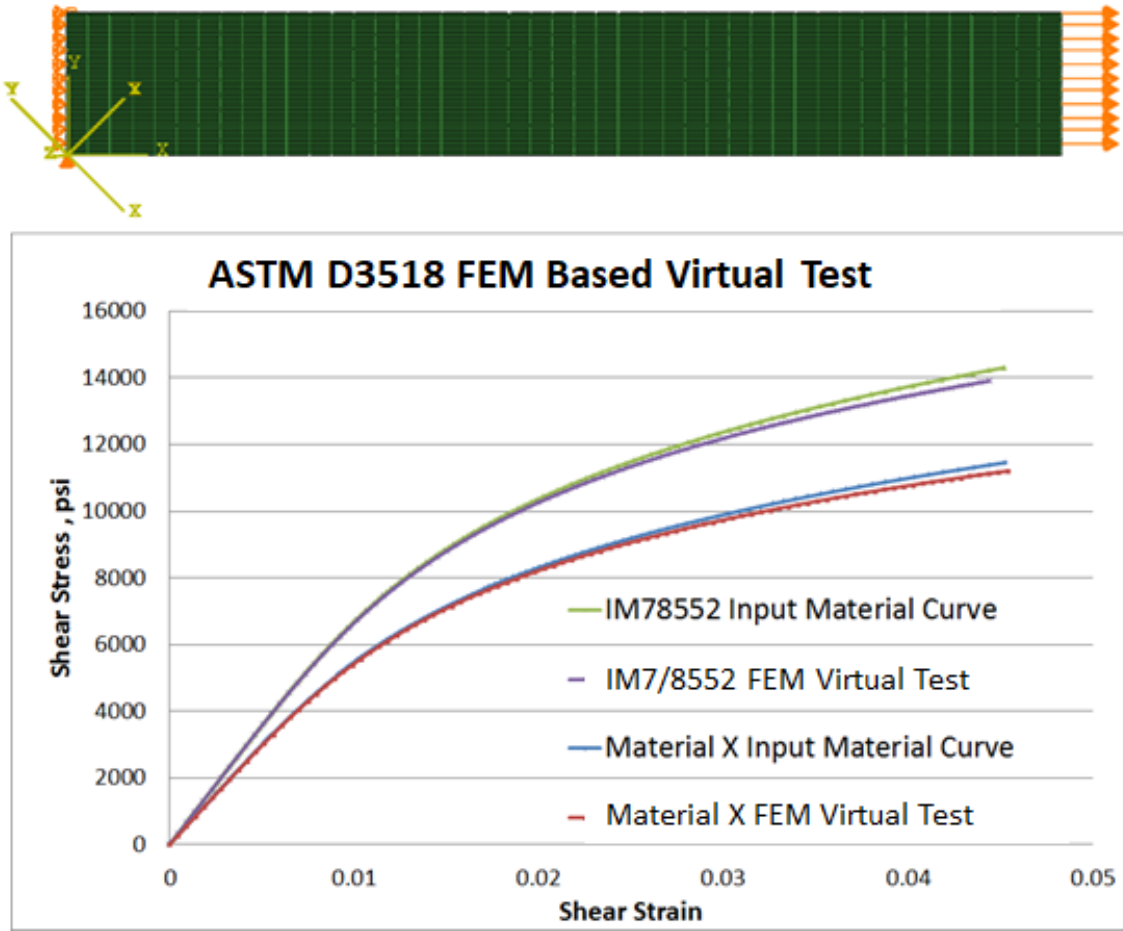


Figure 35. Virtual Test: FEA Model and Calculated Stress-Strain Curves Match Input for both Material X and IM7/8552

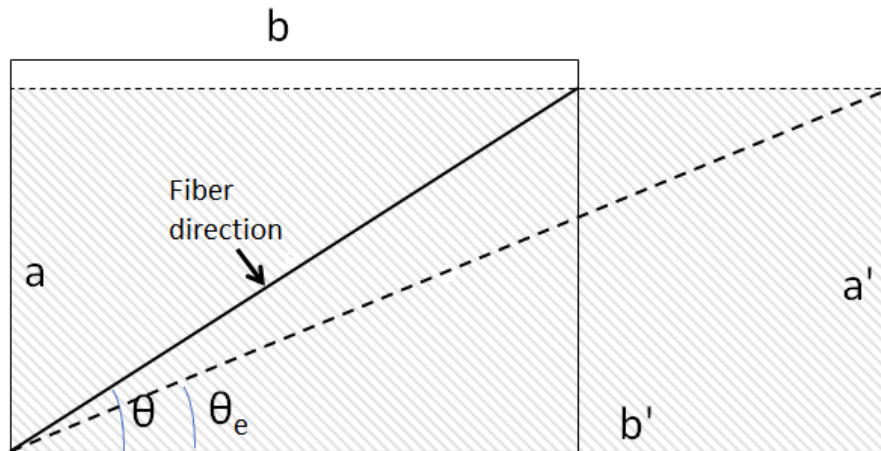


Figure 36. Fiber Reorientation in Off-Axis Tensile Test

Fiber reorientation is a function of the changing geometry. By trigonometry analysis, the new angle is defined as:

$$\tan(\theta_e) = \frac{a'}{b'} = \frac{a}{b} \frac{1 + \varepsilon_{yy}}{1 + \varepsilon_{xx}} = \tan(\theta) \frac{1 + \varepsilon_{yy}}{1 + \varepsilon_{xx}} \quad (3-4)$$

Therefore, principal stress and strains are in the wrong material axes. First, strain must be rotated. Stresses cannot be rotated, as the material behavior is nonlinear. The solution for a tensile test with fiber reorientation is found incrementally using small steps. In Matlab, the following scheme is applied using classical lamination theory (CLT). Calculate:

1. ABD matrices and Q_{ply} at current stress level;
2. Increment in global strains $\Delta\varepsilon_{x,y}$;
3. Fiber reorientation angle θ_e ;
4. Angle Increment $\Delta\theta = \theta_e - \theta$;
5. Total principal strains $\varepsilon_{1,2}$ by rotation about angle $\Delta\theta$: $\varepsilon_{1,2}'$;
6. Increment in principle strains $\Delta\varepsilon_{1,2}$;

7. Increment in principle stresses $\Delta\sigma_{1,2} = Q_{ply} \Delta\varepsilon_{1,2}$;
8. Total principle stresses $\sigma_{1,2}' = \sigma_{1,2} + \Delta\sigma_{1,2}$;
9. Total global stresses $\sigma_{x,y}$, updating $Q_{i,j}$ for nonlinear behavior

The 1,2 and x,y subscripts represent the material principal and global directions, respectively. The effect of these two phenomena are summarized in Figure 37. The cross-sectional area reduction and fiber reorientation becomes significant after 5% shear strain. This agreement fits well with established ASTM standard guidelines [4].

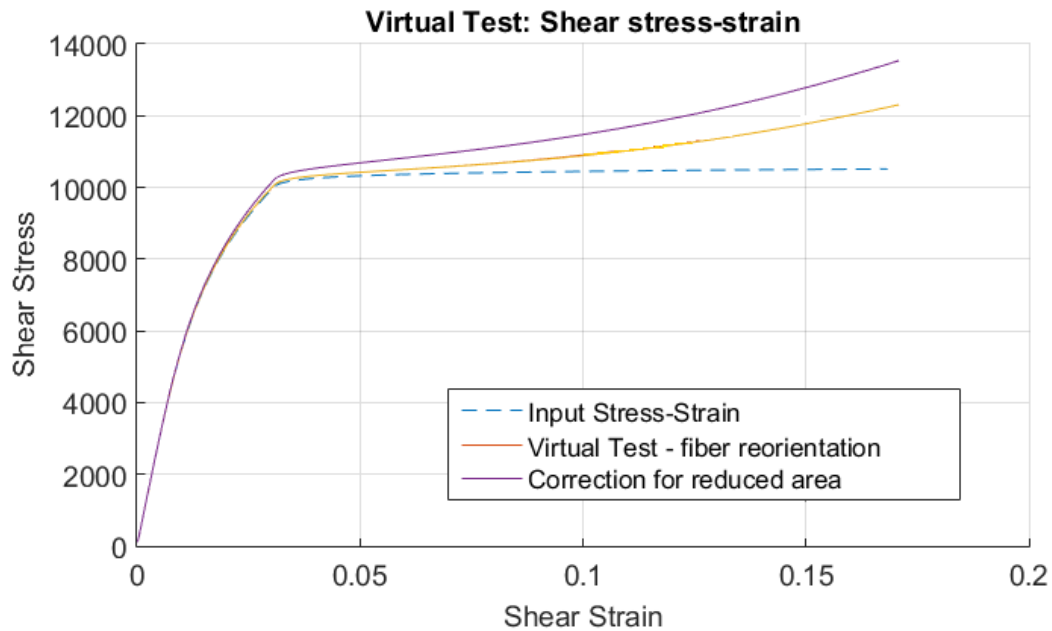


Figure 37. Virtual Test: Influence of Fiber Reorientation, Nonlinear Axial/Transverse Modulus, and Correction for Reduced Cross-Sectional Area

3.2.2 Test Method and Results

ASTM D3518 tensile tests were performed on 0.06in. thick 8-ply straight $[\pm 45]$ and dog-bone $[+45_2 / -45_2]_S$ specimens for IM7/8552 and only straight specimens for material X. The

straight specimens are according to ASTM spec, but the dog-bone specimens were used to ensure failure occurs at the gauge section, with the opportunity to track micro-cracks and other damage using CT imaging. Specimens are shown in Figure 38. The black-and white speckle patterns was used for the full-field strain measurement by DIC. The strain field was assumed homogenous, such that the average shear strain is of the whole part of the gauge section caught by the cameras and plotted against average stress. The specimens were tested in the Instron hydraulic test frame at 0.05in./min, with the first specimen tested with two DIC systems; one on each side. The DIC systems showed near-perfect agreement on the level of shear strain, verifying the alignment of the machine. The first specimen for each material is shown in Figure 39.



Figure 38. ASTM D3518 Specimens made of IM7/8552:
8-ply straight $[\pm 45]_2$ s (top) and Dog-Bone $[+45_2 / -45_2]_s$ (bottom) Specimens

The pilot specimens demonstrate that the straight specimens can reach very large levels of shear strain. This is also inevitable accompanied with some degree of fiber reorientation. This is visible on the un-painted back side, of the material X specimen, photographed during the test. At shear strain of 5%, the angle between the plies had reduced from 90 degrees to 87.5 degrees.

A linear trend is shown, where at a shear strain of 10%, the angle between plies is only 84 degrees still. The straight specimens lasted up to a very large strain, but the dog-bone specimen failed before reaching 4%.

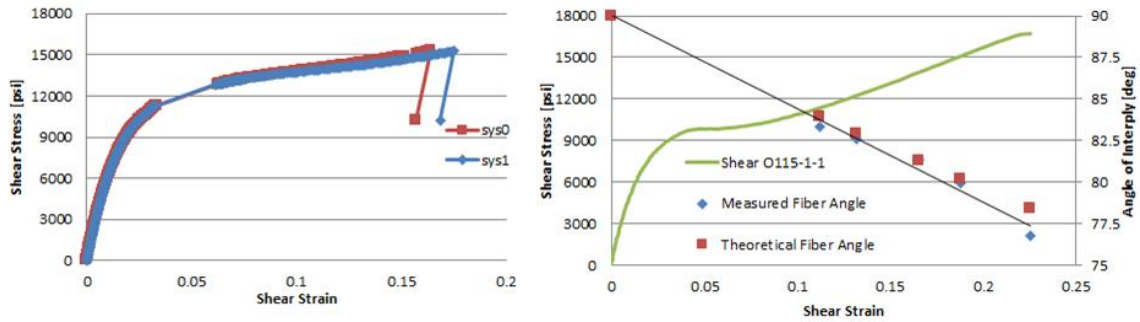


Figure 39. Analysis of Pilot Specimens for IM7/8552 and Material X Straight ASTM D3518 Specimens, Including Fiber Reorientation Results.

With the pilot study complete, the remainder of the specimens were tested using one DIC system. Due to the likelihood of matrix cracks forming, the test plan was set to load different specimens up to 6000 μ strain, 1% shear strain, and 3% shear strain, and to perform CT reconstructions for each specimen. The test results are summarized in Table 8, Table 9, Figure 40, and Figure 41. Table 8 also shows at what strain level specimens were tested to before the test was stopped and at what load the CT scan was performed. The average G_{12} value was defined by a linear regression in the ASTM D3518 test between 1000-3000 μ strain and matches well to the SBS-measured value, but the nonlinear properties do not match. The discrepancy starts at 4000 μ strain, at the start of nonlinear behavior. This phenomenon is consistent between the two material planes. At about 3% shear strain, the ASTM D3518 test result is about 12-15% lower than the SBS result.

Table 8. Test Results for ASTM D3518 Specimens

	Specimen	T_{avg} [in]	W_{avg} [in]	P_{max} [lbf]	G [psi]	γ_{max} [-]	P_{scan} [lbf]
IM7/8552 Dog-Bone	PB-1	0.060	0.60	825	6.49E+05	0.0388	Broken
	PB-2	0.059	0.60	282	7.06E+05	0.0058	0, 200
	PB-3	0.058	0.60	420	6.58E+05	0.0099	0, 300
	PB-4	0.059	0.60	778	7.18E+05	0.0316	Broken
	PB-5	0.059	0.60	770	6.71E+05	0.0324	0, 500
IM7/8552 Straight	P8-T45-1	0.060	1.00	1816	7.11E+05	0.1752	0
	P8-T45-2	0.059	1.00	488	7.23E+05	0.0060	360
	P8-T45-3	0.060	1.00	731	7.21E+05	0.0100	500
	P8-T45-4	0.059	1.00	1347	6.86E+05	0.0375	650
Material X Straight	O115-1-1	0.060	0.99	2002	6.21E+05	0.2300	-
	O115-1-2	0.060	1.00	416	6.06E+05	0.0060	0
	O115-1-3	0.060	0.99	594	6.31E+05	0.0097	0
	O115-1-4	0.060	0.99	1060	6.14E+05	0.0307	0
	O115-1-5	0.060	0.99	1170	6.07E+05	0.0563	-

Table 9. Comparison Linear Shear Modulus G₁₂ between SBS and T45

	IM78552	Material X
SBS	7.20E5	6.03E5
45° Tensile	6.94E5	6.16E5
% difference	-3.6%	+2.2%

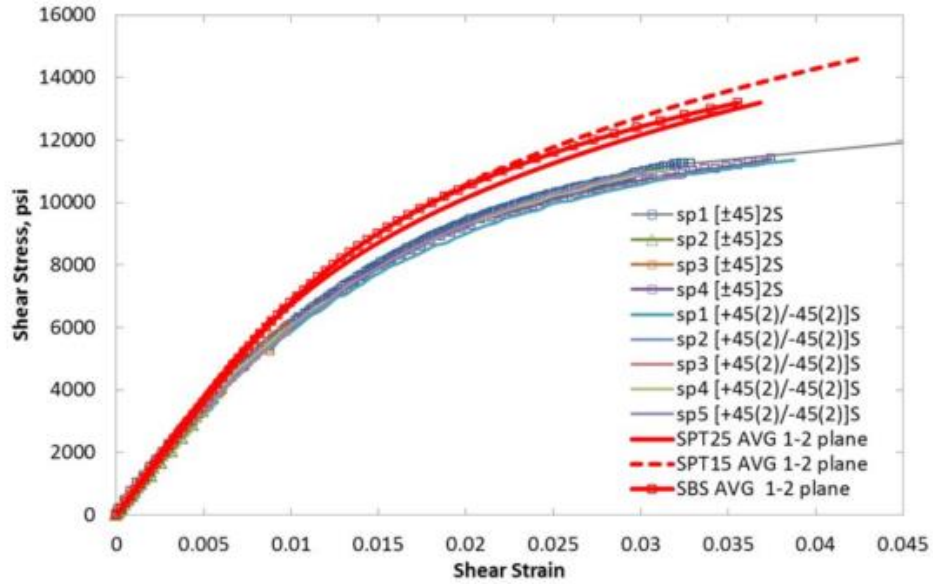


Figure 40. Comparison Nonlinear Shear IM7/8552; ASTM D3518 Straight and Dog-bone Tensile Test, Short Beam Shear, and SPT 1-2 Plane

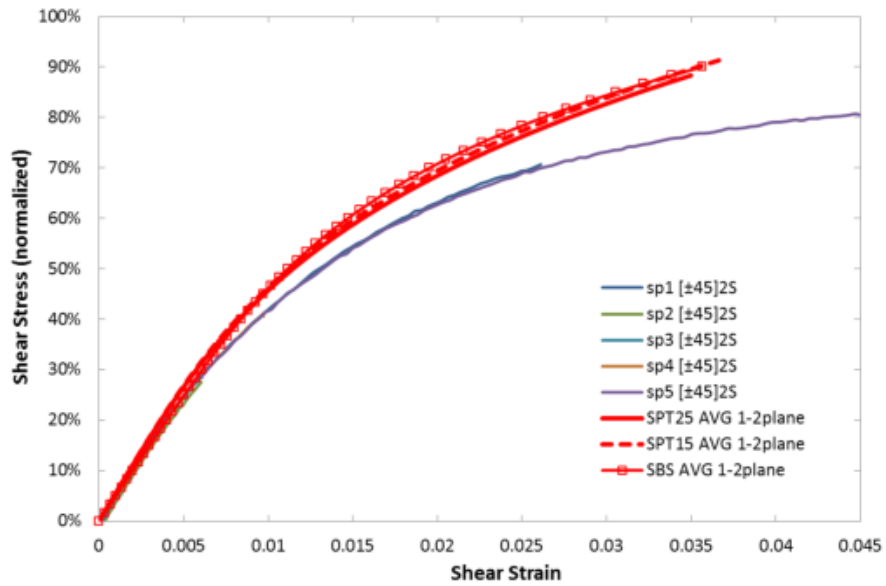


Figure 41. Comparison Nonlinear Shear Material X; ASTM D3518 Straight Tensile Test, Short Beam Shear, and SPT 1-2 Plane

3.2.3 CT Study of D3518 Specimens

The shear strength measured in ASTM D3518 tests are usually underestimated due to the effect of normal stresses in the matrix [18], leading to mixed-mode matrix cracking. This might cause the considerable reduction of the 0.2 offset strength. Besides that, there is also a noticeable effect of stacking sequence and number of plies [4]. Consider that the D3518 specimens were only 0.06in. long, they may have cured differently than the SBS and SPT specimens, all cut from a .25in. thick panel.

A scan of the straight IM7/8552 specimen P8T45-1, tested up to 17%, provides insight on the failure modes that one may expect to see in the reconstruction. This specimen was scanned using a heavy element dye penetrant that shows up clearly in the reconstruction. Figure 42 shows a wild array of matrix cracks in the 45deg direction, along with delaminations and crack amalgamation between plies.

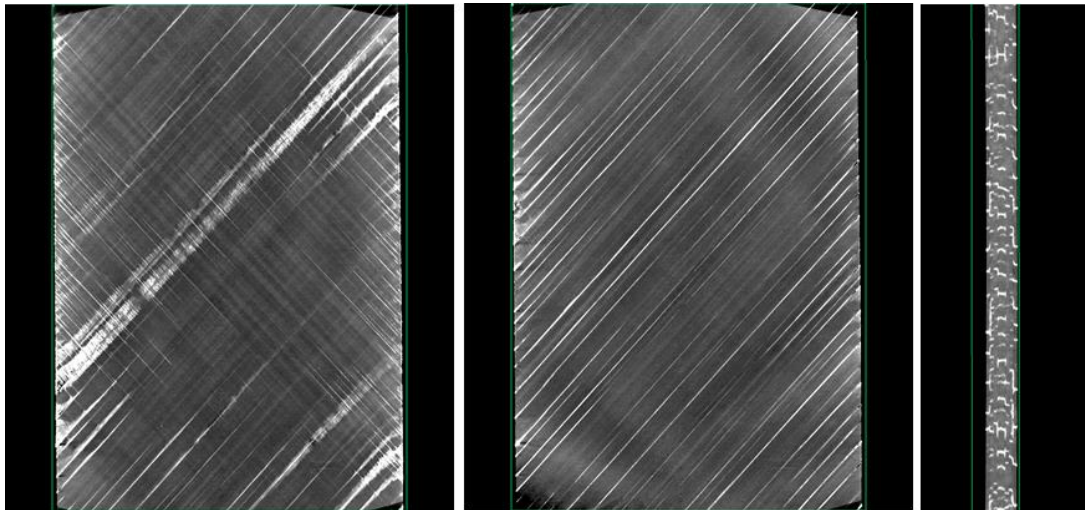


Figure 42. CT Reconstruction of IM7/8552 D3518 Specimen at 17% Shear Strain

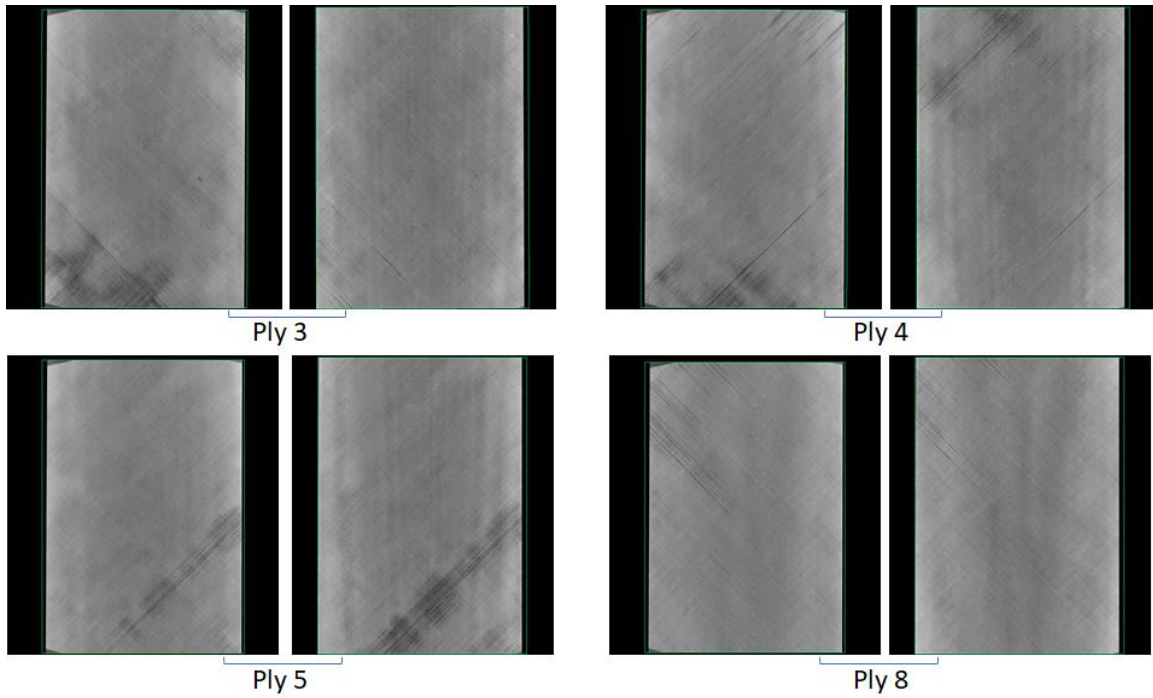


Figure 43. Pretest/Posttest Scan Material X O115-1-4 (3.1% Shear Strain)

CT reconstruction images from the D3518 specimens pre-test and post-test scans with heavy element dye penetrants and some of them under load as well. A typical reconstruction is shown in Figure 43. All specimens have plenty of defects, including voids, matrix cracks, and inclusions (including hairs). The dye penetrant has not penetrated any cracks, which indicates edge cracks are small or nonexistent. Furthermore, damage pattern and size are consistent between pre-test and post-test scans. While these flaws may influence the shear modulus, damage development is not yet active at 3% strains. This result is supported by reference [96].

3.2.4 Evaluation of In Situ Lamina Shear Properties in SPT

One big difference between ASTM D3518 and the SBS/SPT is the stacking sequence. The 90deg interply angle represents a laminate, rather than a unidirectional stacking sequence. Therefore, one hypothesis is that some in-situ material properties are different from those in unidirectional configuration. Neighboring plies may cause constraints on allowable deformation or introduce stresses within the material during curing. As such, a SPT specimen was created of IM7/8552 with a stacking sequence of $[0_2/90_2]_{3S}$ at UTA facilities. The specimens are 1 x 1 x 0.177in and one is shown in Figure 44. The specimen is speckled and only used for 1-2 shear stress-strain characterization. The other two surfaces have alternate plies between 1-3 and 2-3, so it is not logical to perform measurements on these planes as well.

Analysis of the SPT 1in. specimens was performed by the FEMU algorithm, only optimizing the 1-2 plane. Legacy data for IM7/8552 was used to fill in the other properties, including shear in the 1-3 and 2-3 planes. The results of this iterative analysis are plotted alongside the previous obtained result in Figure 44. Regardless of the stacking sequence, the SPT 1in. specimens agree well with previous SPT tests, confirming the robustness of this test. The evidence does not support the hypothesis that in situ material properties in the laminate are different from those measured in unidirectional coupons.

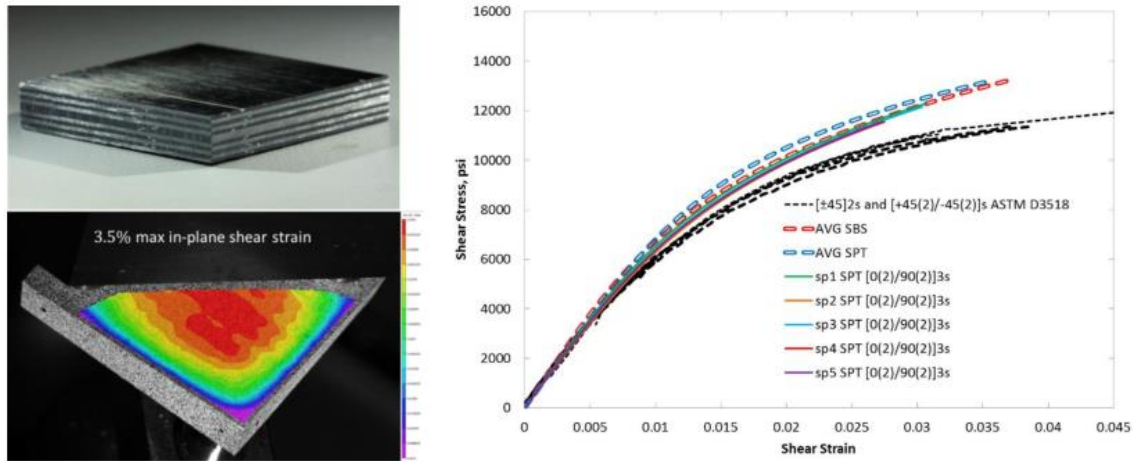


Figure 44. An IM7/8552 SPT Specimen with $[0_2/90_2]_{3S}$ Stacking Sequence (top), and Typical Surface Shear Strain Measurements in 1-2 Plane.

3.2.5 Compression D695 Tests and Sensitivity to Stacking Sequence

As noted in references [16,20], the shear nonlinear behavior is affected by normal stresses in the matrix. As such, the hypothesis is formed that the normal stress state of the epoxy influences the shear stress-strain behavior. To test this hypothesis, one D3518 specimen was machined into 6 smaller specimens (.458 x .060 x 3in.), to be used as D695 compression specimens. The D695 fixture is modified to have a clear plastic front plate, such that it is possible to perform DIC strain field measurements. The front and back parts of this fixture prevent buckling as the specimen is compressed. This is plotted in Figure 45, where it is shown that the D695 specimen test results agree nearly exactly (on average) with the D3518 specimens, even though the loading is reversed. As the specimen is not constrained laterally, the specimen buckles sideways at higher loads and deviates from the D3518 specimen test results.

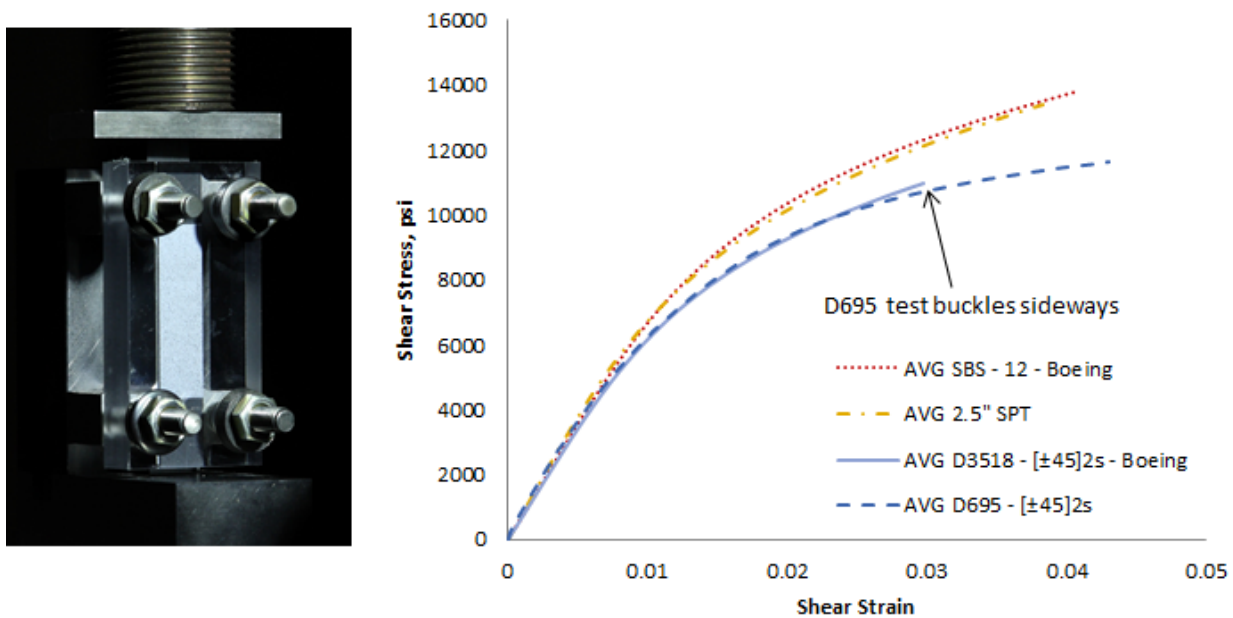


Figure 45. Comparison of IM7/8552 D695 $[\pm 45]_{2s}$ Compression Shear Stress-Strain Test Results to SBS, SPT Results. Left: Picture of D695 Fixture with Different Specimen

The test results for the D695 test compared to D3518 do not give conclusive evidence that the normal stress state in the material is responsible for the difference in test methods. In this final effort, a new batch of IM7/8552 SBS $[0]_{24}$ specimens with D3518 specimens with $[45_2/-45_2]_{3s}$ specimens are made. These specimens are made with material sourced at AMSL, and all have a thickness of 24 plies. As such, there are more commonalities between these specimens than before. The tests (5 specimens each), have been tested using the identical test method as described in previous sections and the results are shown in Figure 46. For the SBS coupons, the agreement between test results of different material supply is very good, but the D3518 test results are different. The thicker laminate has an increased 0.2% offset strength and does agree better with SBS test results. The difference at 3% shear strain is 8% between test methods, so the difference is still significant.

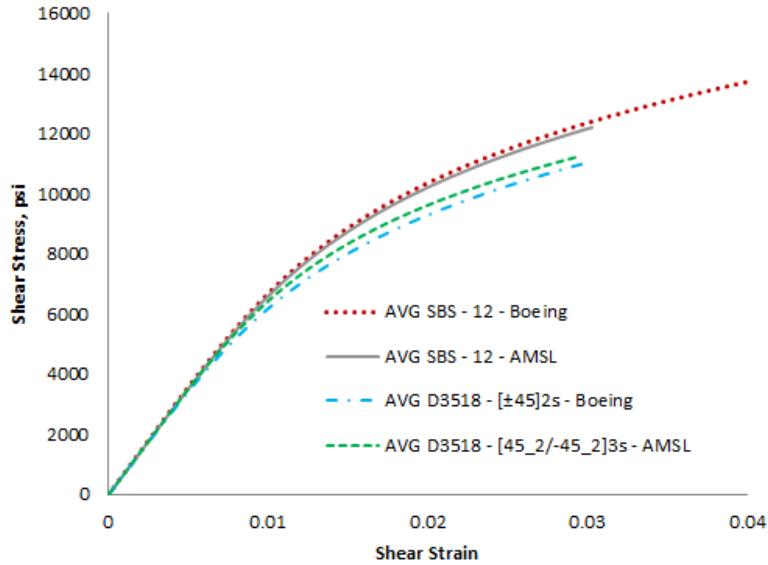


Figure 46. Comparison of IM7/8552 D3518 [45₂/-45₂]_{3S} Shear Stress-Strain Test Results to SBS, Sourced from AMSL Materials

3.2.6 Reversible Strains

Nonlinear shear stress-strain behavior may occur to micro-structural damage such as shear bands [18][21]. Polymer behavior is unlike metals, such that the 0.2% offset strength may not represent permanent damage. Instead, polymer deformation is a nonlinear process in which the molecule chains align and stretch before damage starts. Moreover, it is difficult to judge what part of the stress-strain curve is considered a damaged state, which may be significant for useful life predictions of composites. The D3518 tensile test is an effective method to study constitutive behavior, degradation, and stiffness reduction under monotonic and repeated loadings. While full characterization of damage processes in nonlinear shear is out of scope for this thesis, the following test data shows viability of this test method to indicate a threshold for the elastic regime of the material.

One tensile D3518 $[\pm 45]_{2s}$ IM7/8552 tensile specimen is loaded under repeated and increasing peak strains according to the scheme shown in Figure 47. Strains are measured using the DIC system. Each step increases peak strains (displacement control), before quickly unloading and relaxing at zero load to remove transient strains. As such, the residual strains represent a permanent damaged state of the material. The nonlinear behavior also means that load increments are quite small to reach ever higher strains. In the figure, one can quickly tell that significant residual and transient strains start forming as soon as 1% of peak strain is reached. Holding time was set in increasing intervals to ensure transient strains had been mostly removed, which increased as peak strains increased as well.

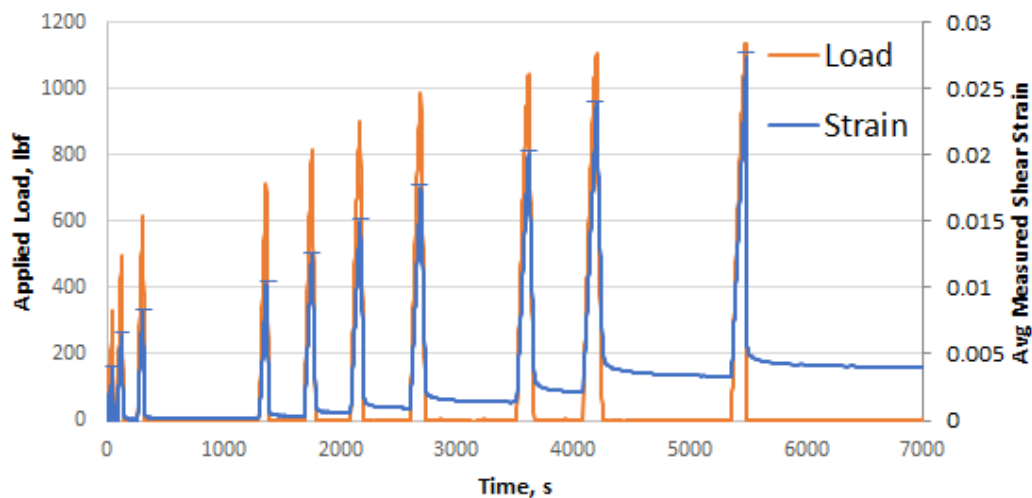


Figure 47. Repeated Loading History of an IM7/8552 D3518 Specimen

Using DIC full-field strain measurements, the repeated loading stress-strain curves are plotted in Figure 48. As a reference, the data from a monotonously quasi-static loaded D3518 specimen is plotted along these repeated loading curves. As the peak strain increases, the loading

curves shift to the right, and the total stress-strain curve becomes significantly lower than as measured in the quasi-static test. Note that all transient strains are removed at the start of each loading curve, such that only permanent strains remain. Figure 48 (right) shows all stress-strain curves shifted to start at the origin. As such, they do follow the reference line very well in the nonlinear regime.

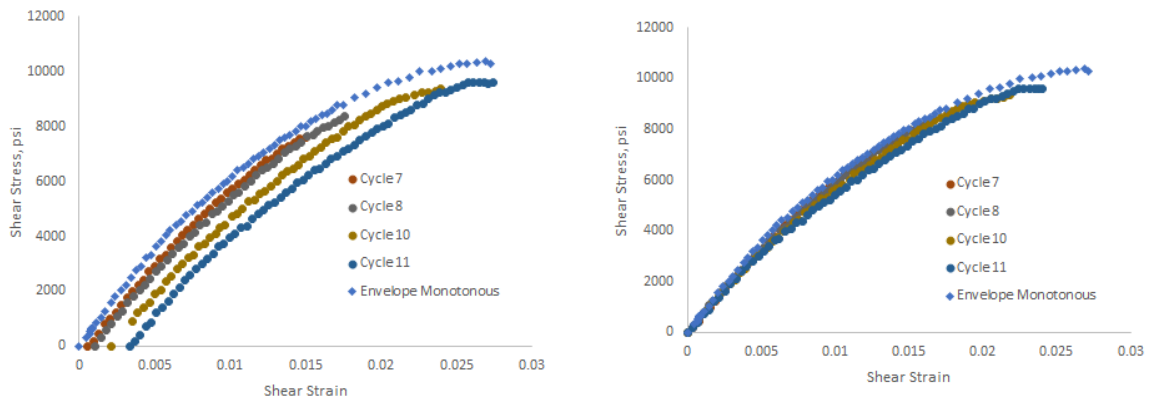


Figure 48. Repeated Loading Stress-Strain Curves for IM7/8552 D3518 Specimen.
 Left: Permanent Strains are Visible. Right: Permanent Strains Removed

A visible reduction in shear modulus is apparent from the shear curves in Figure 48, which is related to the permanent strain state within the epoxy. The shear modulus as a percentage of the elastic (original) shear modulus is plotted in Figure 49. The relaxed strains are added to this chart to establish trends. As peak strains increase during repeated loadings, both transient and permanent strains increase, while the linear modulus decreases. Permanent and transient strains become significant starting at 1%, while the shear modulus drops quickly at 1.5%. At these levels of strain, no damage was identified in the CT reconstructions. Further

studies should be conducted to establish what phenomena are responsible for the loss in modulus and the significance of the level of peak strain.

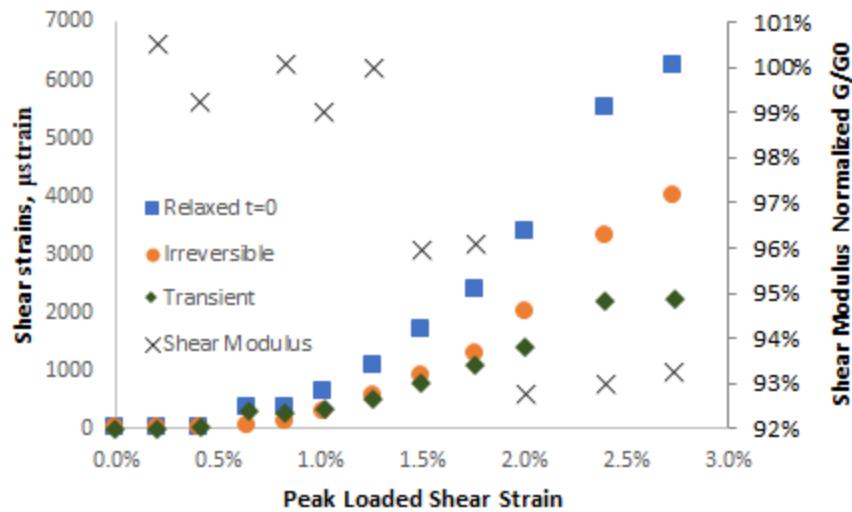


Figure 49. Reduction in Shear Modulus and Increasing Permanent and Transient Strains during Repeated Loading of IM7/8552 D3518 Specimen

This chapter presented an analysis of the applicability of the SBS, SPT, and $\pm 45^\circ$ tensile test method to characterize shear nonlinear properties. The SBS specimens analyzed with optimization methods agree very well with the SPT specimens, which were analyzed with FEMU analysis. As a result, this methodology can be used to verify simplifying material model assumptions, such as transverse isotropy in shear. The ASTM D3518 specimens agree in the linear regime but deviate at $4000 \mu\text{strain}$. The tensile test results are dependent on stacking sequence, overall specimen thickness, and suffer from complex mixed-mode micro-scale damage development, which develops well before damage can be picked up by CT reconstructions.

CHAPTER 4

ADVANCED APPLICATIONS IN THE SBS METHOD

The Short Beam Shear test method is highly versatile method and can be used to measure the 3D constitutive material properties, as well as nonlinear shear behavior in the 1-2 and 1-3 plane and a range of failure modes. Across the wide range of available shear characterization methods, obtaining a pure shear failure mode is still challenging. In the SBS test, many specimens can fail in shear if the proper fixture and specimen configuration is used [35]. Still, certain materials can withstand large amount of shear deformation and will still fail in mixed-mode failure at the contacts. Legacy FEMU and first-order solutions do not provide the flexibility or accuracy to characterize high-strain material behavior.

4.1 Characterizing High Strain Response

4.1.1 Wrapping phenomena during the test

The IM7/8552 and material X SBS specimens tested in the 1-2 plane (see section 3.1.2) were subjected to very high levels of shear strain. Moving beyond 5% shear strain, these specimens experience very large deformation and “wrapping” behavior of the specimen around the loading nose. What is visible in Figure 50 is full-scale yielding along the cross-section of the SBS, with quickly rising shear strains as the contact area of the loading nose increases until it makes full contact. Effectively, the distance between contact surfaces decreases and shear strains are concentrated in a smaller span section. While specimens in this study failed in pure shear,

specimens that exhibit this behavior often fail in mixed-mode fiber compression – interlaminar shear stresses.

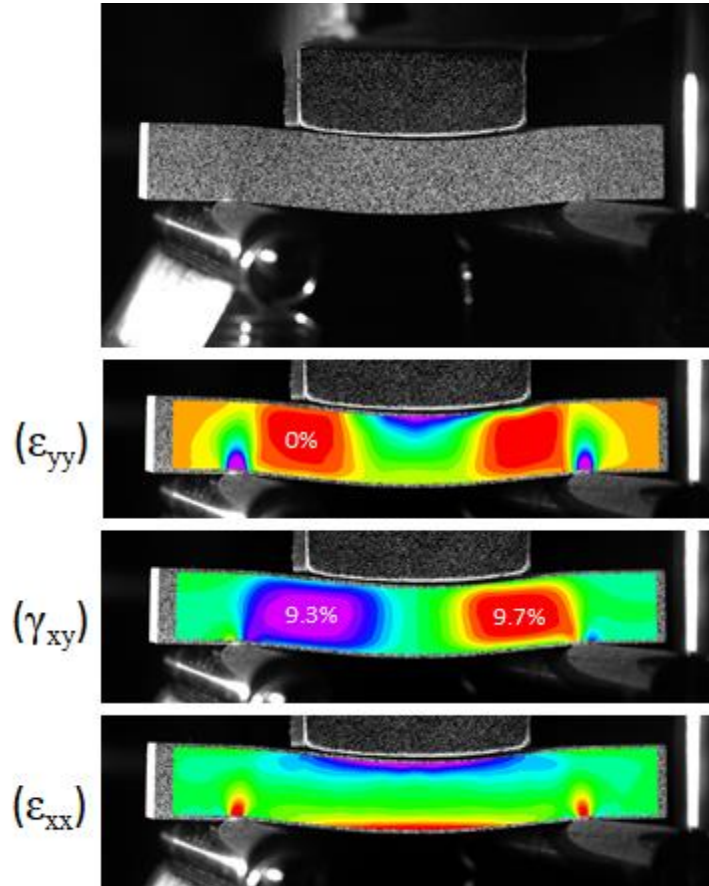


Figure 50. IM7/8552 SBS specimen .25x.25x1.2in. Span Tested in 1-2 Plane. Wrapping of the Specimen Around Loading Nose (top). Strain Fields as Measured using DIC are shown.

Considering this behavior rapidly decreases the effective span to thickness aspect ratio, the first order estimate becomes more inaccurate. This is due to warping of the specimen cross-section and transverse stresses that are spread along a larger section of the span. Furthermore, the Ramberg-Osgood equation is not able to curve-fit beyond 4-5% of shear strain, as the change in slope occurs too quickly. These are the reasons that images of specimens at loads exceeding the wrapping threshold have been discarded as unreliable data. The DIC system is an objective and

independent analysis method able to measure large strains and deformations and should provide accurate strain measurements even after wrapping.

4.1.2 Results from Optimization Model

The optimization model as defined in chapter 2 provided the flexibility to analyze SBS from start to failure. Instead of performing the cross-sectional analysis at the customary 50%, the chosen cross-section $\frac{x}{L_L} = 40\%$ is not subject to the transverse stresses, even after wrapping around the loading nose. This maintains the assumptions that the optimization model is based upon. Focusing on the shear properties, the first order estimate of $\frac{3P}{4A}$ is evaluated first, followed by the optimization analysis. No changes to the optimization model were made. These two solutions are plotted in Figure 51. As expected, the closed-form solution greatly overestimates the maximum shear stress. At a shear strain of 8%, this error is about 33%.

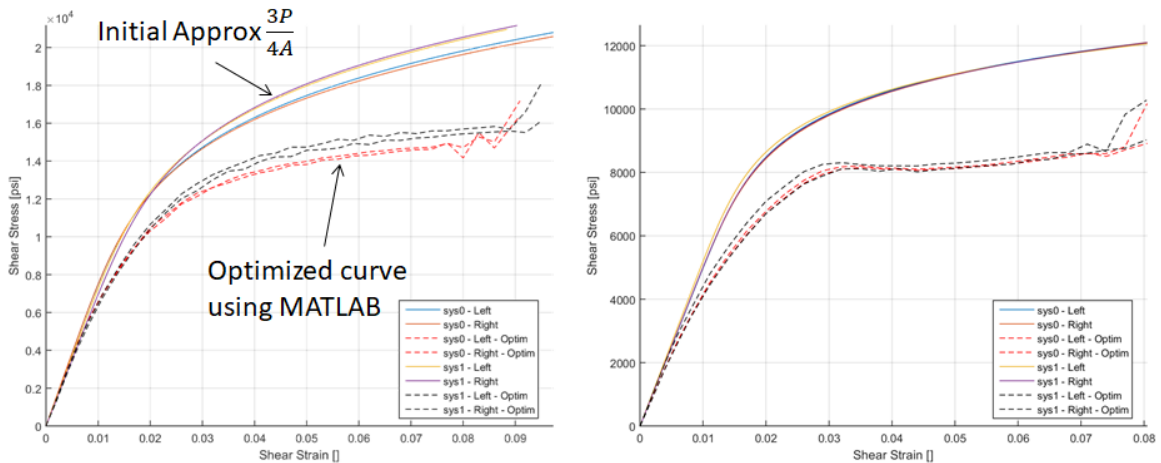


Figure 51. Characterization of Nonlinear Shear Stress-Strain Behavior in 1-2 Plane for IM7/8552 (Left) and Material X (Right)

The nonlinear stress-strain curves exhibit small oscillations at the highest strain values, because the amount of data at the highest strain value is the lowest. Therefore, it is the most susceptible to noise. The curves exhibit a large change in slope after 3% shear strain. The material X specimens show the most dramatic change in shear modulus, as the slope goes horizontal. As such, the load increases, but the maximum stress does not. Such a counter-intuitive result draws parallels with perfectly plastic behavior of metals.

The underlying assumptions for the optimization model may lose validity when analyzing specimens with large deformations. Notably, the specimen is assumed to have small deflections such that the fibers and the specimen itself do not rotate. As such, part of the shear force may be aligned in the direction of the beam and transformed into an axial force. Furthermore, the operator must be mindful of the strain formulation, which is defined as engineering strain. Future studies investigating this large-strain response with greater confidence and accuracy should address the implication and aspects of these assumptions.

4.1.3 Simulation in FEA environment

To gain more insight into the wrapping behavior of the SBS specimens at higher loads, an FEA study was performed. As the material X specimen had such extensive wrapping behavior starting at 3%, with such a dramatic change in slope, it was chosen to simulate in the FEA environment. Note that the FEA model used is the same as was developed and described in section 2.3.1. The diameter of the loading nose is 4in. as tested, which is a significant parameter for the model.

The material model chosen is a simplification of the stress-strain curve as plotted in Figure 51. The Ramberg-Osgood equation sets the behavior up to a strain level of 0.03%

(8000psi). The UMAT includes an if-statement. If the strain exceeds 0.03%, the slope must be zero. A material model with a large discontinuity in derivative will lead to unstable behavior, frequently causes FEA models not to finish. Therefore, the flat line is replaced with an exponential function, which has an initial slope to provide continuity but quickly goes to zero. This is plotted in Figure 52.

Simulation of the SBS specimen is performed in one quasi-static step, but results can be distinguished into two separate phases. Up to 3% shear strain, the SBS specimen behaves predictably, with simulated strain fields matching with that of the measurement (Figure 53). As soon as 3% shear strain is reached, the contact surface area starts to increase rapidly with applied load. This behavior is only simulated by including the highly nonlinear large-strain behavior. Without, the virtual specimen would carry much larger loads without inducing the wrapping. As soon in Figure 54, the regions of maximum shear appear to cover a smaller part of the span. The material model is shown to be directly responsible for the wrapping.

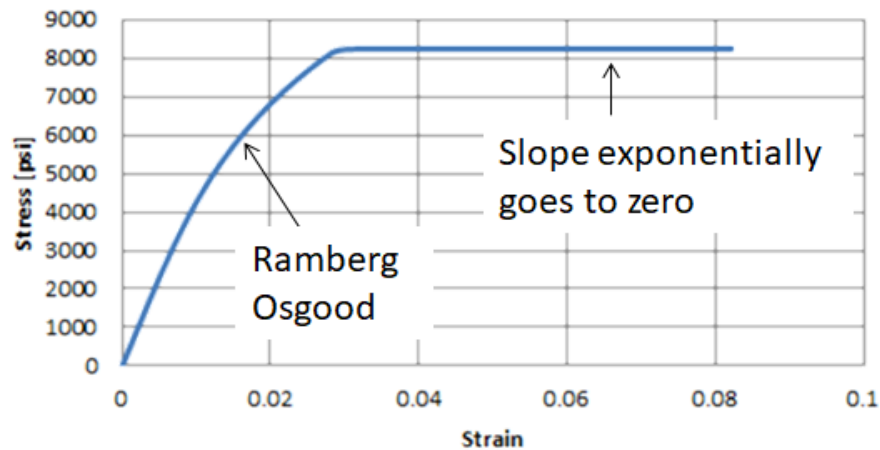


Figure 52. Highly Nonlinear Shear Model for UMAT to Simulate High-Strain Behavior

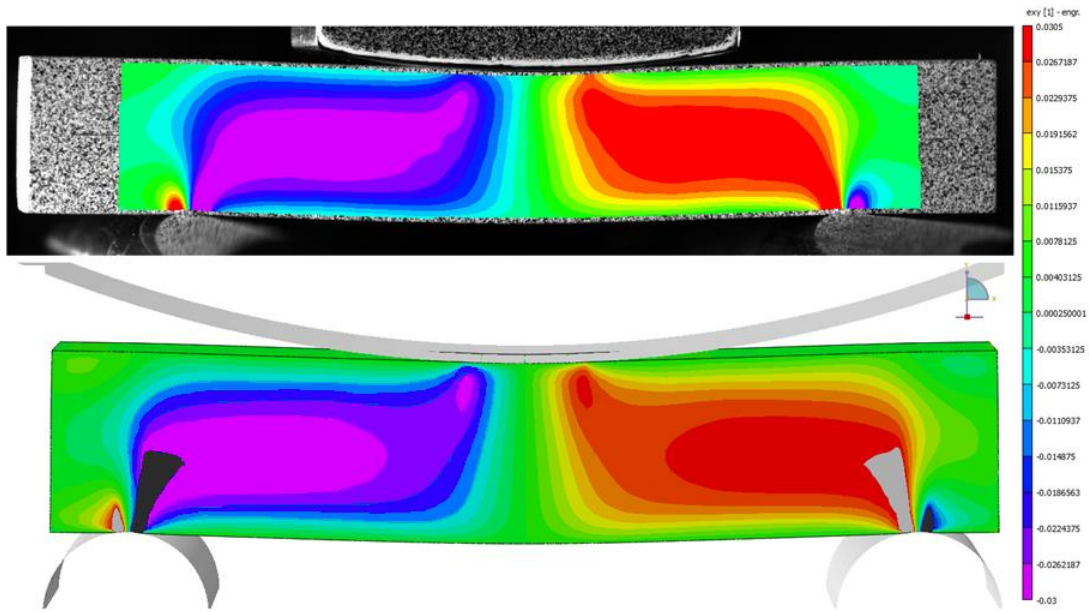


Figure 53. Material X SBS Specimen: Comparison of Measured and Simulated Strains. Specimens are .25 x .25 x 1.2in. Span under 900lbf Load. Color Legend is Matched

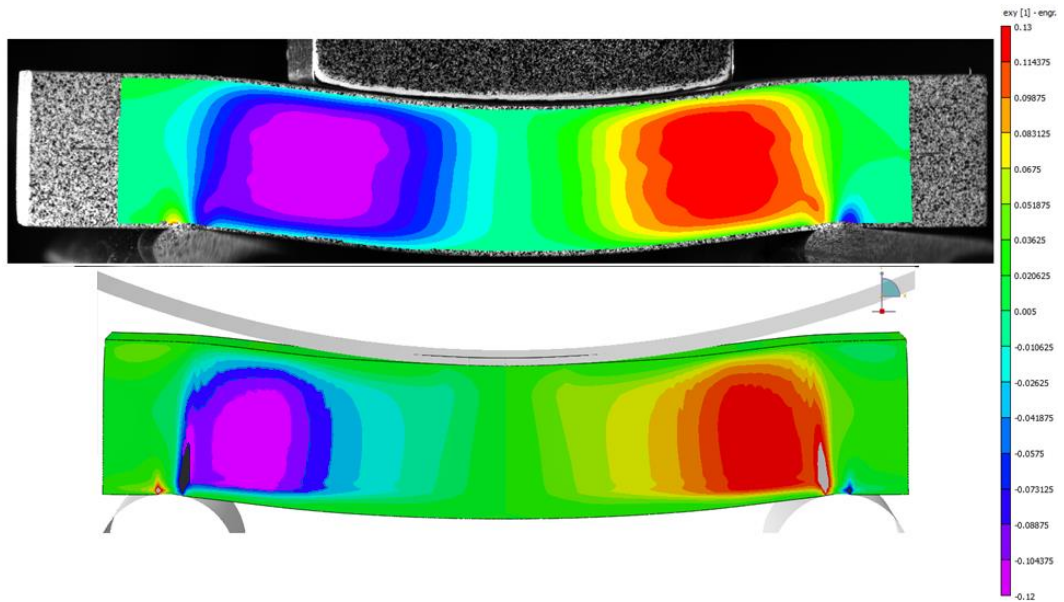


Figure 54. Material X SBS Specimen: Comparison of Measured and Simulated Strains. Specimens are .25 x .25 x 1.2in. Span under 1100lbf Load. Color Legend is Matched.

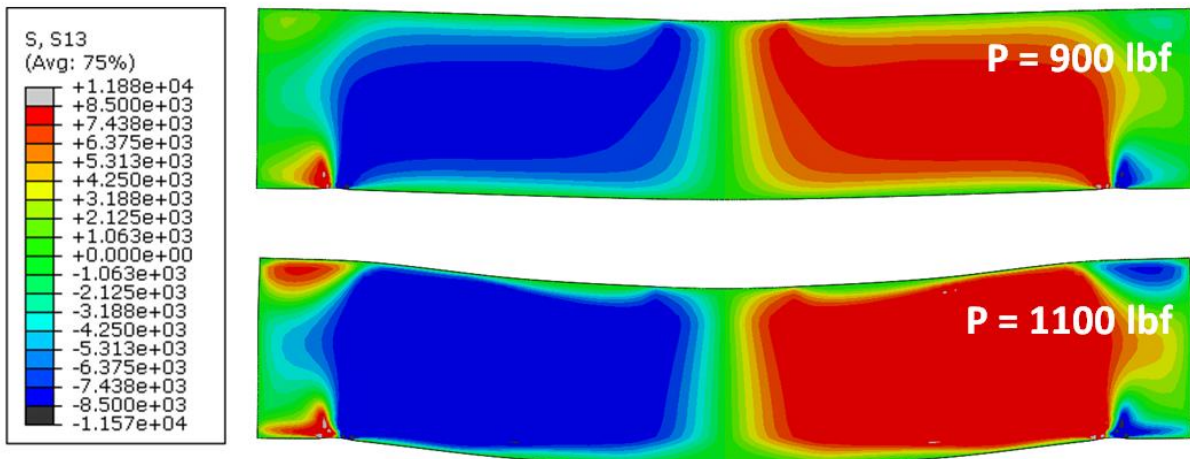


Figure 55. Material X SBS Specimen: Comparison of Simulated stresses under 900lbf and 1100lbf Load. Specimen demonstrated Large-scale Yielding throughout the Cross-section. Color Legend is Matched for both Plots

The reason that the specimen wraps around the loading nose is due to large-scale yielding through the cross-section. At approximately $P=900\text{lbf}$ applied load, the maximum stress of 8200psi is reached. This stress cannot increase, as it is not on the material stress-strain curve. Therefore, other parts of the cross-section must increase their stress to 8200psi to sustain the applied load, as can be seen in Figure 55. The load is increased, until the cross-section is unable to raise its stress along the cross-section anymore. As a result, shear strain increases rapidly, and conforms to the shape of the loading nose.

Wrapping behavior at the loading nose is not an undesirable result, as it is driven by material stress-strain behavior. However, some specimens tend to exhibit pure shear failure if tested with a small loading nose diameter, without the wrapping behavior. A small loading nose would distribute the load under a smaller area, and locally the shear stresses could exceed either the ILS strength or induce a mixed-mode shear and compression stress failure.

4.2 The Asymmetric Three-Point Bend Test

4.2.1 Reasoning and First-order Estimate

While the current SBS test has many different configurations (see Table 1) to test many different properties, the short beam and long beam specimens have distinct advantages and disadvantages which may require the use of both tests. The long beams have low shear stresses through the cross-section, such that the first-order equations are very accurate. Short beam specimens are necessary to characterize shear behavior but suffer from less reliable axial strain measurement data. It is very difficult to get high magnification/resolution in long beam specimens, due to the desire to have the longer specimen in the field of view. By using symmetric fixtures such that the left and right supports are placed equidistant from the loading nose, one limits themselves in possible outcomes. The fixture span and support placements are important considerations.

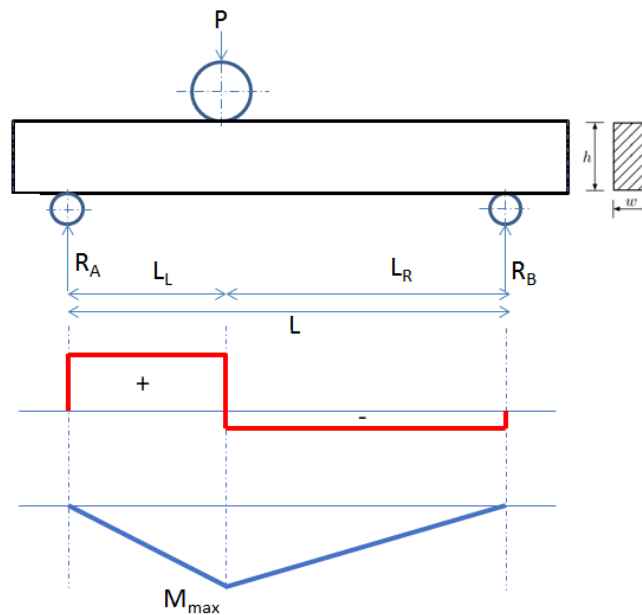


Figure 56. Static Analysis of the 3-Point Bend Test, with Asymmetric Span Setup

The asymmetric SBS test shown in Figure 56 is subject to different stresses in the left and right gauge sections. Most notable, the cross-section in the short side is subject to the larger shear force. While the bending moment is not significantly different between the two gauge sections, the long side benefits from the low shear stresses. Therefore, the theory is that the short side is more effective to measure shear nonlinear properties. The long side would be more suitable for measuring the axial properties. Applying equations 2-3 and 2-4 to the asymmetric SBS, the maximum shear force increases while the maximum bending moment decreases, which means SBS specimens are much more likely to fail in shear, rather than fail under mixed-mode stresses at the loading nose.

Consider a hypothetical SBS specimen with a span of 1.2in. loaded with the loading nose at 0.4in. from the left support. The shear force would be twice higher in the short side, compared to the long side. The effective aspect ratio (span/thickness), would be 3.2 on the left and 6.4 on the right. This would make the first-order estimate less accurate on the short side, and more accurate on the long side (evidence provided in Figure 15). Since the specimen is more likely to fail in pure shear, it is reasonable to increase the total span or decrease loading nose diameter to compensate for the small aspect ratio effect.

4.2.2 Experimental program and Test Results

All the predictions from the previous sections have been verified by an experimental study for IM7/8552 SBS specimens in the 1-2 and 1-3 plane. From a single IM7/8552 panel, two sets of .25 x .25 x 1.75in. specimens were machined to be tested in the 1-2 plane. The first set of five SBS were tested with symmetrical fixture and a span of 1.2in. The second set of these specimens were offset with the left support set at 1.0in. and the right at 0.6in..

From a second IM7/8552 panel to be tested in the 1-2 plane, two sets of specimens were machined of dimensions .175 x .175 x 1.75in. The first set of five specimens were tested in the symmetric fixture, and four specimens were machined dedicated for the offset SBS test. Three of these were tested with a span of 0.36in. and 0.60in. left and right respectively. The last specimen was tested at a more extreme offset, with support placements at 0.36in. and 1.00in..

All specimens had been tested with two DIC systems, one for the front and one for the back. Figure 57 shows the shear strain field for a IM7/8552 1-2 plane specimen with each of the two offsets. No complications associated with the offset were found during the test. The shear strains are larger on the short side, exceeding 5% shear strains. The specimens tested in the 1-2 plane exhibited larger strains and more wrapping behavior at the loading nose.

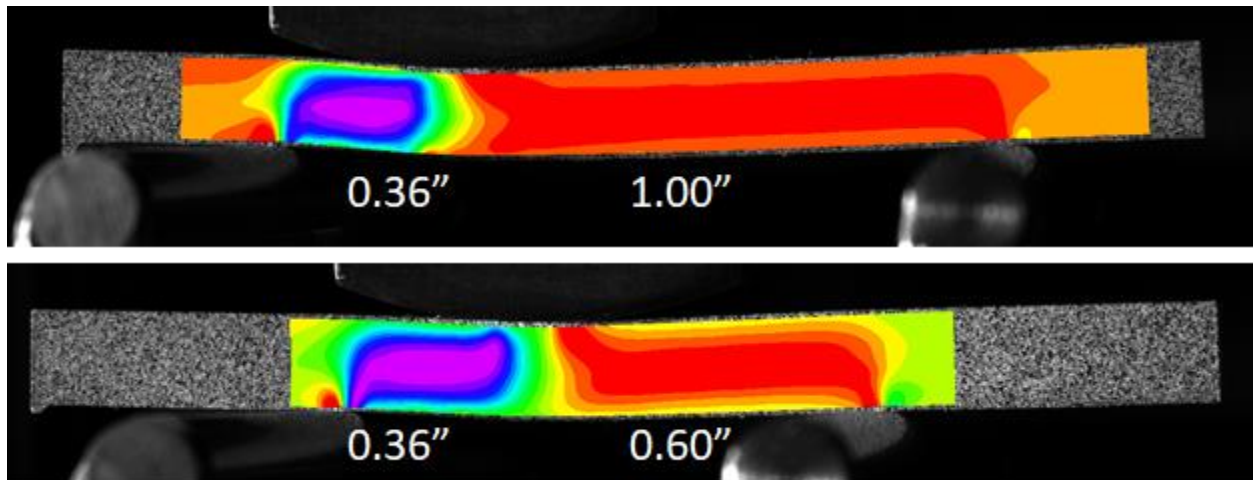


Figure 57. IM7/8552 Offset Asymmetric SBS Specimens Tested in 1-2 Plane.

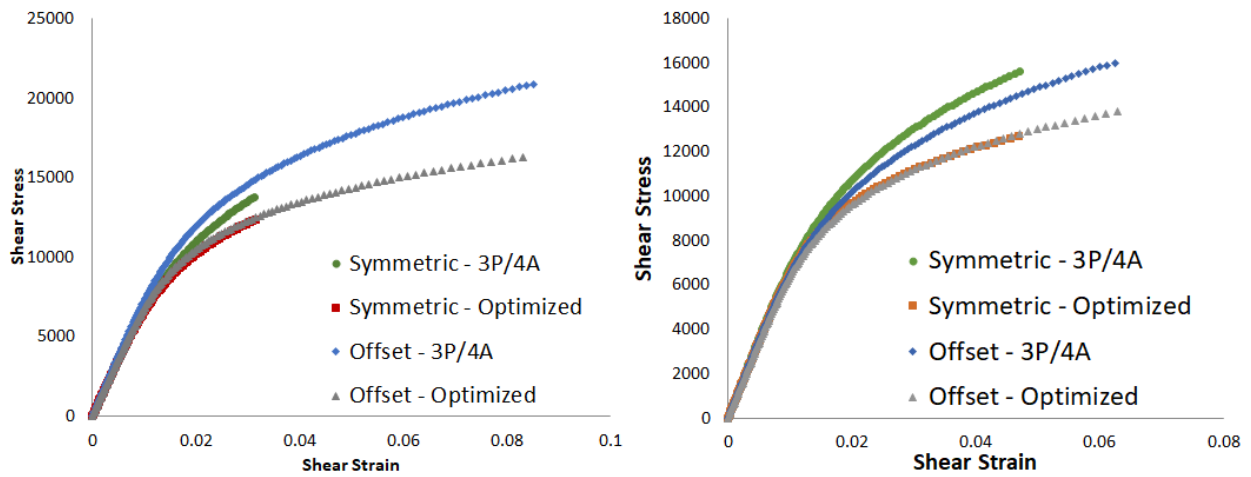


Figure 58. IM7/8552 SBS Test Results: Comparison Average Shear Stress-Strain Curves from Symmetric and Offset SBS Specimens. Left: 1-2 Plane. Right: 1-3 Plane

Table 10. IM7/8552 Specimens 1-3 Plane Test Results: Comparison Average Material Parameters from Symmetric and Offset SBS Specimens

	<u>First-Order Analysis</u>	
	Symmetric	Asymmetric
Span (L,R inches)	0.6, 0.6	1.0, 0.6
E_t [Msi]	22.3	22.0
E_c [Msi]	19.1	20.0
E_{AVG} [Msi]	20.7	21.0
ν_t	0.31	0.34
ν_c	0.38	0.42
S [ksi]	15.5	16.1
Failure Mode	Mixed	Shear
G [ksi]	731	708
K [ksi]	3.75	33.8
n	0.239	0.232
	<u>Optimization Analysis</u>	
G [ksi]	698E	681
K [ksi]	23.7	24.7
n	0.176	0.184
S [ksi]	12.8	13.2
E_{xx} [Msi]	20.7	20.7

The test results are summarized in Figure 58 and in Table 10. The agreement between the shear stress-strain curves of symmetric and asymmetric specimens is striking, because the first-order estimate is very different. Note how the closed-form solution for shear stress in the offset specimens is worse than in the symmetric specimen, but that difference is removed during optimization analysis. Symmetric SBS specimens in the 1-2 plane failed early due to mixed-mode failure, because the span of 1.2in. was set too high for the specimen thickness of 1.75in. The asymmetric specimens were able to achieve pure shear failure with a shear stress-strain that agrees well to that as plotted in Figure 51.

The choice of span for the symmetric SBS specimens in the 1-3 plane was more appropriate, but the specimens were failing under mixed-mode failure at the loading nose. While the offset specimens have a slightly longer span, the increase in shear force at the short end was sufficient to result into characterizing the full shear nonlinear behavior until pure shear failure. Tabular results for the specimens in the 1-3 planes show that both experimental setups are effective at measuring all material properties. For this study, the axial properties were evaluated only on the long end, which did marginally improve on the numerical results for the tensile and compressive moduli in the fiber direction.

The optimum offset parameters are not fully investigated during this thesis, as they may depend on the material system to be tested. The IM7/8552 SBS specimens in the 1-2 plane were tested in two configurations, which represent a 3:5 and a 9:25 span ratio. The comparison is shown in Table 11. The longer and more offset ratio of 9:25 provided a marginally improved set of axial moduli but did not provide any more benefit for characterizing shear nonlinear properties. As the specimen gets longer, the operator must reduce DIC resolution to maintain the

specimen in the field of view. The law of diminishing results applies; results do not necessarily improve with increasing offset ratios.

The short beam shear specimen offers great flexibility in the design of experiments, which allows the user to influence what failure modes and mechanical properties are measured. By choosing an offset span ratio for the SBS test, the chance of pure shear failure is increased. This experimental design program adds complexity and closed-form solutions become less applicable. Shear stress-strain results after optimization are consistent results between a selection of configurations. This alleviates concerns of repeatability and gives confidence in the reliability of this experimental setup. The experimentalist may choose the span supports and offset of the loading nose to best measure the intended material response. By using optimization methods described in this thesis, large shear strain response can be characterized, even if it does not follow a particular material model.

Table 11. IM7/8552 Offset SBS Specimens 1-2 Plane Test Results:
Comparison Offset Ratio on Characterized Material Properties

L:R Span (in)	Pmax (lbf)	Strength (psi)	G (psi)	K (psi)	n (-)	E_{T,avg} (psi)	E_{c, avg} (psi)	E_{xx} (psi)
0.36 : 0.60 3 : 5	718	20959	7.58E+05	3.98E+04	0.222	2.54E+07	2.05E+07	2.29E+07
0.36 : 1.00 9 : 25	548	19263	7.67E+05	3.77E+04	0.214	2.32E+07	2.07E+07	2.20E+07

CHAPTER 5

CHARACTERIZING TRACTION SEPARATION BEHAVIOR

This work addresses a lack of understanding and measurement data on cohesive traction-separation laws for delamination fracture. This is a fundamental challenge of progressive damage and failure analysis of composite structures, which is sensitive to the input parameters of the cohesive zone model. Typical updating methods use CZM laws based on mathematical assumptions and strive to optimize its parameters to minimize the error to a certain objective function. The work presented in this chapter aims to develop methods to measure the traction-separation law directly, improving the confidence in cohesive laws.

5.1 Cohesive Force Model

The growth of a crack constitutes a change in the energy in a system. From this idea, the fracture characteristics of an adhesive crack were derived from total specimen energy balance. The energy balance is defined by Sun and Wang [97] as

$$\Delta W = \Delta U_e + \Delta W_p + \Delta W_s \quad (5-1)$$

where W and U represent work and energy respectively. ΔU_e is the elastic strain energy, ΔW_p is the plastic energy and ΔW_s is the energy required to grow the crack surface. Fracture energy is dissipated from total work and depends on the change in fracture area.

$$R = \frac{\Delta W}{dA} - \frac{\Delta U_e}{dA} = \frac{dW_p}{dA} + \frac{dW_s}{dA} \quad (5-2)$$

$$R = G_p + G \quad (5-3)$$

The dissipated energy R represents energy loss due to plasticity and creation of new crack surface dA . For brittle materials, plastic energy dissipation is assumed to be negligible [83,85], such that fracture energy is equal to the energy release rate G . By adopting this assumption, one can use the J-integral or the VCCT method to gain a useful estimate of the energy release rate. For the DCB test, the contour integral is calculated about the cohesive zone. A closed-form solution exists for this application [81] as

$$J = \frac{12(Pa_0)^2}{E_d h_d^3} + (w'_1 - w'_2) \quad (5-4)$$

where P is the applied load; a_0 is the crack length; E_d and h_d are the lengthwise modulus and thickness of the adherend skins respectively; and w' are the rotations of the skins at the crack tip. This equation assumes negligible contribution due to shear force, so the crack length must be much longer than the specimen thickness. No closed-form solution exists to calculate the J-integral for the Thick Adherend test. The VCCT method was selected to calculate the strain energy release rate for the TA test. G is defined as the work necessary to close a crack with an element length. The equation for fracture energy dissipation has been rewritten to be implementable in the FEM environment with finite element sizes:

$$G_{II} = \frac{1}{2} \frac{F_s \delta u_x}{B \Delta a} \quad (5-5)$$

in which F and δu are the surface shear reaction force and relative separation of the relevant nodes as shown in Figure 59. The relative separation is the difference in displacements of the nodal points. The size of the element in which the crack growth is given by B and Δa , the

element width and length. The underlying assumption is that the crack is self-similar and will continue parallel to its current path, so the elements near the crack have the same size.

The following definitions are used to relate the separation of the top and bottom crack surfaces to the restraining stress acting on them within the damage zone. A linear elastic fracture mechanics approach is not useable, as it leads to infinite stresses at the crack tip. Instead, the J-integral is used. By definition, the J-integral is path independent, as long as the contour Γ does not go through the cohesive zone. It is conveniently placed along the upper and bottom traction surfaces. In this derivation, crack tip separation is only 1D.

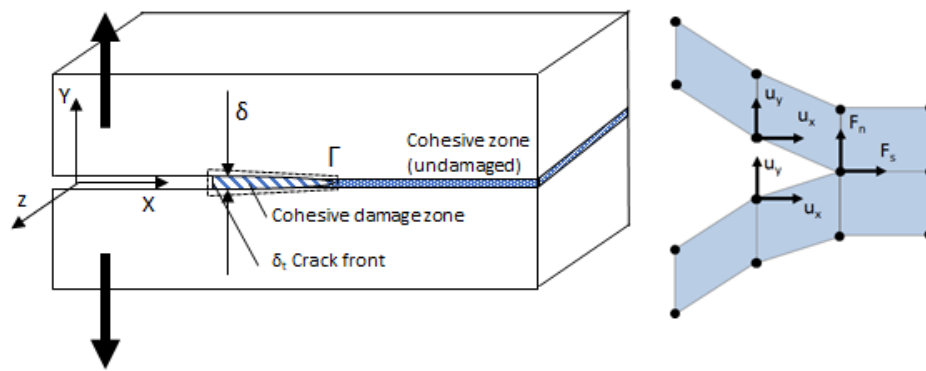


Figure 59. Relevant Parameters for the VCCT Method

$$J = - \int_{\Gamma} T_i \frac{\partial u_i}{\partial x_1} ds = - \int_{c.z.} \sigma \frac{\partial \delta}{\partial x_1} dx_1 = - \int_{c.z.} \frac{\partial \delta}{\partial x_1} \left[\int_0^{\delta} \sigma(\delta) d\delta \right] dx_1 \quad (5-6)$$

$$G = J = \int_0^{\delta_t} \sigma(\delta) d\delta \quad (5-7)$$

Here, c.z. is the abbreviation for cohesive zone, and δ can be defined as either the normal separation at the crack front (Mode I), or the slip separation (Mode II). $\sigma(\delta)$ is the surface traction as a function of the crack separation. As the J-integral is path independent, it can also be set very

far away from the crack zone. At a far distance, the cohesive forces are insignificant, so the J integral represents the energy decrease of the noncohesive solution. In other words, the area under the traction-separation cohesive law gives the work done to grow a crack and is thus defined as being equal to G . Finally, the traction-separation relationship can then be deduced to

$$\sigma(\delta) = \frac{\partial J}{\partial \delta} \quad (5-8)$$

5.2 Experimental Procedure

5.2.1 Specimen Manufacturing and Precracking

Thick Adherend and DCB specimens were manufactured from IM7/8552 carbon fiber reinforced prepreg tape co-cured with Hysol EA 9690-006 film adhesive and cut from the same panel. The specimen dimensions are shown in Figure 60. Fiber bridging was a concern, so the chosen lay-up $[0_{16}/3_2/\text{FilmAdhesive}/-3_2/0_{16}]_T$ has 3degree offset fibers at the interface. This orientation prevents fiber bridging, while still being close to unidirectional. The film adhesive was co-cured with the skins, which created an irregular bondline thickness, averaging .0068in. The DCB specimens had aluminum blocks with center drilled holes bonded for load application. A starting notch was machined between the blocks using a grinder. The TA specimens were made by milling out grooves on both ends of the gauge section. CT reconstructions of the TA specimens were used to identify manufacturing issues. Machining of the grooves caused damage at the side surface of the TA specimens as shown in Figure 61. The damage may have acted as a starting point for failure, so it was removed by grinding, reducing the width of these specimens.

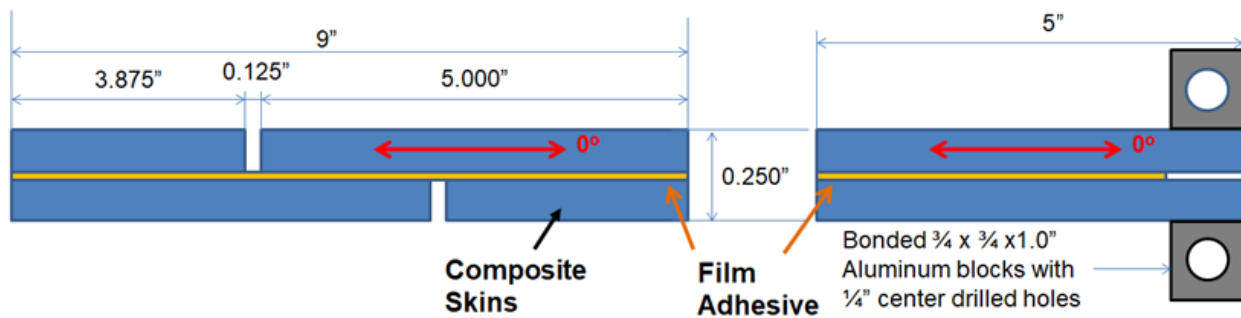


Figure 60. Thick Adherend (Left) and Double Cantilever Beam (Right) specimens as cut from a single co-cured panel.

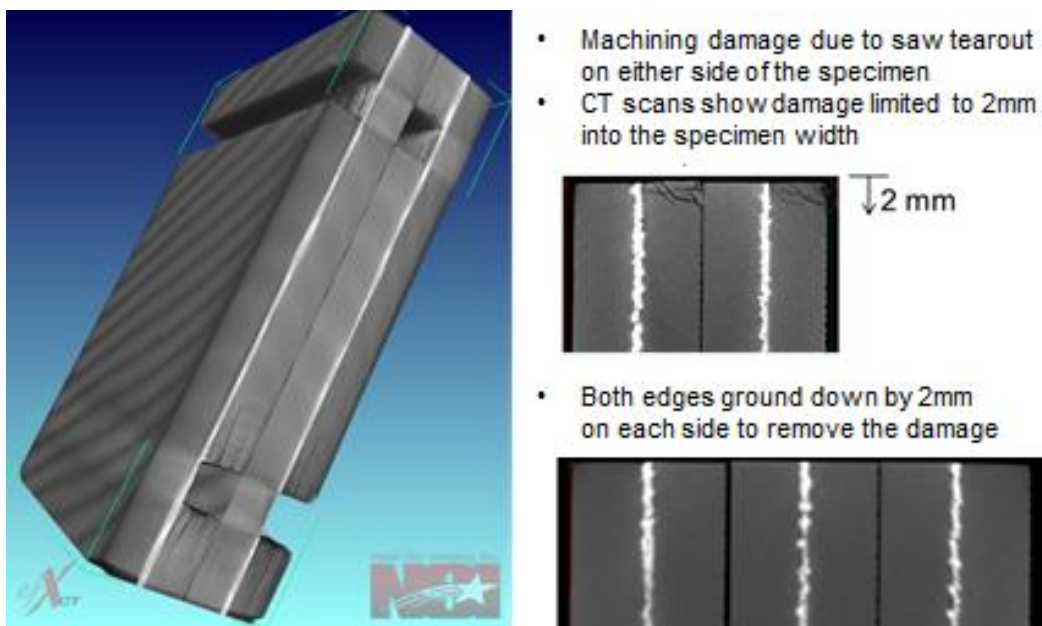


Figure 61. Thick Adherend Specimen Fabrication Issues

Specimens were manufactured without initial defect. Preliminary testing of DCB and TA specimens has proven that crack growth is stable in the DCB and TA tests (see Figure 62). Under fatigue loads, TA specimens exhibit low average stresses, and a small process zone. Crack growth is very sudden in static TA tensile test without a pre-crack, as the internal energy becomes very high. The net stress and process zone are large, and failure occurs seconds after

initiation. Every specimen was pre-cracked in fatigue ($f = 10\text{Hz}$, $R=0.1$). Each DCB specimen was pre-cracked until a_0 was about 10mm long and the TA specimens until a_0 on either side was 3mm long. CT pretest reconstructions were used to identify the crack tip locations through the width.

Fatigue failure progression →

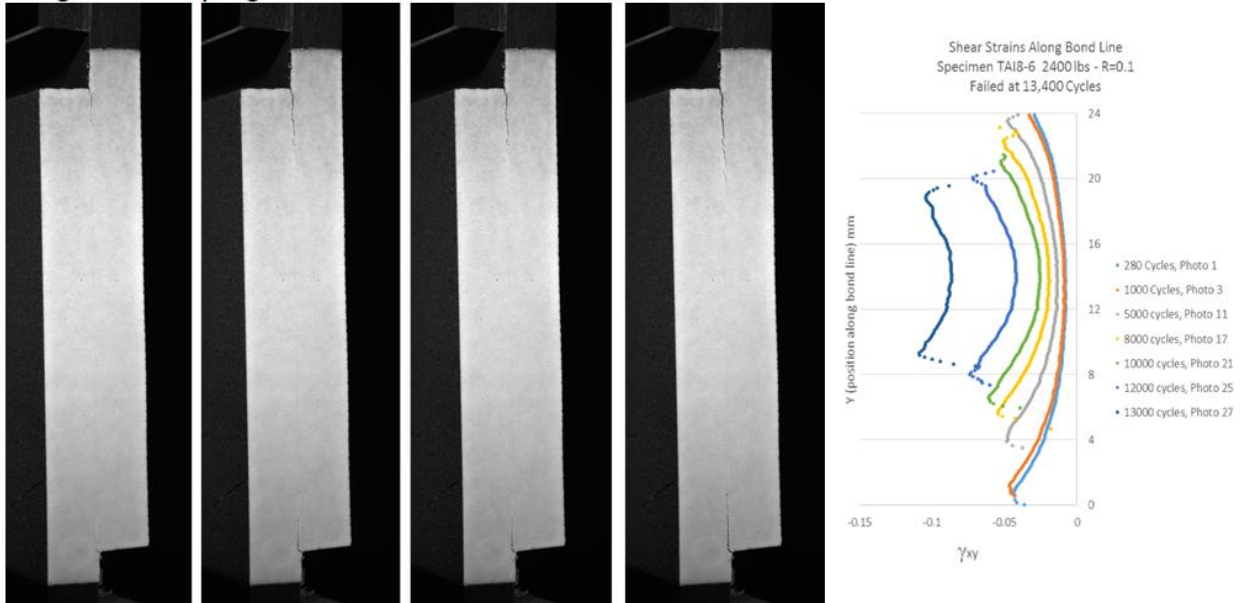


Figure 62. Fatigue Failure Progression in TA Specimens. Strains Along Bondline are shown at Select Cycle Counts

5.2.2 General Procedure

All specimens were painted white on both sides using Krylon White spray paint. One side was finely speckled using an airbrush set at 40psi, to measure crack tip displacements using DIC. The other side was kept white for contrast with the growing crack. By adding millimeter marks, the crack tip was tracked optically during the test. TA specimens were tested in a 20kip capacity Instron servohydraulic load frame. DCB specimens needed much less load, so these were tested in a 2kip capacity Shimadzu electromechanical load frame instead.

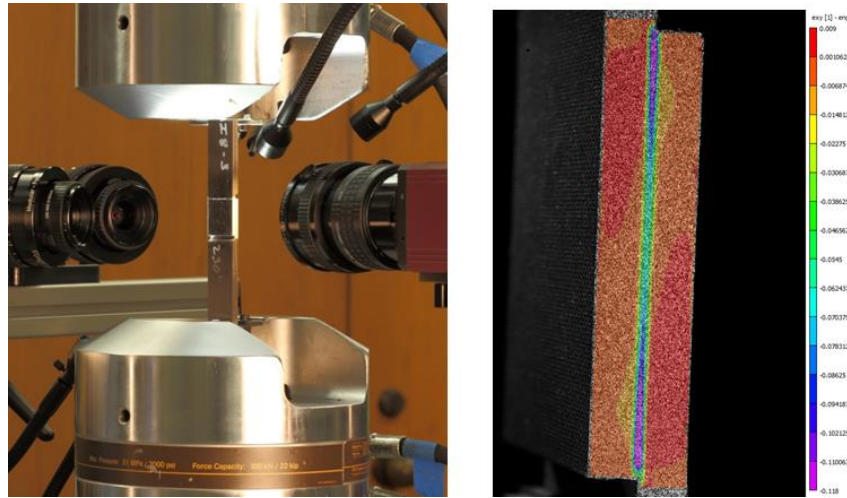


Figure 63. Thick Adherent Test Experimental Setup. A camera on the left tracks crack front optically. The cameras on the right take images of speckled side for DIC.

Testing speed was .02in/min for DCB tests 0.01 in/min for TA tests. DCB specimens were unloaded each 5mm of crack growth. After reaching crack length of 30mm, the DCB cracked specimens were CT scanned under load, such that the crack front was visible in the reconstruction. DCB specimens were retested with the longer crack length. The TA specimens were only tested once, as they break quickly in static loading.

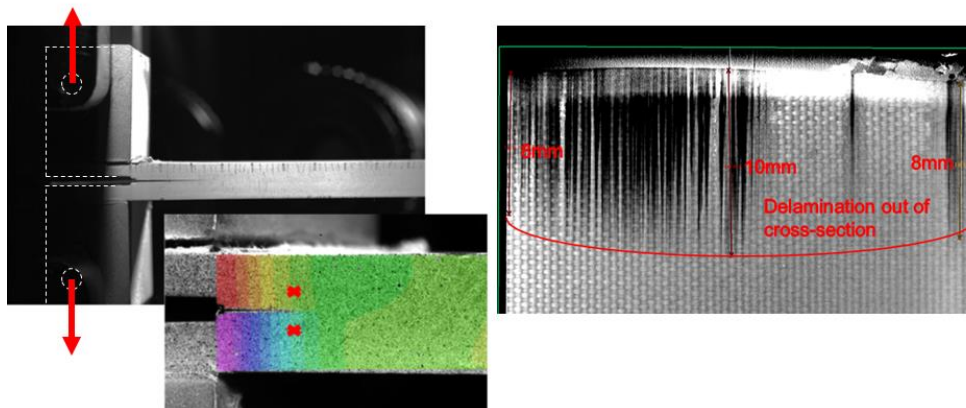


Figure 64. DCB Data. Left: Crack Tip Location and Vertical Displacement Field. The red crosses indicate where crack tip displacements are measured. Right: Crack Front as Reconstructed in CT. Distance measured from groove edge

The crack surfaces in DCB and TA specimens were 3D, as shown in Figure 64. They were mostly within the adhesive but otherwise at the skin-adhesive interface. To simplify analysis, the crack front is assumed to be 2D, halfway through the adhesive thickness.

The cameras in the test setup as shown in Figure 63 have 16MP resolution. One camera is used to track the crack along the length of the specimen, which requires less magnification. The DIC cameras are zoomed in as far as possible. At the DCB test, pixel pitch in DIC is 5 μm , with 34 pixels through the adhesive layer. Because of this high magnification, the crack tip would move out of the field of view, so the cameras were moved and recalibrated for longer crack lengths. The DIC cameras had to see the whole gauge section in TA specimens, so pixel pitch was reduced to 6.2 μm . Figure 64 and Figure 65 show how measurements are taken at 0.5mm away from the actual crack front. While the displacement field should be discontinuous at the crack tip, DIC filtering methods create steep gradients of the displacement field instead, leading to inaccurate results. As a consequence, it is assumed that all measured displacements at the nodes are due to deformation of the bondline.

The displacements and rotations are extracted at the nodes. For analysis of the DCB specimens, the rotation of the skins has a significant influence on the calculated fracture toughness. The difference in vertical displacement of the two measured nodes gives the crack tip separation. A correction for the rotation of the gauge section has to be applied to the crack tip separation measured for TA specimens [98]. This rotation causes an artificial increase in tip separation. The dots in Figure 66 represent three nodes at either side of the bondline as the specimen deforms. The rotation angle must be eliminated via the following equation:

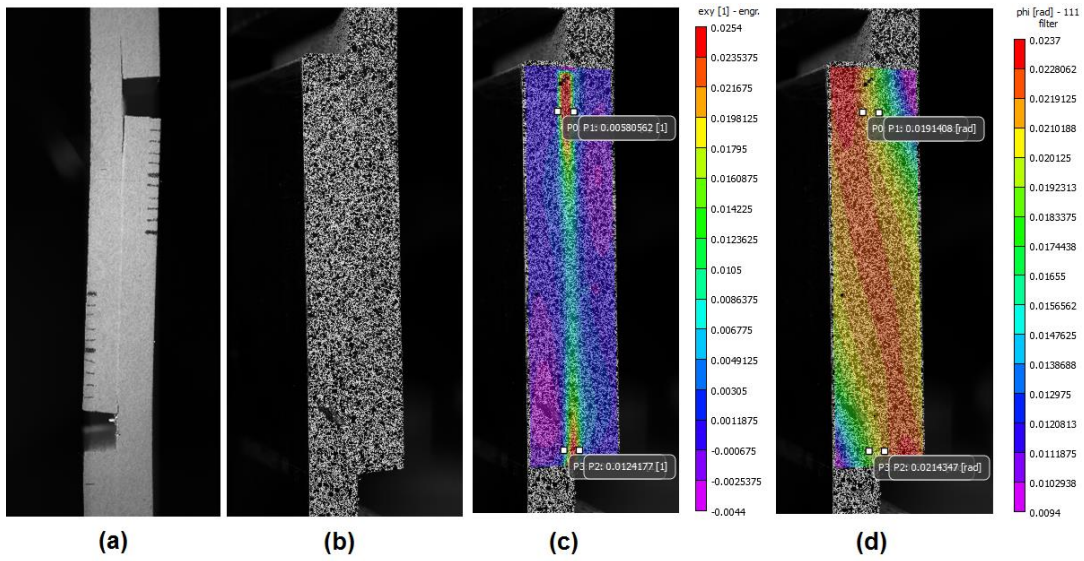


Figure 65. Synchronized Data Captured with Cameras during TA test: (a) Optical Tracking of Crack Length; (b) Deformed Speckle Pattern; (c) Shear Strain Measurements; (d) In-plane Specimen Rotation.

$$\Delta V = (\Delta V_{Left} - \Delta V_{Right}) - dx \tan \theta \quad (5-9)$$

where dx is the horizontal difference between the two measured points and θ is the in-plane rotation as an average of the two nodes.

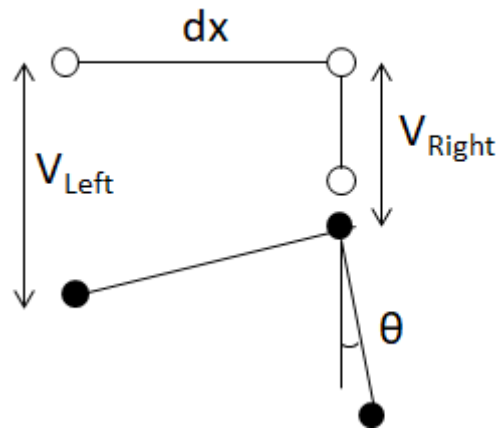


Figure 66. Nodes Along Bondline Undergo Translation and Rotation

5.3 Simulation of DCB and TA Tests in FEA

5.3.1 FEA Models

A numerical study was performed to investigate the numerical sensitivity of traction-separation law parameters to the simulation. For this, the two models in Figure 67 represent the DCB and TA specimens in the ABAQUS/Standard by Dassault Systèmes environment, and both employ the same methodology. The specimen and the adhesive joint were modeled as a 3D solid with C3D8 elements. The free end is pinned, while the loaded edge is loaded in displacement-control. The cohesive interface is modelled as cohesive contact, to be able to extract the contact forces and displacements for the VCCT analysis. The formulation was nodes-to-surface with finite sliding, with cohesive and damage properties as defined in the traction-separation curves. Viscous stabilization coefficient is $1E-4$ to allow for numerical convergence. Mesh refined at the crack tip was based on convergence of specimen load-displacement results.

The FEA model of the TA specimen was used to calculate the fracture energy using the VCCT method. The nodal forces and displacements were taken at the interface of the single lap joint under quasi-static loading were used. The model consisted of two parts; each part has one adherend and one half adhesive layer. The half adhesive layer of each part faces the other such that the cohesive surface is halfway through the bondline thickness. One half-width was simulated thanks to the plane of symmetry. Since the specimen ends are gripped and do not deform, these ends are omitted from the specimen and constrained against rotation. The analysis step is nonlinear and discontinuous, in preparation for the cohesive zone modeling. During the test, the skins were not highly stressed, so the material model was kept linear. The ductile behavior of the adhesive is then captured in the cohesive law. Material properties are given in

Table 12. The adhesive is modeled as isotropic solid with $E = 300\text{ksi}$, $\nu = 0.45$. Adhesive thickness was taken as an average of 0.0068in .

Table 12. Material Properties IM7/8552 used in FEA Simulation [61]

Property	Value
Elastic Modulus E_{11} [Msi]	22.858
Elastic Modulus $E_{22} = E_{33}$ [Msi]	1.282
Poisson's Ratio ν_{12}	0.320
Poisson's Ratio ν_{13}	0.329
Poisson's Ratio ν_{23}	0.461
Shear Modulus G_{12} [Msi]	0.824
Shear Modulus G_{13} [Msi]	0.757
Shear Modulus G_{23} [Msi]	0.456

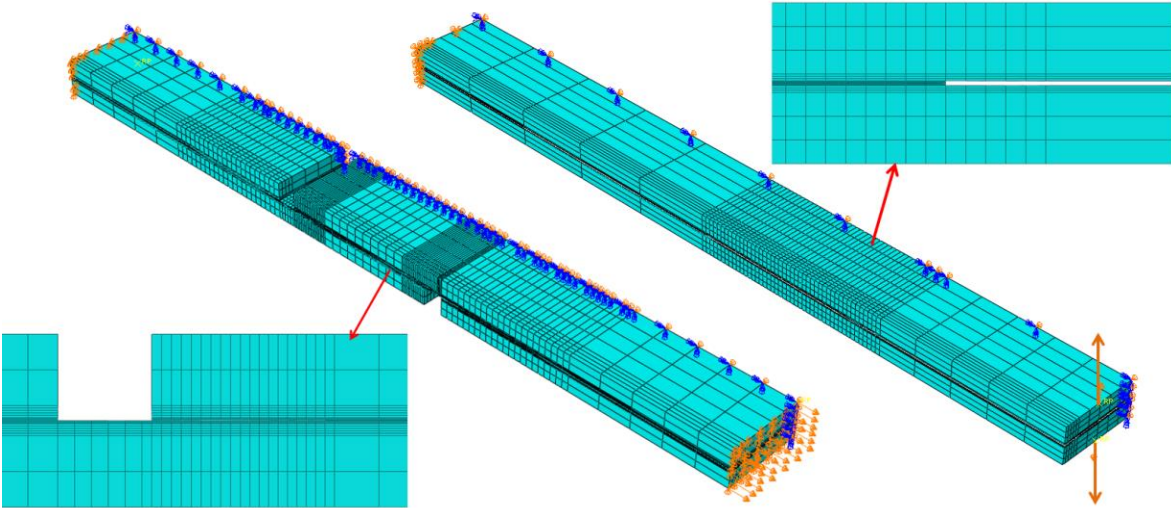
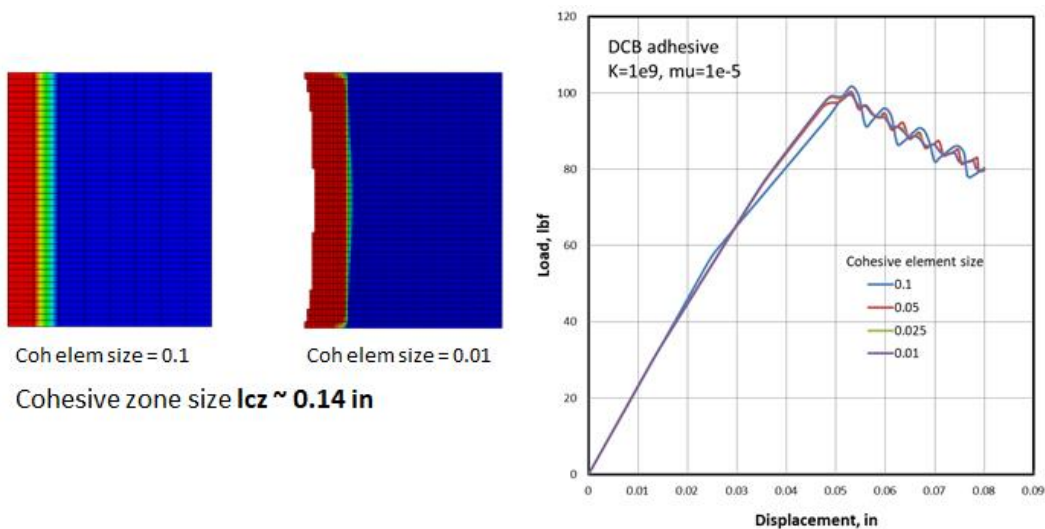


Figure 67. FE Meshed Models for TA (left) and DCB (right) Test Specimens.

5.3.2 Sensitivity of FEA Solution to CZM Modeling Parameters

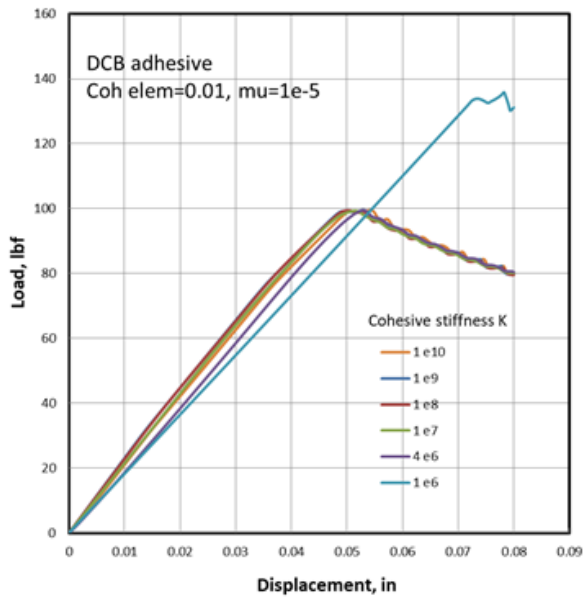
Progressive damage and failure analysis is sensitive to the input parameters of the cohesive elements or cohesive contact. To ensure accurate results, the correct model parameters and cohesive properties must be used. The following sensitivity study applies to the DCB model. The triangular CZM law as in Figure 8 is considered, with parameters G_c , K , and $\sigma_0 = t_n$.

The loaded cohesive zone creates a damage zone near the crack tip (Figure 59). As such, the FEA model must carefully simulate this damage zone, and ideally has about 3 elements between the crack front and the end of the damage zone. Figure 68 shows elements at the bondline at a cohesive zone size of .14in. The red elements are passed the point of maximum stress and are thus in the damaged state. The smaller cohesive element size captures the curved crack front phenomenon, but only marginally changes global response of the specimen.

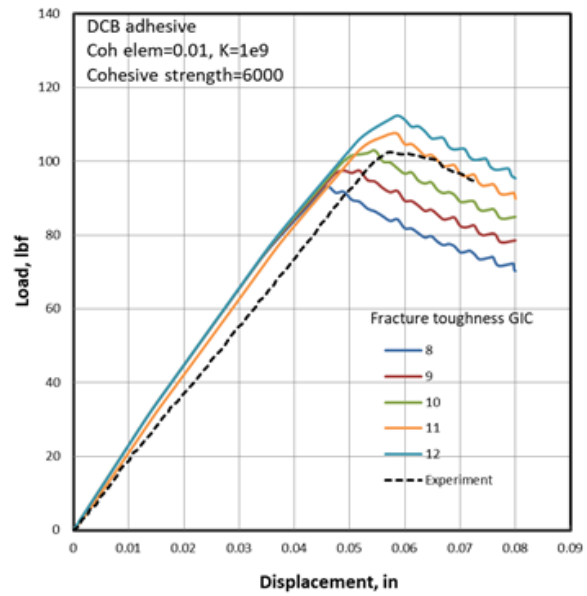


* Note: Graphs courtesy of G. Nikishkov, 2018

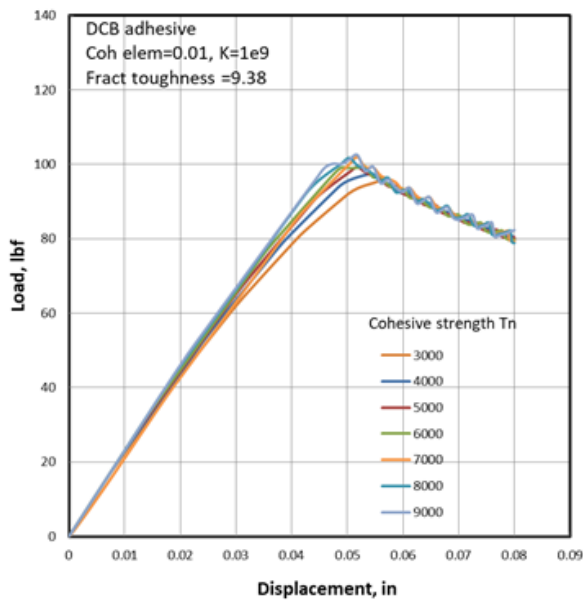
Figure 68. Convergence of Cohesive Element Size in DCB FEA Analysis



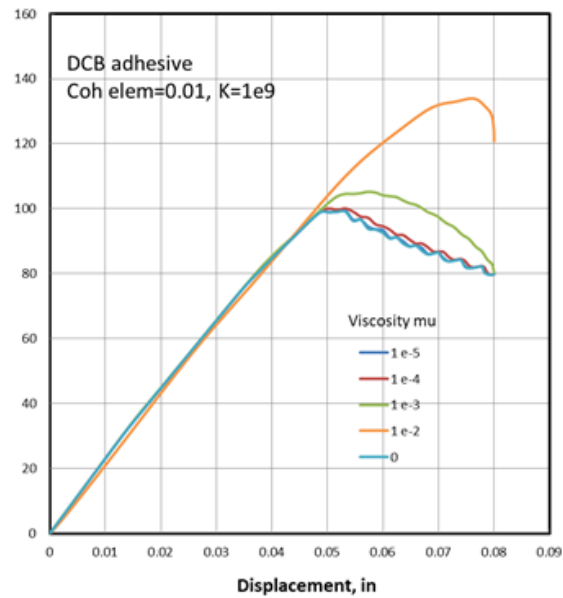
(a)



(b)



(c)



(d)

* Note: Graphs courtesy of G. Nikishkov, 2018

Figure 69. FEA Simulation of DCB Specimen by CZM Triangular Traction-Separation Law. Graphs show Sensitivity to Cohesive Penalty Stiffness (a), Fracture Energy (b), Maximum Traction Stress (c), and Stabilization Viscosity (d)

Figure 69 summarizes the results of the sensitivity study on how the parameters of a triangular CZM law influence global DCB response. The penalty stiffness and maximum traction stress appear to have only a marginal effect on the failure load. The solution is very sensitive to the fracture energy of the CZM law. Viscous regularization of the model is necessary to reach numerical convergence but should be kept under $1E-4$ to prevent excessive energy dissipation. What is not shown is an interaction effect between the penalty stiffness and maximum traction stress. Both parameters influence the cohesive damage zone size. As such, certain combinations of K and t_n result in a very small process zone, at which mesh size can be a limiting factor, leading to erroneous results.

5.4 Derivation of CZM Law

The load-displacement results for DCB specimens were consistent. The global response and R-curve are shown in Figure 70 [68], showing low sensitivity to crack length. Separation displacements at the crack tip were measured using DIC. Lacking a reliable indicator of the crack tip location under the paint, the crack tip was located using CT reconstruction measurements. The shape of the crack front was characterized using CT reconstructions at pretest length $a_0 = 18.5\text{mm}$ and posttest at $a_0 = 30\text{mm}$. The location of the crack tip was marked in the DIC field, which happened to be at a different location than where the paint had cracked. Displacement and rotation measurements were taken at $.5\text{mm}$ above and below the bondline, as shown in Figure 64. The J-integral and the derived traction-separation are calculated and plotted for the three tested specimens at a crack length of 30mm in Figure 71.

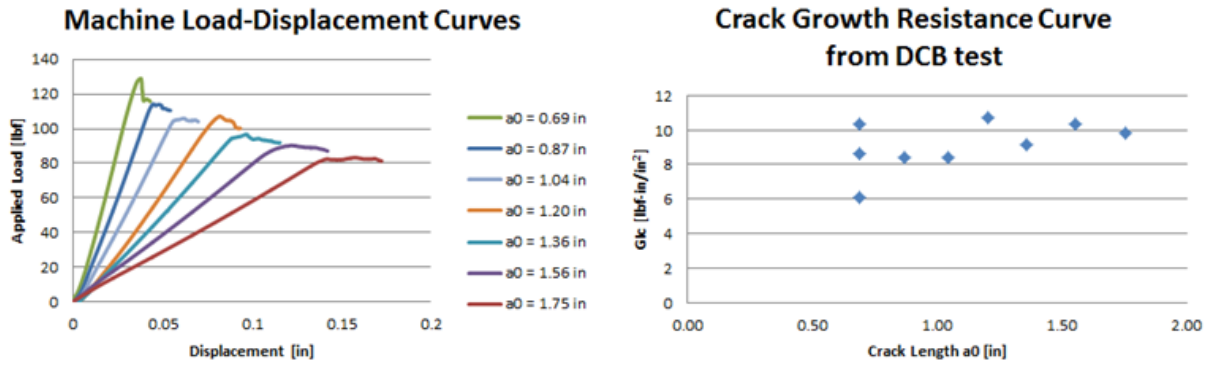


Figure 70. Test Data from DCB Specimens. Left: Load-Displacement Data from the Test Frame. Right: Resistance Curve, in accordance with ASTM standard D5528

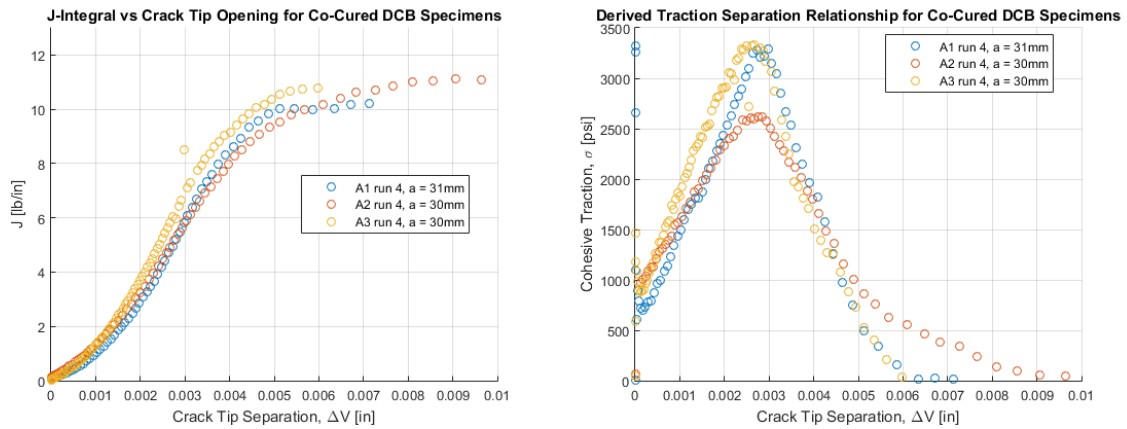


Figure 71. Derivation of the Mode I Cohesive Traction-Separation Law in DCB Specimens. Left: J-integral vs Crack Tip Separation. Right: Traction-Separation Curves.

The traction-separation law in Figure 71 may be reasonably approximated by a triangular shape, with an exception at $\delta = dV = 0$. The damaged down-slope appears to be bi-linear or exponential decay. Note that the penalty stiffness is very low in this curve, and must be including the (in-)elastic behavior of the adhesive. Results are shown for crack length of 30mm. The shorter crack lengths were giving results with very large scatter, while the closed-form solution would have been invalid due to a higher shear force effect. Scatter in the results may be explained by sensitivity to the precise failure mode, which is shown in CT images to vary

between adhesive and adhesive-adherend debonding seemingly at random. The scatter is worse at shorter lengths, where the higher shear force causes extra peeling stresses and the profile of the crack tip through the width has a more pronounced effect. Longer crack lengths would likely have given more favorable results.

The energy release rate in the TA specimens was calculated using the VCCT method in the model as shown in Figure 67 (left). This model was precracked; the top and bottom crack lengths cracks modeled with mesh refinement at the crack front location (see Figure 65). The crack is defined by bonding a node subset of the interface without damage, assuming the crack to be constant through the width. The results for fracture toughness and crack tip separation are shown in Figure 72 and Figure 73 for one specimen. The fracture energy is calculated to be on average between 10-11lb/in, which is very similar to the Mode I fracture energy. Mode II fracture energy is shown to be the dominant driving force for the crack, even though mode I is about 33% of mode II. The derivative of the $G - separation$ curve gives a shape which is easy to fit with a triangle shape. The penalty stiffness term is very low, while the down ramp may also be somewhat bilinear.

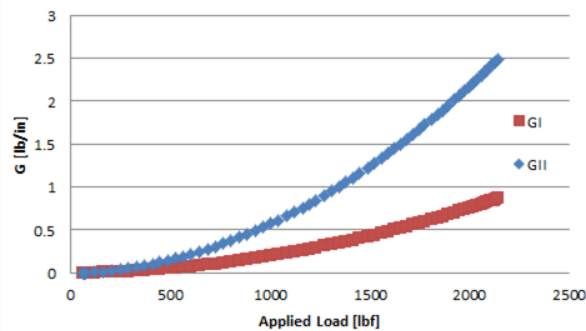


Figure 72. Fracture Energy in the TA Test, as Calculated using VCCT

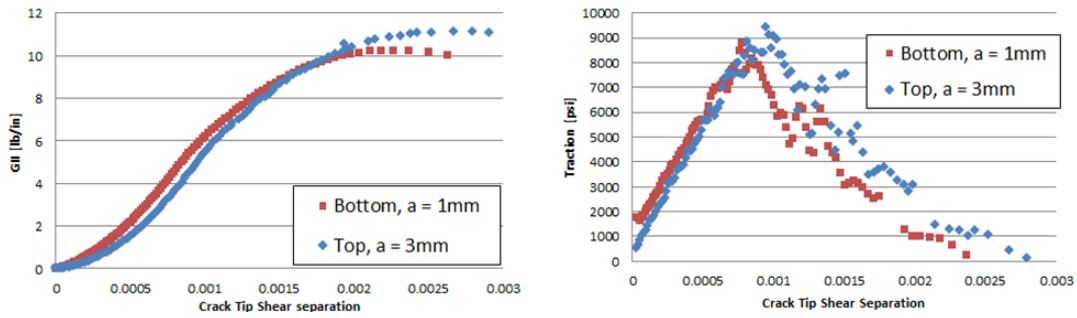


Figure 73. Derivation of Traction-Separation Law in TA specimens. Left: J-integral vs Crack Tip Separation. Right: Traction-Separation Curve.

5.5 Verification by FEA Analysis

5.5.1 Comparison of Global Response

To simulate the global response of DCB and TA tests, the cohesive zone behavior is used as input in the FEA models from Figure 67. By turning on cohesive damage parameters, the FEA model will initiate and grow the crack along the specified interface direction. Shortly after the crack growth begins, maximum load is reached, similar to what happens during the test. The comparison between experimental and FEA load-displacement curves is plotted in Figure 74. The experimental displacement is measured by the crosshead displacement, after a correction for system/fixture compliance. The DCB curve matches the specimen compliance, but has a lower maximum load (98 FEA vs 102 experimental, -4%). Specimen compliance is sensitive to the CZM penalty stiffness term. The reduction in load may be caused by experimental error or choice of average CZM from all three curves shown in Figure 71.

Comparing the specimen compliance between measurement and FEA simulation again gives very positive results for the TA specimen, but the simulation's maximum load significantly overshoots the ultimate strength (4300lbf vs 3940lbf, +9.1%). While the choice of measurement

nodes as in Figure 65 may be responsible for some mismatch, this much error is due to mixed mode failure. As mentioned previously, the mode I crack driving force is about 33% of the mode II, due to a bending moment inside the gauge section. The TA model was rerun with both mode I and mode II cohesive laws, with experimental results approximated by triangle laws. Due to lack of information on mixed mode failure, this criterion was specified with power law of exponent 1. The result is added in Figure 74 as the black line, and clearly reduces the simulated maximum load and stretch before failure. The ultimate load is much improved, but the mixed-mode failure warrants further investigation.

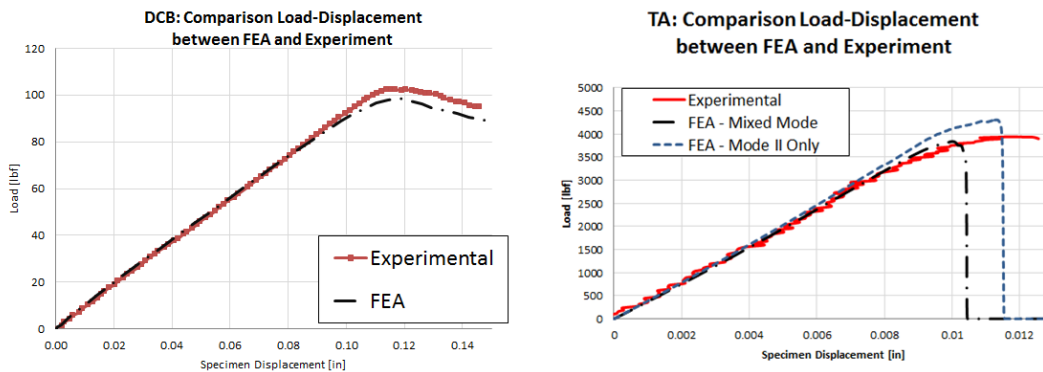


Figure 74. Comparison Global Numerical and Experimental Specimen Load-Displacement Measurements for DCB (Left) and TA (Right).

5.5.2 Sensitivity of Solution to Measurement Location in DCB Specimens

According to simulations and measurements, deformations in DCB and TA specimens are a function of location. As the nodal displacements are direct input for the CZM measurements, sensitivity is high; Taking measurements behind or in front of the crack tip will lead to a change in the estimate of penalty stiffness and maximum traction. Figure 75 shows the effect of taking measurement in front or behind the crack tip.

The crack front can be measured within 1mm accuracy in CT reconstruction analysis. If the placement of the measurement nodes exceeds 1mm away from the crack front, the maximum traction and penalty stiffness term are significantly affected. These CZM laws lead to significant errors in global response as simulated in FEA. Sensitivity of the measurement node locations in the direction normal to the bondline is much lower as strain and displacement gradients are lower in these directions.

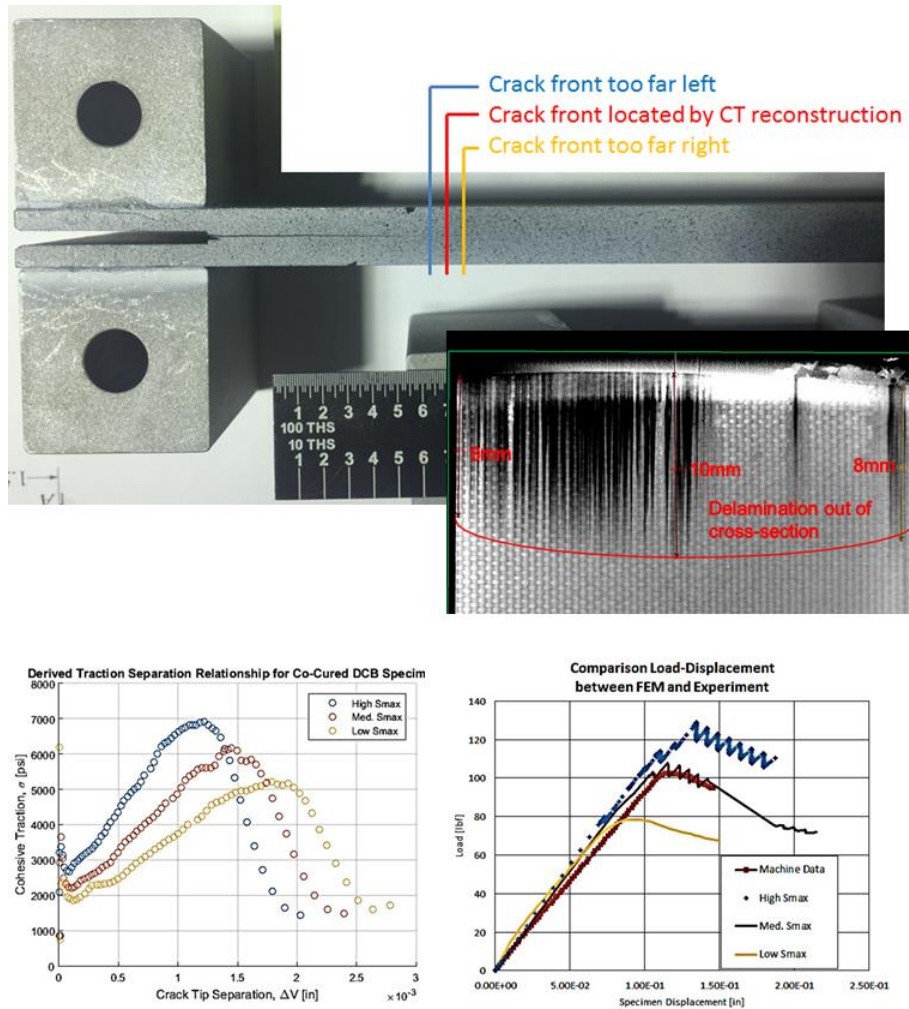


Figure 75. Sensitivity of Traction-Separation Law to Crack Tip Measurement in DCB Specimens.

5.5.3 Application to TA Specimen Without Adhesive

A batch of three specimens have of co-cured IM7/8552 specimens were manufactured without adhesive. A panel of .25in. thick was machined by grinding two grooves exactly half the thickness deep. These specimens were precracked in fatigue and scanned under load. Scanning under load opened the crack to facilitate the identification of the crack tip. Typical measurements are shown in Figure 76. The experiment did not show complications; the crack growth in fatigue was very stable; The 3deg off-axis plies at the interface prevented fiber bridging. Without the adhesive layer, the composite skins were subject to large shear stresses, and crack grow along a near-zero thickness interface. This in contrast to TA specimens with adhesive, which had all ductile and fracture failure within a finite thickness adhesive zone.

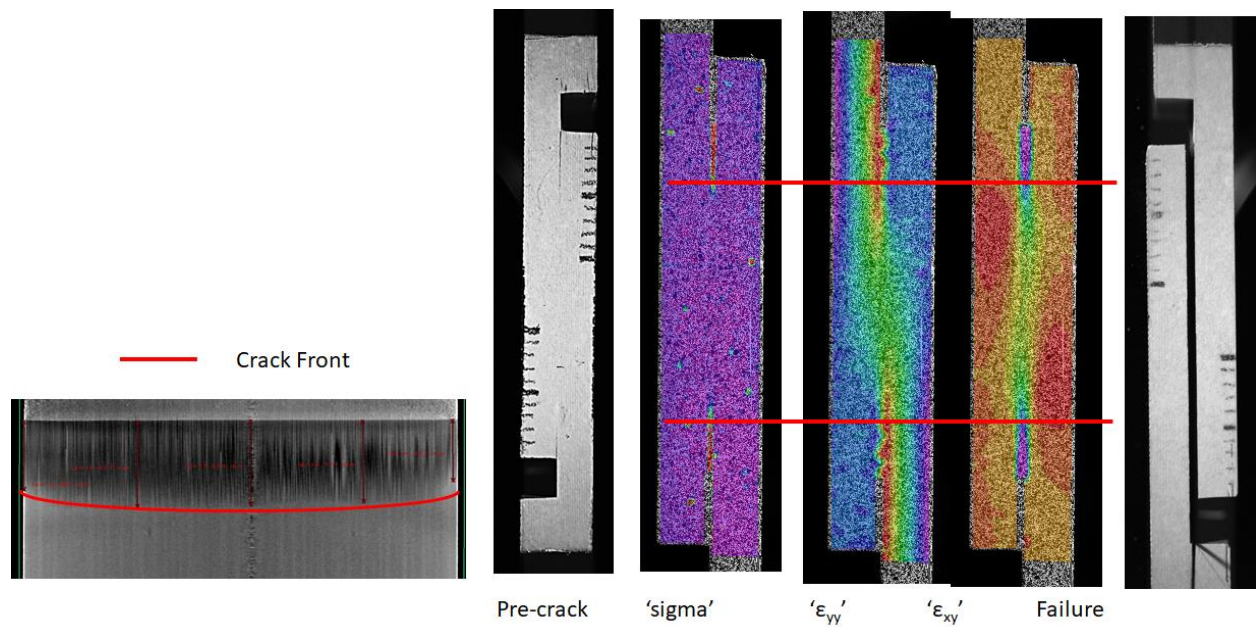


Figure 76. CT and Optical Measurements of IM7/8552 TA Specimens without Adhesive

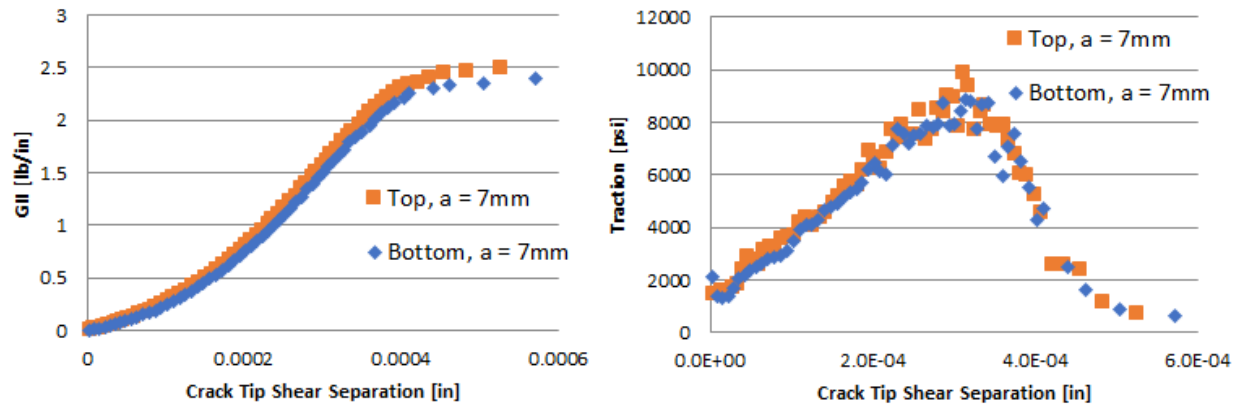


Figure 77. CZM Characterization of IM7/8552 Specimens

The analysis for the TA specimens was unchanged for the specimens without adhesive. Crack tip measurements were taken within .125in. of either side of the interface. The G_{II} fracture energy was calculated using VCCT using a model without an adhesive layer. The results are summarized in Figure 77. Striking is a large difference in fracture toughness G_{IIc} and smaller maximum crack tip shear separation. A low penalty stiffness is defined, which is counter-intuitive [81]. Using this method, the shear deformation of the skins before fracture is included within the CZM law.

5.5.4 Characterizing Bondline Shear Stress-Strain Response

Insight in the adhesive stress-strain response was used to create understanding of the CZM law. The ASTM D5656 [71] is used to measure stress-strain behavior of adhesive in shear loading. Strain measurements are performed via the KGR, a dedicated extensometer fixture. This extensometer will accurately measure strains at one-point location. By assuming stress and strain are constant through the cross-section, a stress-strain relationship is established. Consider Figure 65, where shear strains are shown to be heterogeneous through the cross-section. Taking a

measurement at a single point is unlikely to represent the distribution of strains that exist. If measured at the center of the specimen, the KGR method cannot be accurate.

A virtual test was performed to develop an appropriate analysis for the stress-strain behavior at the bondline. Using full-field strain field measurements from FEA, all strains along the bondline are known. This gives different options to calculate the material properties. The first method is a virtual KGR measurement (as in Figure 78). Three measurement points in the FEA analysis act as an extensometer. For details, refer to ASTM D5656 [71]. Another method is to plot average stress P/A over strains in the middle of the bondline and average stress over average bondline strains. Additionally, an optimization method was developed to optimize the stress-strain curve to satisfy the equilibrium conditions (as in section 2.4). The integration of the stresses over the cross-section must be equal to the applied load. The optimization scheme is shown in Figure 79 (left).

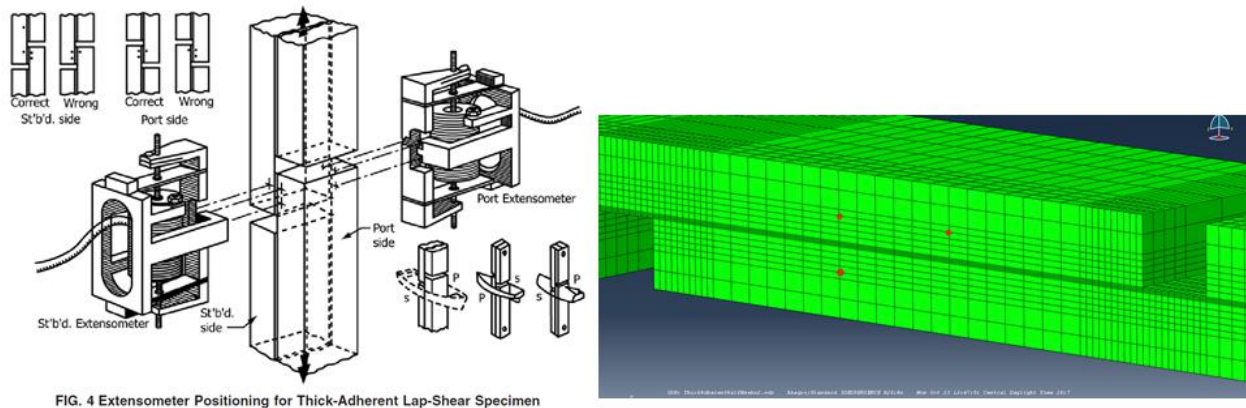


Figure 78. Simulation of KGR Strain Measurement in FEA

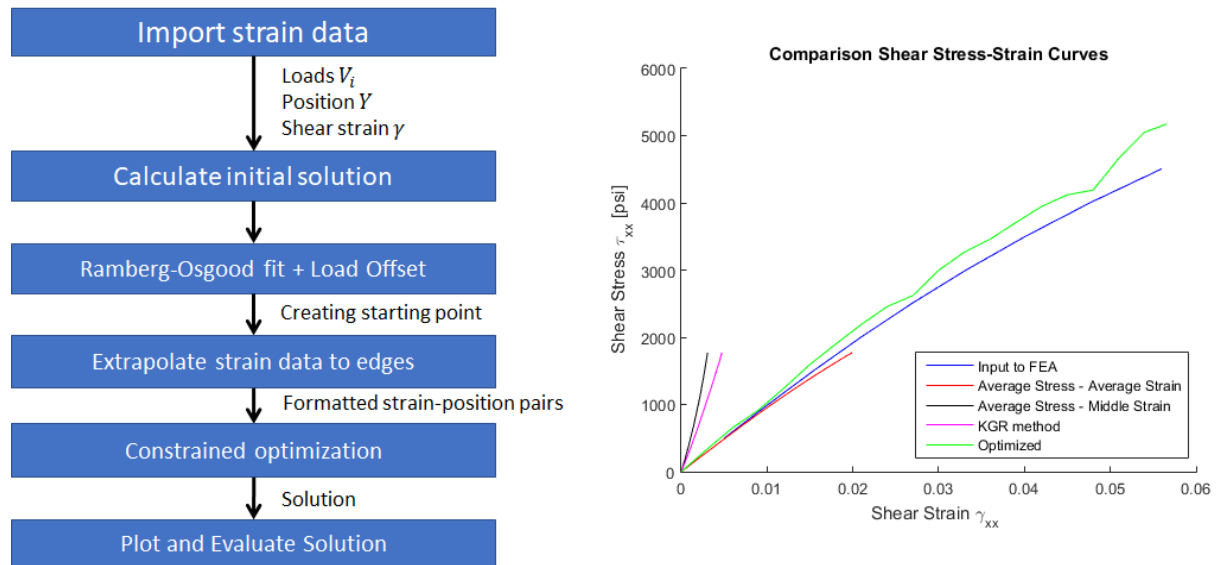


Figure 79. Comparison of Stress-Strain Characterization Analyses for TA Specimens. The Flowchart for the Optimization Method is shown Left.

Comparing the outcome of the virtual experiment and analyses confirms that the KGR method cannot accurately define the stress-strain behavior of the bondline. Plotting average stress against the average measured strain in the bondline gives a reasonable estimate of the stress-strain behavior. However, maximum strains at the free edges are averaged out and lost in this method. By contrast, the optimization method can characterize the stress-strain behavior up to failure strain. The downside to the optimization method is sensitivity to noise in the data. The optimization and average stress-average strain methods were applied to the co-cured TA specimens with adhesive and the result is plotted in Figure 80. It shows significant nonlinear behavior. This nonlinear behavior is a significant part of the total global specimen behavior. As thus, cohesive failure is a combination of shear nonlinear stress-strain and fracture behavior [99]. Future work could address isolating fracture behavior from global response.

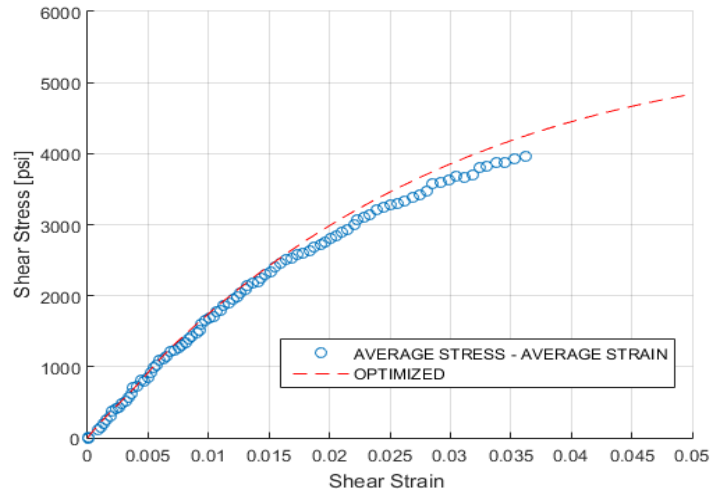


Figure 80. Measured Nonlinear Stress-Strain Behavior of Adhesive in TA Specimens

5.6 Discussion of Results

The approach presented in this chapter was used to directly measure the cohesive laws for co-cured specimens, without the use of iterative numerical FEA analyses. High-resolution and high-magnification DIC techniques were applied to measure the mode I and mode II fracture properties. Importantly, the J-integral and VCCT methods were both adequate to determine the fracture energy to derive the cohesive laws for the DCB and TA specimens.

The importance of micro-focus X-ray CT scans of the crack front cannot be overstated. As shown in this chapter, the crack tip separation measurements are very sensitive to the placement of the measurement nodes. The paint does not necessarily crack at the same strain level as the adhesive, so using only visual identification of the crack tip, there was too much scatter in the results. By scanning the specimen (under load) before testing, the crack tip was accurately found, which improved quality of the results.

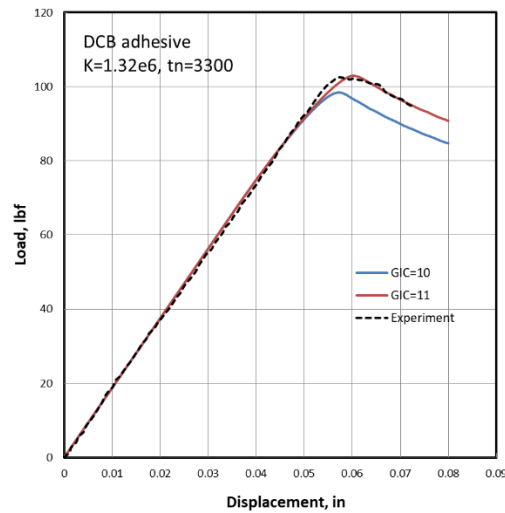


Figure 81. Adjustment of G_{Ic} of CZM Law to Improve Agreement between FEA Simulation and Measurement Data

Numerical analyses of the DCB and TA specimens in ABAQUS/standard were performed to verify the measured cohesive laws by comparing the load-displacement curve between simulation and measurement. Both the DCB and TA models matched global compliance, and the DCB maximum load simulation was very close to the measured maximum load. The TA model with mode II fracture properties overestimated the failure load by 9.1%, because it did not take mixed-mode failure into account. When mode I CZM properties were added to the simulation, the specimen strength was within 2.5% of the measured strength. Further refinement of the results may be obtained by investigating mixed mode failure laws.

A hybrid direct- and updating FEMU method may be used to improve accuracy of the CZM law. The direct method could verify the shape of the cohesive law, of which the parameters may be optimized with FEA analysis. An example of such hybrid analysis is shown in Figure 81. Compared to Figure 74, the agreement with global response is improved by adjusting the fracture toughness.

CHAPTER 6

CONCLUSIONS, DISCUSSION, AND FUTURE WORK

The body of this work addressed the challenge to accurately identify material parameters of carbon fiber reinforced polymer composites through advanced experimental methods that capture the full three-dimensional material behavior. The importance of measuring transverse shear nonlinear stress-strain and fracture properties is highlighted. Many failure models are highly sensitive to these complex failure phenomena, which are notoriously hard to measure.

An optimization method was introduced to analyze specimens subject to heterogeneous stress state. The method captures the complex constitutive properties of the composite material in a computationally effective, accurate, and flexible procedure without ad hoc assumptions of the material model. To identify multiple material parameters in a single test method, specimens were loaded in multi-axial stress states. Full-field noncontact deformation measurements by DIC of these specimens provided overdetermined data used for material characterization. The characterization of the orthotropic and nonlinear stress-strain behavior poses an inverse problem. The proposed method links the measured strain distribution to the applied load, by optimization of material stress-strain cubic spline parameters. As such, nonlinear stress-strain curves can be defined without a material model. Comparison to FEA analysis proved this method is accurate.

The optimization method was applied to the D2344 3-Point Bend and D5656 Thick Adherend tensile tests. These tests were used to characterize nonlinear shear behavior of bulk material and adhesives, respectively. The shear properties found in this analysis method are not

very sensitive to model and analysis parameters, and the moduli are derived from the results via regression analysis.

Overdetermined strain distribution information from full-field DIC measurements increases confidence in material parameters and can be used to verify simplifying assumptions. The assumption of transverse isotropy of polymer composites is often not substantiated. The SBS test is shown to provide shear stress-strain properties which agree very well with the nonlinear properties derived from the SPT test, which were analyzed with FEMU analysis. Full 3D nonlinear lamina characterization verifies whether the assumption of transverse isotropy is valid. Data showed that this assumption depends on microstructure topology. The IM7/8552 carbon fiber epoxy exhibits transverse isotropic behavior, but data showed that the assumption was not valid for material X.

The shear behavior derived from SBS specimens agrees very well with the SPT test results, but not with the ASTM D3518 test. These 45deg off-axis tensile specimens agree in the linear regime but shear behavior deviates after about 4000-5000 μ strain. The tensile test results are dependent on stacking sequence, overall specimen thickness, and suffer from complex mixed-mode micro-scale damage development. This damage is shown to start well before damage can be seen in X-ray CT reconstructions.

Across the wide range of available shear characterization methods, obtaining a pure shear failure mode is still challenging. In the SBS test, certain materials can withstand large amount of shear deformation and will still fail in mixed-mode failure at the contacts. Legacy FEMU and first-order solutions do not provide the flexibility or accuracy to characterize high-strain material behavior. The short beam shear specimen offers great flexibility in the design of experiments,

allowing the user to influence what failure modes and mechanical properties are measured. This work showed how an offset span ratio for the SBS test can increase the chance of pure shear failure. By using optimization methods described in this thesis, large shear strain response greater than 5% can be characterized. Results are shown to be consistent between various span and offset configurations.

Flexibility in the design of experiments will allow for more detailed investigations in the nonlinear and complex deformation and failure behavior of polymer composites. By varying the 3-Point Bend configurations, the material may be subject to a wide range of axial and shear loading combinations, leading to a set of mixed-mode failure criteria to be used for PDFA methods. Future work performed should take advantage of the flexibility of the SBS method to define new parameters, such as to define the multi-axial failure (or yielding) envelope, as well as time-dependent and fatigue behavior. Future studies may also investigate the use of optimization models for the use in other test methods subject to either plane stress or plane strain conditions. 4-Point Bending tests of straight or curved beams are possible subjects.

Experimental methods and nonupdating analysis techniques were applied to capture the interface traction-separation law and increase confidence in material input data for PDFA. Direct measurement of traction-separation cohesive laws in Mode I and Mode II fracture was proven to be feasible. DCB and TA specimens, made of IM7/8552 skins co-cured with a film adhesive, were tested with high-magnification DIC measurements at the crack tip. The thick adherend as a predominant mode II fracture test exhibited the proper failure modes. The traction-separation law was derived from crack tip displacements extracted from the DIC displacement fields at the crack tip. The J-integral and VCCT method were both found to be appropriate methods for

obtaining fracture toughness. Micro-focus X-ray Computed Tomography (CT) scans of the crack front were critical to obtain an accurate result.

Global response of the DCB and TA simulation with CZM model derived from test results compared very favorable to the experimental load-displacement curve. Further study will be required to separate true cohesive laws from the specimen response including the compliance of adherend materials, and reversible and inelastic strain from the adhesive. Specimen diversity especially for shear may be used for verification purposes. Reaching beyond, these methods may be used to define static and fatigue cohesive damage laws for composite structures with or without adhesive.

REFERENCES

- [1] US Department of Defense. Composite Materials Handbook MIL-HDBK-17-1F. vol. 1/5. 2002.
- [2] Nikishkov Y, Makeev A, Seon G. Progressive fatigue damage simulation method for composites. *Int J Fatigue* 2013;48:266–79. doi:10.1016/j.ijfatigue.2012.11.005.
- [3] ASTM. D 4762 Standard Guide for Testing Polymer Matrix Composite Materials 1. ASTM Stand 2017;D2344-16:1–22. doi:10.1520/D4762-16.2.
- [4] Chaterjee S, Adams DF, Oplinger DW. Test Methods for Composites a Status Report; Volume III. Shear Test Methods. Blue Bell, PA 19422: 1993.
- [5] Ramault C, Makris A, Sol H, Hemelrijck D Van, Lecompte D, Lamkanfi E. Development of an Inverse Method for Material Characterization using a Biaxially Loaded Cruciform Composite Specimen. *Proc SEM Annu Conf* 2009.
- [6] Gu X, Pierron F. Towards the design of a new standard for composite stiffness identification. *Compos Part A Appl Sci Manuf* 2016;91:448–60. doi:10.1016/j.compositesa.2016.03.026.
- [7] Seon G, Makeev A, Van Der Vossen B, Schaefer J, Justusson B. DIC data driven methods to verify simplifying assumptions and increase confidence in material properties of laminated composites. *32nd Tech. Conf. Am. Soc. Compos.* 2017, vol. 2, 2017.
- [8] Van Der Vossen B, Makeev A. Characterization of Cohesive Zone Laws using Digital Image Correlation. *18th US-Japan Conf. Compos. Mater.*, Seattle, WA, USA: 2018, p. 916–30.
- [9] Grédiac M, Auslender F, Pierron F. Applying the virtual fields method to determine the through-thickness moduli of thick composites with a nonlinear shear response. *Compos Part A Appl Sci Manuf* 2001;32:1713–25.
- [10] Hahn HT, Tsai SW. Nonlinear Elastic Behavior of Unidirectional Composite Laminae. *J Compos Mater* 1973;7:102–18. doi:10.1177/002199837300700108.
- [11] Sun W, Lau ACW. Three-Dimensional Constitutive Model for Anisotropic Inelastic Deformation of Unidirectional Reinforced Composites. *J Thermoplast Compos Mater* 2002;15:477. doi:10.1106/089270502023204.
- [12] Sabik A. Direct shear stress vs strain relation for fiber reinforced composites. *Compos Part B Eng* 2018;139:24–30. doi:10.1016/j.compositesb.2017.11.057.

- [13] Mandel U, Taubert R, Hinterhölzl R. Three-dimensional nonlinear constitutive model for composites. *Compos Struct* 2016;142:78–86. doi:10.1016/j.compstruct.2016.01.080.
- [14] Eskandari S, Andrade Pires FM, Camanho PP, Marques AT. Intralaminar damage in polymer composites in the presence of finite fiber rotation: Part II – Numerical analysis and validation. *Compos Struct* 2016;151:127–41. doi:10.1016/j.compstruct.2016.01.048.
- [15] Makeev A, He Y, Carpentier P, Shonkwiler B. A method for measurement of multiple constitutive properties for composite materials. *Compos Part A Appl Sci Manuf* 2012;43:2199–210.
- [16] Puck A, Schürmann H. Failure Analysis of FRP Laminates by means of Physically based Phenomenological Models. *Compos Sci Technol* 1998;58:1045–67.
- [17] Camanho PP, Dávila CG, Pinho ST, Iannucci L, Robinson P. Prediction of in situ strengths and matrix cracking in composites under transverse tension and in-plane shear. *Compos Part A Appl Sci Manuf* 2006;37:165–76. doi:10.1016/j.compositesa.2005.04.023.
- [18] Courtney TH. *Mechanical Behavior of Materials* 1990:351–65.
- [19] Vogler T., Kyriakides S. Inelastic behavior of an AS4/PEEK composite under combined transverse compression and shear. Part I: experiments. *Int J Plast* 1999;15:783–806. doi:10.1016/S0749-6419(99)00011-X.
- [20] Vogler TJ, Hsu S-Y, Kyriakides S. Composite failure under combined compression and shear. *Int J Solids Struct* 2000;37:1765–91. doi:10.1016/S0020-7683(98)00323-0.
- [21] Pettersson KB, Neumeister JM, Kristofer Gamstedt E, Öberg H. Stiffness reduction, creep, and irreversible strains in fiber composites tested in repeated interlaminar shear. *Compos Struct* 2006;76:151–61. doi:10.1016/j.compstruct.2006.06.021.
- [22] Adams DF, Carlsson LA, Pipes RB. *Experimental characterization of advanced composite materials*. CRC Press LLC; 2003.
- [23] Czichos H, Saito T, Smith L, editors. *Springer Handbook of Materials Measurement Methods*. Springer Science+Business Media, Inc.; 2006.
- [24] Sharpe W. *Springer Handbook of Experimental Solid Mechanics*. New York, NY: Springer Science+Business Media, Inc.; 2008.
- [25] Sutton MA, Orteu J, Schreier HW, editors. *Image Correlation for Shape, Motion and Deformation Measurements*. New York, NY: Springer Science+Business Media, LLC; 2009.
- [26] Potter KD. *Understanding the Origins of Defects and Variability in Composites*

- Manufacture. 17th Int. Conf. Compos. Mater., Edinburgh, UK: 2009.
- [27] Tomblin J, Seneviratne W. Laminate Statistical Allowable Generation for Fiber-Reinforced Composite Materials : Lamina Variability Method. 2009.
- [28] Hexcel Composites. HexPly ® 8552 Product Data. 2013.
- [29] Marlett K. Hexcel 8552 IM7 Unidirectional Qualification Material Property Data Report. Wichita: 2011.
- [30] Genovese K, Lamberti L, Pappalettere C. A new hybrid technique for in-plane characterization of orthotropic materials. *Exp Mech* 2004;44:584–92. doi:10.1177/0014485104048907.
- [31] Leclerc H, Périé JN, Roux S, Hild F. Integrated digital image correlation for the identification of mechanical properties. *Mirage* 2009 2009;LNCS 5496:161–71.
- [32] Grédiac M. The use of full-field measurement methods in composite material characterization: interest and limitations. *Compos Part A Appl Sci Manuf* 2004;35:751–61. doi:10.1016/j.compositesa.2004.01.019.
- [33] Van Paepegem W, De Baere I, Degrieck J. Modelling the nonlinear shear stress-strain response of glass fibre-reinforced composites. Part I: Experimental results. *Compos Sci Technol* 2006;66:1455–64. doi:10.1016/j.compscitech.2005.04.014.
- [34] Precision WS. Standard Test Method for Short-Beam Strength of Polymer Matrix Composite Materials. *Annu B ASTM Stand* 2011;00:1–8. doi:10.1520/D2344.
- [35] Carpentier AP. Advanced Materials Characterization based on Full Field Deformation Measurements. University of Texas at Arlington, 2013.
- [36] He Y. Matrix-Dominated Constitutive Laws for Composite Materials. Georgia Institute of Technology, 2010.
- [37] Cline J. Accurate Three-dimensional Characterization of the Nonlinear Material Constitutive Properties for Laminated Composite Materials. The University of Texas at Arlington, 2015.
- [38] Van Der Vossen B. Spatial Variability of Stiffness in Fiber Reinforced Composites in Short Beam Shear Test Specimens. Delft University of Technology, 2014.
- [39] Whitney JM. Experimental Characterization of Delamination Fracture. vol. 5. Elsevier Inc.; 1989. doi:10.1016/B978-0-444-87285-2.50008-X.
- [40] Seon G, Makeev A, Cline J, Shonkwiler B. Assessing 3D shear stress-strain properties of composites using Digital Image Correlation and finite element analysis based

- optimization. *Compos Sci Technol* 2015;117:371–8. doi:10.1016/j.compscitech.2015.07.011.
- [41] He Y, Makeev A, Shonkwiler B. Characterization of nonlinear shear properties for composite materials using digital image correlation and finite element analysis. *Compos Sci Technol* 2012;73:64–71. doi:10.1016/j.compscitech.2012.09.010.
- [42] ASTM D3518. Standard Test Method for In-Plane Shear Response of Polymer Matrix Composite Materials by Tensile Test of a 45 ° Laminate 1. *Annu B ASTM Stand* 2007;94:1–7. doi:10.1520/D3518.
- [43] Giannadakis K, Varna J. Analysis of nonlinear shear stress-strain response of unidirectional GF/EP composite. *Compos Part A Appl Sci Manuf* 2014;62:67–76. doi:10.1016/j.compositesa.2014.03.009.
- [44] Gurvich MR, Clavette PL. Probabilistic Characterization of Elastic Properties of Composites Using Digital Image Correlation Technique. In: Patterson E, Backman D, Cloud G, editors. *Compos. Mater. Join. Technol. Compos.* Vol. 7, vol. 7, New York, NY: Springer New York; 2012, p. 93–8. doi:10.1007/978-1-4614-4553-1.
- [45] Reddy JN. *Mechanics of laminated composite plates and shells: theory and analysis.* 2003. doi:10.1007/978-1-4471-0095-9.
- [46] Bednarczyk B, Aboudi J, Yarrington PW. Determination of the Shear Stress Distribution in a Laminate From the Applied Shear Resultant — A Simplified Shear Solution. *Ohio*: 2007. doi:10.13140/2.1.3629.9521.
- [47] Zenkour AM. Generalized shear deformation theory for bending analysis of functionally graded plates. *Appl Math Model* 2006;30:67–84. doi:10.1016/j.apm.2005.03.009.
- [48] Magnucki K, Malinowski M, Magnucka-Blandzi E, Lewiński J. Three-point bending of a short beam with symmetrically varying mechanical properties. *Compos Struct* 2017;179:552–7. doi:10.1016/j.compstruct.2017.07.040.
- [49] Molimard J. Identification of the Four Orthotropic Plate Stiffnesses Using a Single Open-hole Tensile Test. *Exp Mech* 2005;45:404–11. doi:10.1177/0014485105057757.
- [50] Lecompte D, Smits A, Sol H, Vantomme J, Van Hemelrijck D. Mixed numerical–experimental technique for orthotropic parameter identification using biaxial tensile tests on cruciform specimens. *Int J Solids Struct* 2007;44:1643–56. doi:10.1016/j.ijsolstr.2006.06.050.
- [51] Avril S, Bonnet M, Bretelle A-S, Grédiac M, Hild F, Jenny P, et al. Overview of Identification Methods of Mechanical Parameters Based on Full-field Measurements. *Exp Mech* 2008;48:381–402. doi:10.1007/s11340-008-9148-y.

- [52] Chan a., Chiu WK, Liu XL. Determining the elastic interlaminar shear modulus of composite laminates. *Compos Struct* 2007;80:396–408. doi:10.1016/j.compstruct.2006.05.025.
- [53] Cugnoni J, Gmür T, Schorderet A. Inverse method based on modal analysis for characterizing the constitutive properties of thick composite plates. *Comput Struct* 2007;85:1310–20. doi:10.1016/j.compstruc.2006.08.090.
- [54] Grédiac M, Pierron F. Applying the Virtual Fields Method to the identification of elasto-plastic constitutive parameters. *Int J Plast* 2006;22:602–27. doi:10.1016/j.ijplas.2005.04.007.
- [55] Grédiac M, Toussaint E, Pierron F. Special virtual fields for the direct determination of material parameters with the virtual fields method . 2 — Application to in-plane properties. *Compos Part A Appl Sci Manuf* 2002;32:2707–30.
- [56] Avril S, Bonnet M, Bretelle AS, Grédiac M, Hild F, Jenny P, et al. Overview of identification methods of mechanical parameters based on full-field measurements. *Exp Mech* 2008;48:381–402. doi:10.1007/s11340-008-9148-y.
- [57] He T, Liu L, Makeev A, Shonkwiler B. Characterization of stress-strain behavior of composites using digital image correlation and finite element analysis. *Compos Struct* 2016;140:84–93. doi:10.1016/j.compstruct.2015.12.018.
- [58] Haj-Ali R, Kim H-K. Nonlinear constitutive models for FRP composites using artificial neural networks. *Mech Mater* 2007;39:1035–42. doi:10.1016/j.mechmat.2007.05.004.
- [59] Makeev A, Nikishkov Y, Cross R, Armanios E. Empirical Modeling Based on Neural Networks and Bayesian Learning. 45th AIAA/ASME/ASCE/AHS/ASC Struct. Struct. Dyn. Mater. Conf., vol. 1, Palm Springs: American Institute of Aeronautics and Astronautics; 2004, p. 1–13.
- [60] da Silva LFM, Campilho RDSG. Advances in Numerical Modeling of Adhesive Joints. 2012. doi:10.1007/978-3-642-23608-2.
- [61] Nikishkov Y, Seon G, Makeev A, Shonkwiler B. In-situ measurements of fracture toughness properties in composite laminates. *Mater Des* 2016;94:303–13. doi:10.1016/j.matdes.2016.01.008.
- [62] Su ZC, Tay TE, Ridha M, Chen BY. Progressive damage modeling of open-hole composite laminates under compression. *Compos Struct* 2015;122:507–17. doi:10.1016/j.compstruct.2014.12.022.
- [63] Camanho P, Davila CG. Mixed-Mode Decohesion Finite Elements in for the Simulation Composite of Delamination Materials. *Nasa* 2002;TM-2002-21:1–37.

doi:10.1177/002199803034505.

- [64] Camanho PP, Bessa MA, Catalanotti G, Vogler M, Rolfes R. Modeling the inelastic deformation and fracture of polymer composites-Part II: Smearred crack model. *Mech Mater* 2013. doi:10.1016/j.mechmat.2012.12.001.
- [65] Song K, Davila C, Rose C. Guidelines and parameter selection for the simulation of progressive delamination. *2008 ABAQUS User's Conf 2008*:1–15.
- [66] Yao L, Alderliesten RC, Zhao M, Benedictus R. Discussion on the use of the strain energy release rate for fatigue delamination characterization. *Compos Part A Appl Sci Manuf* 2014;66:65–72. doi:10.1016/j.compositesa.2014.06.018.
- [67] Okereke MI, Akpoyomare AI, Bingley MS. Virtual testing of advanced composites, cellular materials and biomaterials: A review. *Compos Part B Eng* 2014;60:637–62. doi:10.1016/j.compositesb.2014.01.007.
- [68] Astm. D5528-01: Standard Test Method for Mode I Interlaminar Fracture Toughness of Unidirectional Fiber-Reinforced Polymer Matrix Composites 1. *Am Stand Test Methods* 2014;03:1–12. doi:10.1520/D5528-13.2.
- [69] De Moraes AB. Mode I cohesive zone model for delamination in composite beams. *Eng Fract Mech* 2013;109:236–45. doi:10.1016/j.engfracmech.2013.07.004.
- [70] ASTM. D7905/D7905M Standard Test Method for Determination of the Mode II Interlaminar Fracture Toughness of Unidirectional Fiber-Reinforced Polymer 2015:1–18. doi:10.1520/D7905.
- [71] ASTM. D5656-10 Standard Test Method for Thick-Adherend Metal Lap-Shear Joints for Determination of the Stress-Strain Behavior of Adhesives in Shear by 2014;10:1–8. doi:http://dx.doi.org/10.1016/j.proci.2008.06.070.
- [72] Tang JH, Sridhar I, Srikanth N. Static and fatigue failure analysis of adhesively bonded thick composite single lap joints. *Compos Sci Technol* 2013;86:18–25. doi:10.1016/j.compscitech.2013.06.018.
- [73] Carvalho UTF, Campilho RDSG. Validation of pure tensile and shear cohesive laws obtained by the direct method with single-lap joints. *Int J Adhes Adhes* 2017;77:41–50. doi:10.1016/j.ijadhadh.2017.04.002.
- [74] Joki RK, Grytten F, Hayman B, Sørensen BF. Determination of a cohesive law for delamination modelling - Accounting for variation in crack opening and stress state across the test specimen width. *Compos Sci Technol* 2016;128:49–57. doi:10.1016/j.compscitech.2016.01.026.

- [75] de Moura MFSF, Campilho RDSG, Gonçalves JPM. Pure mode II fracture characterization of composite bonded joints. *Int J Solids Struct* 2009;46:1589–95. doi:10.1016/j.ijsolstr.2008.12.001.
- [76] Park K, Choi H, Paulino GH. Assessment of cohesive traction-separation relationships in ABAQUS: A comparative study. *Mech Res Commun* 2016;78:71–8. doi:10.1016/j.mechrescom.2016.09.004.
- [77] Shen B, Paulino GH. Identification of cohesive zone model and elastic parameters of fiber-reinforced cementitious composites using digital image correlation and a hybrid inverse technique. *Cem Concr Compos* 2011;33:572–85. doi:10.1016/j.cemconcomp.2011.01.005.
- [78] Campilho RDSG, Moura DC, Gonçalves DJS, Da Silva JFMG, Banea MD, Da Silva LFM. Fracture toughness determination of adhesive and co-cured joints in natural fibre composites. *Compos Part B Eng* 2013;50:120–6. doi:10.1016/j.compositesb.2013.01.025.
- [79] Fernandes RL, Campilho RDSG, Leitão ACC, Azevedo JCS. Numerical Evaluation of the Direct Method for Cohesive Law Extraction in Shear by the End-Notched Flexure Test. *Procedia Eng* 2015;114:94–101. doi:10.1016/j.proeng.2015.08.046.
- [80] Leitão ACC, Campilho RDSG, Moura DC. Shear Characterization of Adhesive Layers by Advanced Optical Techniques. *Exp Mech* 2016;56:493–506. doi:10.1007/s11340-015-0111-4.
- [81] Rajan S, Sutton MA, Fuerte R, Kidane A. Traction-separation relationship for polymer-modified bitumen under Mode I loading: Double cantilever beam experiment with stereo digital image correlation. *Eng Fract Mech* 2018;187:404–21. doi:10.1016/j.engfracmech.2017.12.031.
- [82] Svensson D, Alfredsson KS, Biel A, Stigh U. Measurement of cohesive laws for interlaminar failure of CFRP. *Compos Sci Technol* 2014;100:53–62. doi:10.1016/j.compscitech.2014.05.031.
- [83] Goutianos S, Sørensen BF. The application of J integral to measure cohesive laws under large-scale yielding. *Eng Fract Mech* 2016;155:145–65. doi:10.1016/j.engfracmech.2016.01.004.
- [84] Sadeghi MZ, Zimmermann J, Gabener A, Schroeder KU. The applicability of J-integral approach in the determination of mixed-mode fracture energy in a ductile adhesive. *Int J Adhes Adhes* 2018;83:2–8. doi:10.1016/j.ijadhadh.2018.02.027.
- [85] Jokinen J, Wallin M, Saarela O. Applicability of VCCT in mode I loading of yielding adhesively bonded joints - A case study. *Int J Adhes Adhes* 2015;62:85–91. doi:10.1016/j.ijadhadh.2015.07.004.

- [86] Jokinen J, Kanerva M. Analysis of cracked lap shear testing of tungsten-CFRP hybrid laminates. *Eng Fract Mech* 2017;175:184–200. doi:10.1016/j.engfracmech.2017.01.029.
- [87] Shih CF, Moran B, Nakamura T. Energy release rate along a three-dimensional crack front in a thermally stressed body. *Int J Fracture* 1986;30:79–102.
- [88] Krueger R. Virtual crack closure technique: History, approach, and applications. *Appl Mech Rev* 2004;57:109. doi:10.1115/1.1595677.
- [89] Wildy S, Codrington J. An Algorithm for Identifying a Crack Within a Measured Displacement Field. *J Nondestruct Eval* 2017;36:1–10. doi:10.1007/s10921-017-0406-8.
- [90] Hutchinson JW, Evans AG. *Mechanics of Materials : Top-Down Approaches* 2000;48:125–35.
- [91] Bergan A, Dávila C, Leone F, Awerbuch J, Tan TM. A Mode I cohesive law characterization procedure for through-the-thickness crack propagation in composite laminates. *Compos Part B Eng* 2016;94:338–49. doi:10.1016/j.compositesb.2016.03.071.
- [92] Schreier H, Orteu JJ, Sutton MA. *Image correlation for shape, motion and deformation measurements: Basic concepts, theory and applications*. 2009. doi:10.1007/978-0-387-78747-3.
- [93] Makeev A, Guillaume S, Nikishkov Y, Lee E. *Methods for Assessment of Interlaminar Tensile Strength of Composite Materials*. *Compos Sci Technol* 2013.
- [94] Whitney JM, Browning CE. On short-beam shear tests for composite materials. *Exp Mech* 1985. doi:10.1007/BF02325100.
- [95] Makeev A, Seon G, Cline J, Shonkwiler B. In quest of methods for measuring 3D mechanical properties of composites. *Compos Sci Technol* 2014;100:105–12. doi:10.1016/j.compscitech.2014.05.026.
- [96] Sket F, Enfedaque A, Alton C, González C, Molina-Aldareguia JM, Llorca J. Automatic quantification of matrix cracking and fiber rotation by X-ray computed tomography in shear-deformed carbon fiber-reinforced laminates. *Compos Sci Technol* 2014;90:129–38. doi:10.1016/j.compscitech.2013.10.022.
- [97] Sun CT, Wang CY. A new look at energy release rate in fracture mechanics. *Int J Fract* 2002;113:295–307. doi:10.1023/A:1014260718867.
- [98] Van Blitterswyk J, Cole RG, Laliberté J, Backman D. Digital image correlation as an improved technique for adhesive shear strain measurement in the ASTM D5656 test. *Proc Am Soc Compos - 31st Tech Conf ASC* 2016 2016.

- [99] Jalalvand M, Czél G, Fuller JD, Wisnom MR, Canal LP, González CD, et al. Energy dissipation during delamination in composite materials – An experimental assessment of the cohesive law and the stress-strain field ahead of a crack tip. *Compos Sci Technol* 2016;134:115–24. doi:10.1016/j.compscitech.2016.08.001.